

PARTICLE SIZE DISTRIBUTIONS OF DEBRIS UPSTREAM AND DOWNSTREAM
OF THE CONTAINMENT SUMP STRAINER IN A LIGHT WATER REACTOR

A Thesis

by

MATTHEW JAREB KAPPES

Submitted to the Office of Graduate and Professional Studies of
Texas A&M University
in partial fulfillment of the requirements for the degree of

MASTER OF SCIENCE

Chair of Committee,	Yassin A. Hassan
Committee Members,	William H. Marlow
	Maria D. King
Head of Department,	Yassin A. Hassan

August 2015

Major Subject: Nuclear Engineering

Copyright 2015 Matthew Jareb Kappes

ABSTRACT

During a LOCA in a LWR, a containment-sump strainer filters debris, generated from fibrous thermal insulation, from the water collected in the containment sump. The buildup of debris on the strainer and the bypass of debris through the strainer lead to upstream and downstream effects, respectively.

The objective of this research was to create a methodology for obtaining PSDs for this debris upstream and downstream of a sump strainer in multiple size ranges. Fibrous debris was injected into an experimental facility which simulated the conditions in a LWR containment sump. Samples were taken downstream of the strainer during the experiment. Using a NanoSight LM10 and two optical microscope systems, size measurements of particles were made.

The fractional number of particles between 55-188 nm increased from 0.591 to 0.734 upstream to downstream; the number of all other particle sizes decreased. This trend is consistent with Hutten's [8] statements about the MPPS. For AMIS-1, from upstream to downstream, the fraction of particles smaller than 55 μm increased from 0.77 to 0.89; almost all of the larger particles sizes decreased in number. This demonstrates larger particles being more efficiently filtered. For AMIS-2, from upstream to downstream, the fraction of particles smaller than 340 μm increased from 0.536 to 0.668; all of the larger particle sizes decreased in number. This again demonstrates higher filtration efficiency for larger particles.

Different PDFs provided the best fit for the PSDs in each of the size ranges measured. For the nanometer range, the Johnson's S_B function provided the best fit. For the 10-500 μm range, the upstream and downstream results were fit best with the log-logistic and lognormal functions, respectively. For the 100-2500 μm size range, the Weibull distribution was found to fit best. Changes in the PDFs fit to the upstream and downstream PSDs were similar to what was found when comparing the upstream and downstream PSD histograms.

Size distributions for spherical (tin powder) and angular (SiC F600) particles were easily obtained using the Coulter Counter, however, it didn't provide reliable results for fibrous debris.

DEDICATION

I dedicate this to the most loving and impressive person that I have ever known, Taryn Ashley Rand. I would also like to express my gratitude to my family, who have encouraged me in all of my endeavors.

ACKNOWLEDGEMENTS

I would like to thank my committee members, especially my advisor, Dr. Yassin Hassan, for his support and guidance during the course of this research. I would like to also thank Saya Lee and Suhaeb Abdulsattar for the time and effort that they put into helping me build the necessary experimental facilities to complete this research, as well as all of their valued insights along the way. Finally, I would like to thank the rest of the students in the thermal-hydraulics research group who supported these lengthy experiments.

NOMENCLATURE

AMIS	Automated Microscope Imaging System
BWR	Boiling Water Reactor
B#5	Bottle Number 5
CMOS	Complementary Metal-Oxide Semiconductor
CDF	Cumulative Distribution Function
DI	De-Ionized
DBA	Design Basis Accident
DSLR	Digital Single Lens Reflexive
ESZ	Electrical Sensing Zone
ECCS	Emergency Core Cooling System
ECDF	Empirical Cumulative Distribution Function
GPH	Gallons per Hour
GSI	Generic Safety Issue
K-S	Kolmogorov-Smirnov
LWR	Light Water Reactor
LOCA	Loss of Coolant Accident
MP	Megapixel
MPPS	Most Penetrating Particle Size
NTA	Nanoparticle Tracking Analysis
NIST	National Institute of Standards and Technology

NI	National Instruments
NPT	National Pipe Taper
NEI	Nuclear Energy Institute
NRC	Nuclear Regulatory Commission
PSD	Particle Size Distribution
PWR	Pressurized Water Reactor
PDF	Probability Density Function
SEM	Scanning Electron Microscope
TAMU	Texas A&M University
VWT-04	Vertical Water Test -04
3P	Three Parameter

TABLE OF CONTENTS

	Page
ABSTRACT	ii
DEDICATION	iv
ACKNOWLEDGEMENTS	v
NOMENCLATURE	vi
TABLE OF CONTENTS	viii
LIST OF FIGURES	x
LIST OF TABLES	xvi
1. INTRODUCTION AND LITERATURE REVIEW	1
2. RESEARCH OBJECTIVES AND APPROACH	13
3. EXPERIMENTAL FACILITIES	16
3.1 Vertical-Flow Sump-Strainer Loop	16
3.2 Automated Microscope Imaging System	37
3.2.1. General System Description	37
3.2.2. Calibration and Validation of AMIS	41
3.3 Beckman Coulter Multisizer 3	50
3.4 NanoSight LM10	54
3.4.1. General System Description	54
3.4.2. Determining a Required Number of Completed Tracks	55
4. EXPERIMENTAL PROCEDURES	60
4.1 Vertical-Flow Sump-Strainer Loop	60
4.1.1 Experiment Preparation	60
4.1.2 Setting the Flow Rate of the Isokinetic Sampling Port	64
4.1.3 Debris Preparation Using the NEI Protocol	65
4.1.4 Running the Experiment	72
4.1.5 Experiment Completion and System Cleaning	72
4.2 Automated Microscope Imaging System	75

4.2.1 AMIS-1: DSLR Camera with 10X Microscope Objective	75
4.2.2 AMIS-2: CMOS Camera with 4X Microscope Objective	77
4.3 Beckman Coulter Multisizer 3.....	78
4.4 NanoSight LM10	81
5. RESULTS AND ANALYSIS	85
5.1 Upstream Versus Downstream Particle Size Distributions	85
5.1.1. NanoSight LM10 Results	86
5.1.2. AMIS-1 Results	93
5.1.3. AMIS-2 Results	101
5.2 Coulter Counter Results for Non-Fibrous Debris	107
6. CONCLUSION	116
REFERENCES	119

LIST OF FIGURES

	Page
Figure 1. Spray from a line break collecting in the containment sump [2].....	2
Figure 2. Diagram showing the containment sump and sump strainers [3]	2
Figure 3. Mechanisms of particle capture [10].....	7
Figure 4. Filter efficiency (%) versus particle size (μm) for two filter media [11].....	8
Figure 5. Change in MPPS with fluid velocity [10].....	10
Figure 6. The Coulter principle	12
Figure 7. Simulated sump strainer.....	14
Figure 8. Vertical-flow sump strainer loop	17
Figure 9. Stainless-steel tank with polycarbonate viewing windows.....	18
Figure 10. Polycarbonate tank lid.....	19
Figure 11. Mixing propeller inside of tank.....	20
Figure 12. (a) Mixing-propeller motor and (b) motor-control relay	20
Figure 13. Stainless-steel centrifugal pump	21
Figure 14. Strainer position within the test section	22
Figure 15. (a) Test section and (b) the downstream-sample collection valve.	23
Figure 16. (a) Differential pressure transducer and (b) signal conditioner	26
Figure 17. Schematic of the pressure transducer calibration setup	27
Figure 18. Calibration curve for Honeywell TJE differential-pressure transducer	28
Figure 19. Electromagnetic flow meter.....	29

Figure 20. Calibration curve for Krohne® Optiflux-1300 flow meter.....	31
Figure 21. Tank-mounted thermocouple (a) and pump-inlet thermocouple (b).....	32
Figure 22. (a) Camera and (b) its triggering circuit	33
Figure 23. National Instruments SCXI-1000 data acquisition system	34
Figure 24. System control panel.....	35
Figure 25. Heating loop (6 kW)	36
Figure 26. Automated microscope imaging system (AMIS).....	37
Figure 27. x and y-axis slides (a) and slide-motor controllers (b).....	38
Figure 28. AMIS-1: DSLR camera with 10X microscope objective (a) and its triggering circuit (b)	40
Figure 29. Camera with 4X microscope objective	40
Figure 30. Klarmann Rulings, Inc. KR-838 stage micrometer	41
Figure 31. Image of a KR-838 stage micrometer taken using AMIS-1	42
Figure 32. Particle measurements for Coulter CC Size Standards from AMIS-1	44
Figure 33. Original (left) and processed (right) image of L10 particles from AMIS-1 ..	45
Figure 34. Original (left) and processed (right) image of L90 particles from AMIS-1 ..	45
Figure 35. Image of a KR-838 stage micrometer taken using AMIS-2	46
Figure 36. Particle measurements for Coulter CC Size Standards from AMIS-2.....	48
Figure 37. Original (left) and processed (right) image of L65 particles from AMIS-2 ..	49
Figure 38. Original (left) and processed (right) image of L90 particles from AMIS-2 ..	49
Figure 39. Beckman Coulter Multisizer™ 3 COULTER COUNTER [13]	50
Figure 40. Schematic of the Beckman Coulter Multisizer 3 [14]	51

Figure 41. Multisizer 3 exterior components [14].....	52
Figure 42. Sample compartment of the Multisizer 3 [14]	53
Figure 43. NanoSight LM10	54
Figure 44. Sample-viewing unit showing the viewing window	55
Figure 45. Number count versus maximum bin value for different numbers of tracked particles.....	56
Figure 46. Number count versus maximum bin value for 2000 tracked particles with different numbers of bins	57
Figure 47. Normalized count versus maximum bin value for 2000 tracked particles with different numbers of bins	58
Figure 48. Normalized histograms for comparison of tracked-particle number from NanoSight LM10.....	59
Figure 49. Downcomer pipe support.....	61
Figure 50. Approximate location of the filter bag installation	62
Figure 51. One-liter bottle for downstream sampling	63
Figure 52. Scale used for setting the sampling port flow rate	64
Figure 53. One-side baked NUKON® mat	66
Figure 54. Weighing the NUKON debris.....	67
Figure 55. Layer separation.....	68
Figure 56. Manual debris size reduction	69
Figure 57. Reduced-size debris inside of the five-gallon mixing bucket.....	70
Figure 58. Pressure washer mixing –outside (a) and inside (b) of the bucket.....	71

Figure 59. Final state of debris sample in the bucket (a) and in the glass tray (b)	71
Figure 60. 1 μm polyester felt filter bag for 6 in pipe	73
Figure 61. Water level in tank during system cleaning	75
Figure 62. 200 μl wet debris sample prepared for use with the automated microscope imaging systems	76
Figure 63. Aperture tube placement in the Multisizer 3 [14]	80
Figure 64. NanoSight NTA 2.3 software	82
Figure 65. Viewing unit showing the injection and the thermocouple ports.....	83
Figure 66. Drawing of NanoSight viewing unit showing the area where the camera was focused [15].....	84
Figure 67. Debris bed at the (a) start and (b) end of sampling for VWT-04 B#5	85
Figure 68. Size distribution of the upstream debris between 10 and 500 nm	87
Figure 69. Size distribution of the downstream debris between 10 and 500 nm	87
Figure 70. Johnson S_B functions fit to the distributions of the upstream (NEI Nukon debris) and downstream (VWT-04 B#5) particle sizes from the NanoSight LM10	91
Figure 71. Comparison of the three functions chosen for fitting the particle size distribution of the upstream debris (NEI-prepared Nukon) from the NanoSight LM10	92
Figure 72. Comparison of the three functions chosen for fitting the particle size distribution of the downstream particles (VWT-04 B#5) from the NanoSight LM10	92

Figure 73. Image taken with AMIS-1 (a) before and (b) after processing	94
Figure 74. Feret length of a particle (represented by the green line) [16].....	94
Figure 75. Size distribution of the upstream debris from AMIS-1	96
Figure 76. Size distribution of the downstream debris from AMIS-1.....	96
Figure 77. Lognormal function fit to the distributions of the upstream (NEI Nukon debris) and downstream (VWT-04 B#5) particle sizes from AMIS-1	99
Figure 78. Comparison of the three functions chosen for fitting the particle size distribution of the upstream debris (NEI-prepared Nukon) from AMIS-1	100
Figure 79. Comparison of the three functions chosen for fitting the particle size distribution of the downstream debris (VWT-04 B#5) from AMIS-1	101
Figure 80. Image taken with AMIS-2 (a) before and (b) after processing	102
Figure 81. Size distribution of the upstream debris from AMIS-2	103
Figure 82. Size distribution of the downstream debris from AMIS-2.....	104
Figure 83. Weibull function fit to the distributions of the upstream (NEI Nukon debris) and downstream (VWT-04 B#5) particle sizes from AMIS-2.....	105
Figure 84. Comparison of the three functions chosen for fitting the particle size distribution of the upstream debris (NEI-prepared Nukon) from AMIS-2	106
Figure 85. Comparison of the three functions chosen for fitting the particle size distribution of the downstream debris (VWT-04 B#5) from AMIS-2	107
Figure 86. SEM image of SiC F600 powder at 250x magnification.....	108
Figure 87. SEM image of SiC F600 powder at 1,000x magnification	108
Figure 88. Example of an angular particle from NIST morphology glossary [17]	109

Figure 89. Example of a quadrangular particle from NIST morphology glossary [17].....	109
Figure 90. Size distribution of F600 SiC from Coulter Counter (100- μ m aperture).....	111
Figure 91. SEM image of tin particles at 1,000x magnification	112
Figure 92. SEM image of tin particles at 10,000x magnification	112
Figure 93. Example of a spherical particle from NIST morphology glossary [18].....	113
Figure 94. Example of a sub-sphere particle from NIST morphology glossary [18]....	113
Figure 95. Size distribution of tin particles from Coulter Counter (30- μ m aperture)...	115

LIST OF TABLES

	Page
Table 1. Fibrous debris classification by shape [9]	5
Table 2. Characteristics of the sump strainer	14
Table 3. Values used for checking the sampling-port flow rate	25
Table 4. Calibration data from Honeywell TJE differential-pressure transducer.....	27
Table 5. Calibration data from Krohne® Optiflux-1300 flow meter	30
Table 6. Control panel components.....	35
Table 7. Specifications of AMIS-1	43
Table 8. Size information of mono-sized particles and measurements from AMIS-1	44
Table 9. Specifications of AMIS-2.....	47
Table 10. Size information of mono-sized particles and measurements from AMIS-2 ..	48
Table 11. Aperture tubes with corresponding size measurement ranges.....	79
Table 12. Results from the NanoSight LM10 for debris size upstream (NEI Nukon debris) and downstream (VWT-04 B#5) of the strainer.....	86
Table 13. PDFs used for fitting the data from the NanoSight LM10	88
Table 14. Results from PDF fitting of the upstream (NEI-prepared Nukon) and downstream (VWT-04, B#5) particle size distributions from NanoSight LM10.....	90
Table 15. Results from AMIS-1 for debris size upstream (NEI Nukon debris) and downstream (VWT-04 B#5) of the strainer	95

Table 16. PDFs used for fitting the results from AMIS-1	97
Table 17. Results from PDF fitting of the upstream (NEI-prepared Nukon) and downstream (VWT-04, B#5) particle size distributions from AMIS-1	98
Table 18. Results from AMIS-2 for debris size upstream (NEI Nukon debris) and downstream (VWT-04 B#5) of the strainer	103
Table 19. Results from PDF fitting of the upstream (NEI-prepared Nukon) and downstream (VWT-04, B#5) particle size distributions from AMIS-2	105
Table 20. Results for SiC powder from the Coulter Counter using a 100- μm aperture.....	110
Table 21. Results for tin particles from the Coulter Counter using a 30- μm aperture ..	114

1. INTRODUCTION AND LITERATURE REVIEW

For a nuclear reactor, the possibility of a rupture occurring in the reactor's primary coolant loop is a design basis accident (DBA). This accident scenario, known as a loss-of-coolant accident (LOCA), is a major consideration in the licensing and operating requirements of any reactor and it is an event which all reactors are designed to withstand [1]. The water that is discharged into the containment vessel is first collected in the containment sump, as shown in Figure 1, and then recirculated into the core for residual heat removal. The system that accomplishes this task is known as the emergency core cooling system (ECCS). The ECCS of both Boiling Water Reactors (BWRs) and Pressurized Water Reactors (PWRs) employ a containment sump strainer which filters out debris created from water/steam break-jet impingement upon reactor structural materials and fibrous thermal insulation during a LOCA. A diagram showing the containment sump strainers can be seen in Figure 2. The debris buildup on the sump strainer and the bypass of debris through the strainer can have several effects on the functionality of the ECCS. These effects are broken up into two categories: the upstream effects and the downstream effects [1].

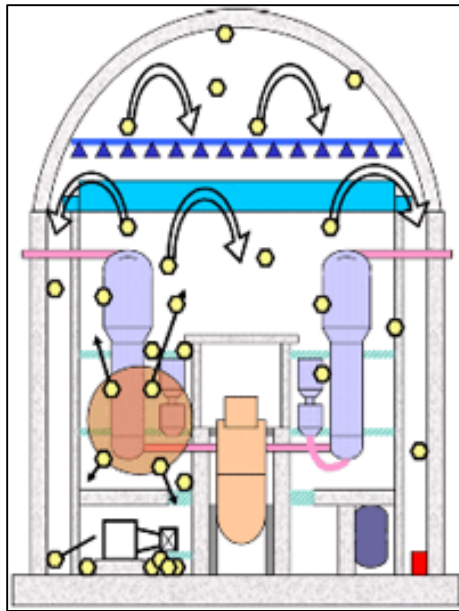


Figure 1. Spray from a line break collecting in the containment sump [2]

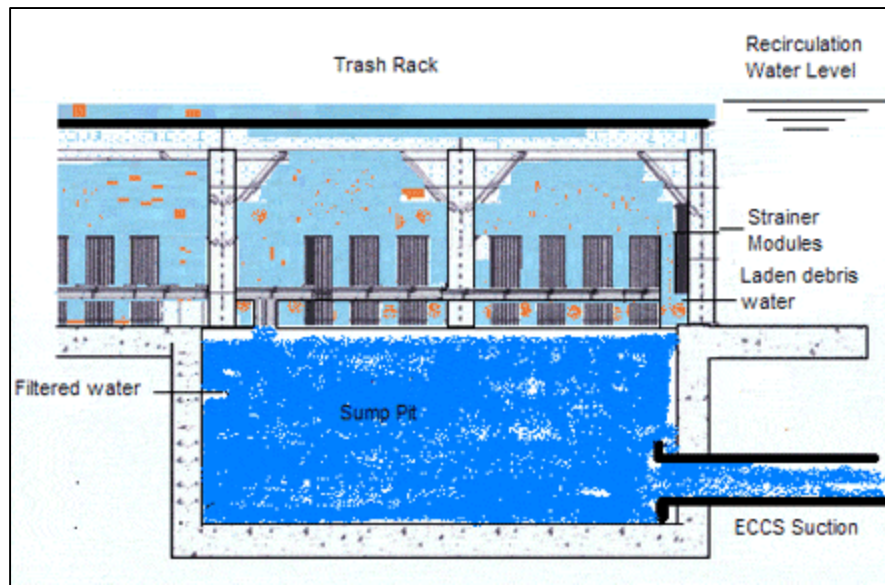


Figure 2. Diagram showing the containment sump and sump strainers [3]

Upstream effects include the blockage of flow to the containment sump, and pump failure caused by the buildup of debris on the sump strainer. In 1992 a loss of containment spray accident occurred at the Barsebäck Unit 2 in Sweden. This accident occurred when two ECCS-pump-suction strainers became clogged by debris. This event demonstrated that the predictions made by models developed for resolution of the U.S. Nuclear Regulatory Commission's (NRC) USI A-43 [4], "Containment Emergency Sump Performance" had underestimated the quantity of fibrous debris that could reach the strainers. This accident, along with two more occurrences at BWR/6 with Mark III containment of Perry Nuclear plant in 1996, prompted the U.S. NRC to initiate analyses to estimate the potential for loss of Net Positive Suction Head (NPSH), constituted Generic Safety Issue (GSI) 191, "Assessment of Debris Accumulation on PWR Sump Performance" [5].

Downstream effects occur when a portion of the debris in the containment sump bypasses the strainer and is then carried into the downstream components and the reactor core with the returning cooling water [1]. This debris can then be deposited in pumps, valves, and the coolant flow channels and has the potential to restrict coolant flow within the flow channel. This flow degradation will ultimately lead to a decrease in the coolant's ability to remove heat from the reactor core, which can result in damage to core components and structural materials [6]. For these reasons, the effects of debris accumulation on reactor-sump performance are of great concern to the nuclear industry and have been extensively studied.

The characteristics of the fibrous debris upstream of the strainer are dependent upon the debris production method. During the filtering process, the size characteristics and concentration of debris downstream of the strainer are initially dependent upon the strainer dimensions and later upon the properties of the fibrous debris bed, which builds up on the strainer over time. Merkus [7] categorizes the size of particulate material in the following manner:

- Nano: ≤ 100 nm
- Ultrafine: 100 nm – 1 μ m
- Fine: 1 μ m – 10 μ m
- Medium: 10 μ m – 1 mm
- Coarse: 1 mm – 10 mm



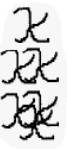




For particle size distributions (PSDs), the log-normal law is frequently observed, and the log-normal function is often used for fitting particle size measurement data.

Johnson's S_B distribution is essentially a truncated log-normal distribution. Unlike the log-normal distribution, Johnson's S_B is bounded by a minimum and maximum size, which must be present in any physical particle system. Another function commonly used is the Rosin-Rammler-Bennett-Sperling (RRBS), also known as the Weibull distribution. This distribution is bounded by a minimum value. Allen [8] states that this function was originally derived for broken coal, but has been found to be applicable to many other materials.

The size of the particles that make up the debris is not the only characteristic which needs to be considered; morphological properties, such as particle shape, are also

important. Zigler et al. [9] provides a classification of the shape of fibrous debris generated by a LOCA, which is shown in Table 1, below.

Table 1. Fibrous debris classification by shape [9]

Class Number	Description	
1		Very small pieces of fiberglass material, "microscopic" fines which appear to be cylinders of varying L/D.
2		Single flexible strand of fiberglass, essentially acts as a suspended strand.
3		Multiple attached or interwoven strands that exhibit considerable flexibility and, which due to random orientations induced by turbulence drag, could result in low fall velocities.
4		Formation of fibers into clusters which have more rigidity and which react to drag forces more as a semi-rigid body.
5		Clumps of fibrous debris which have been noted to sink.
6		Larger clumps of fibers. Forms an intermediate class between 5 and 7
7		Precut pieces (i.e., .25" by .25") to simulate small debris. Other manual/mechanical methods to produce test debris.

Hutten [10] states that the purpose of a filter is to remove undesirable contaminants from a fluid stream with the goal of protecting the environment downstream of the filter; this is the case for the containment-sump strainer. As previously mentioned, filtration of the fibrous material will determine the size characteristics of the particles that bypass the strainer. There are four fundamental filtration mechanisms which Sutherland and Purchas [11] described.

- Surface straining: This occurs when a filter with a uniform pore size, such as a perforated plate, is used and only particles which are smaller than the pore size will pass through the filter. Any debris larger than the pore size will be filtered effectively.
- Depth straining: The filter material is relatively thick compared to its pore diameter, which varies with the depth. As particles are transported through the pores they become trapped at points where the pore size becomes smaller than the debris being transported.
- Depth filtration: This mechanism differs from depth straining in the respect that necking is not the only means by which the particle is trapped. Depth filtration is concerned with other physical phenomena which allow for the capture of particles in a pore at a point where the pore diameter is larger than the particle. This requires that the particle be brought into contact with the wall of the pore and then become attached to the wall. This transport to the pore wall and subsequent capture of the particle in the filtering medium, occurs in one of the following ways: inertial impaction, which is a result of particles with sufficient

inertia breaking away from fluid streamlines and impacting the fibrous material; interception, where particles travel close enough to the fibers of the filter material that natural forces cause attachment of the particle to the fiber; diffusion, or random Brownian motion which causes very small particles to leave fluid streamlines and come into contact with a filter material fiber. After reaching the fiber, the particles are attached by means of the van der Waals and other surface forces [11]. A classical illustration of these particle-capture mechanisms can be seen in Figure 3.

- Cake filtration: This mechanism takes place when particle buildup on or near the surface of the filter begins to function as a filter itself. The layering buildup is known as filter cake.

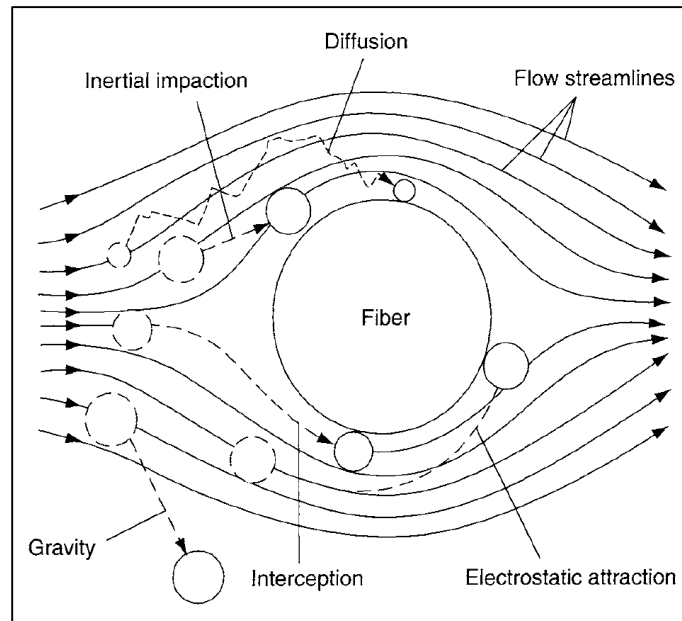


Figure 3. Mechanisms of particle capture [10]

For the current research, all of these filtration mechanisms will contribute to the debris bed generation and to the characteristics of the debris downstream of the strainer. Surface straining on the perforated plate will initially filter most of the fibrous debris, but as a debris bed of appreciable thickness is generated on the strainer, cake filtration will start to play an active role. With a fibrous debris bed, both depth straining and depth filtration will inevitably be present.

In general, “the retention efficiency of a filter medium decreases as the size of the particles reduces” [11]; this is illustrated in Figure 4.

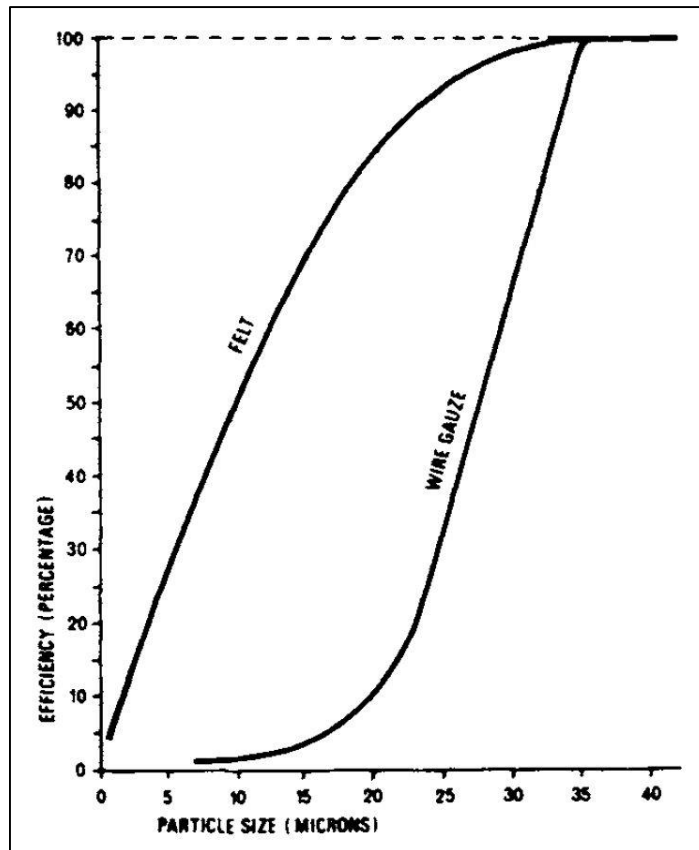


Figure 4. Filter efficiency (%) versus particle size (μm) for two filter media [11]

Although dependent upon particle size, it is not always the case that filtration efficiency is lower for smaller particles in every size range. For depth filtration, the dominant capture mechanism is related to particle size. Brownian motion is important for very small particles, which are subject to capture by diffusion. Large particles have more momentum, making them more likely to break loose from the fluid streamlines and be captured through inertial impaction. There is a particle-size range from 0.04-0.4 μm that is too large for substantial diffusion effects yet too small to have sufficient momentum for inertial effects [10]. The relative inefficiencies of the diffusion and inertial mechanisms here typically lead to the most penetrating particle size (MPPS) being within this range. The MPPS is variable, dependent upon the velocity of the fluid, and will decrease as the fluid velocity increases (Figure 5). The figure below also suggests that there is a velocity at which the amount of particle penetration reaches a maximum.

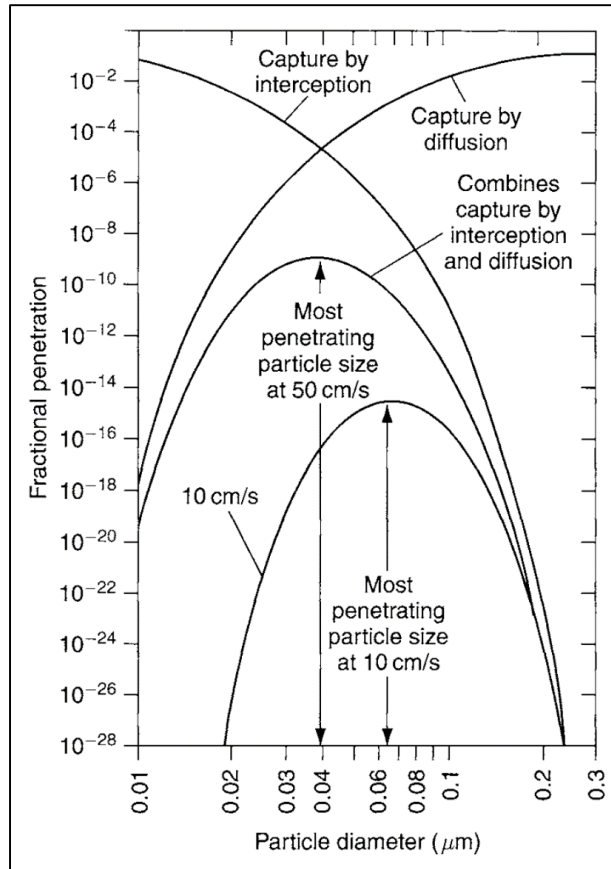


Figure 5. Change in MPPS with fluid velocity [10]

Optical methods are commonly used for particle-size analysis, and are heavily relied upon for size characterization of irregular shape. Optical microscopy is often used for particle sizes ranging from 3 μm to 150 μm ; while any particles that are larger than this can be sized using a magnifying glass. The lower limit of this range is determined by the following equation for the theoretical limit of resolution, d_L .

$$d_L = \frac{f \lambda}{NA} \quad (1)$$

In this equation f is a factor allowing for the inefficiency of the system ($f \approx 0.6$), λ is the wavelength of the illuminant, and $NA = \mu \sin\theta$ where μ is the refractive index of the immersion medium and θ is the angular aperture of the objective [8].

Although “microscopy is often used as an absolute method of particle size analysis since it is the only method in which the individual particles are observed and measured” [8], particles smaller than 3 μm need to be analyzed by other means; a popular method is the coulter technique. This method works by measuring the electrical impedance between two electrodes that are submerged in an electrolytic solution on opposite sides of a small aperture. The particles are suspended in the electrolytic solution and are forced to pass through the aperture, which changes the impedance between the electrodes. This change in impedance generates a pulse whose amplitude is proportional to the volumes of the particle. Figure 6 shows a drawing presenting the basic idea of the Coulter principle.

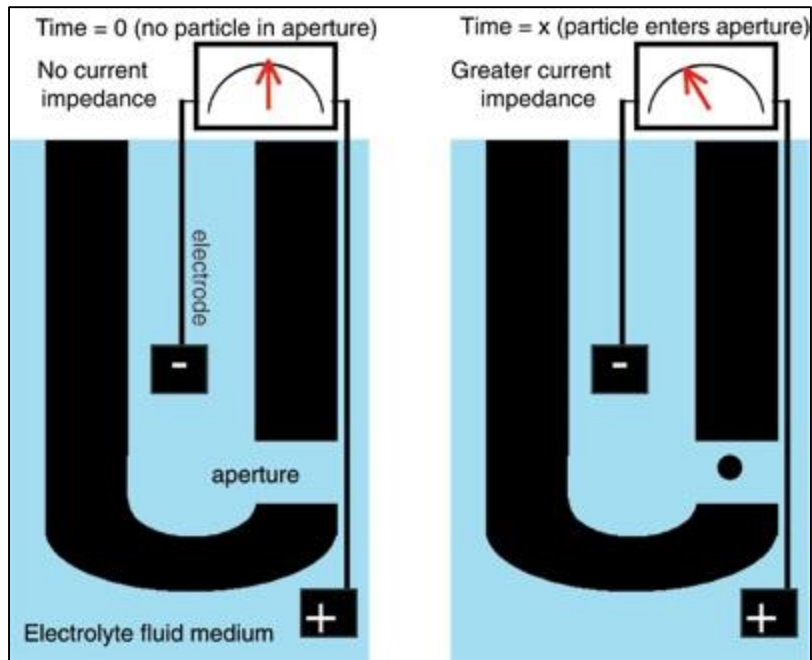


Figure 6. The Coulter principle

In the above figure, a cross section of the aperture tube can be seen with a positive and negative electrode on either side of the tube wall. On the left, the aperture is free of debris, thus there is no impedance across the electrodes. On the right, as a particle is drawn into the aperture, there is an increase in the impedance which can be measured.

2. RESEARCH OBJECTIVES AND APPROACH

The objective of this particular research was to create a methodology for obtaining particle-size distributions (PSDs) for fibrous-thermal-insulation debris, created during a LOCA, both upstream and downstream of a containment sump strainer in multiple size ranges. This involved debris production, filtration of the debris through a sump strainer, sampling of debris both upstream and downstream of the strainer, and size measurements of the particles in the debris samples.

The fibrous debris needed to be representative of that created during a LOCA, and the method of debris production chosen for this study was the protocol developed by the Nuclear Energy Institute [12]. This debris was sampled directly. The NEI method is described in detail in Section 4.1.3.

This debris then had to be introduced into an experimental facility that simulated the conditions of the containment sump. The facility designed for conducting these experiments was a semi-closed loop of piping with a removable test section housing the containment sump strainer. A variable-speed pump was installed in the loop to reach the targeted fluid approach velocity, and a tank at the top of the loop was used for injecting the NEI-prepared debris. The strainer was oriented horizontally, with the flow direction being vertically downward through it. A picture of the strainer used during this study can be seen in Figure 7; the characteristics of it are shown in Table 2. In order to sample the debris downstream of the strainer, an isokinetic sampling port was installed in the test section below the strainer.



Figure 7. Simulated sump strainer

Table 2. Characteristics of the sump strainer

Plate Thickness	1.56 mm
Hole Diameter	2.42 mm
Center-to-Center Hole Pitch	3.97 mm

For size measurements of the fibrous debris, multiple methods were employed. For particles from 10 – 2500 μm , two optical-microscope systems were developed at TAMU. The irregular shape of the fibrous particles in this range required the use of visual characterization and measurement of the debris. For particles from 10 – 500 nm, a nanoparticle tracking analysis machine, NanoSight LM10, was used. A Multisizer 3

Coulter Counter was used in an attempt to measure particles between 0.6 – 18 μm , however measurement were disrupted by the buildup of larger debris fibers over the aperture.

3. EXPERIMENTAL FACILITIES

3.1 Vertical-Flow Sump-Strainer Loop

The vertical-flow sump-strainer loop was designed and constructed to simulate the filtration of NUKON debris through a stainless-steel perforated-plate strainer during a LOCA. It consists of a stainless-steel tank, a polycarbonate test section with a stainless-steel strainer, a pump, and an electromagnetic (EM) flow meter all connected in a semi-closed loop by stainless-steel and polycarbonate piping. The strainer was installed horizontally in a 6 in-diameter polycarbonate test section 172 in (436 cm) below the tank, where the flow direction is vertically downward. The piping diameter was reduced from 6 in to 1 in, below the test section. This 1 in pipe was then connected to the inlet of a centrifugal pump. The piping from the outlet of the pump is also 1 in and returns to the tank after passing through the flow meter. A picture of this experimental facility can be seen in Figure 8.

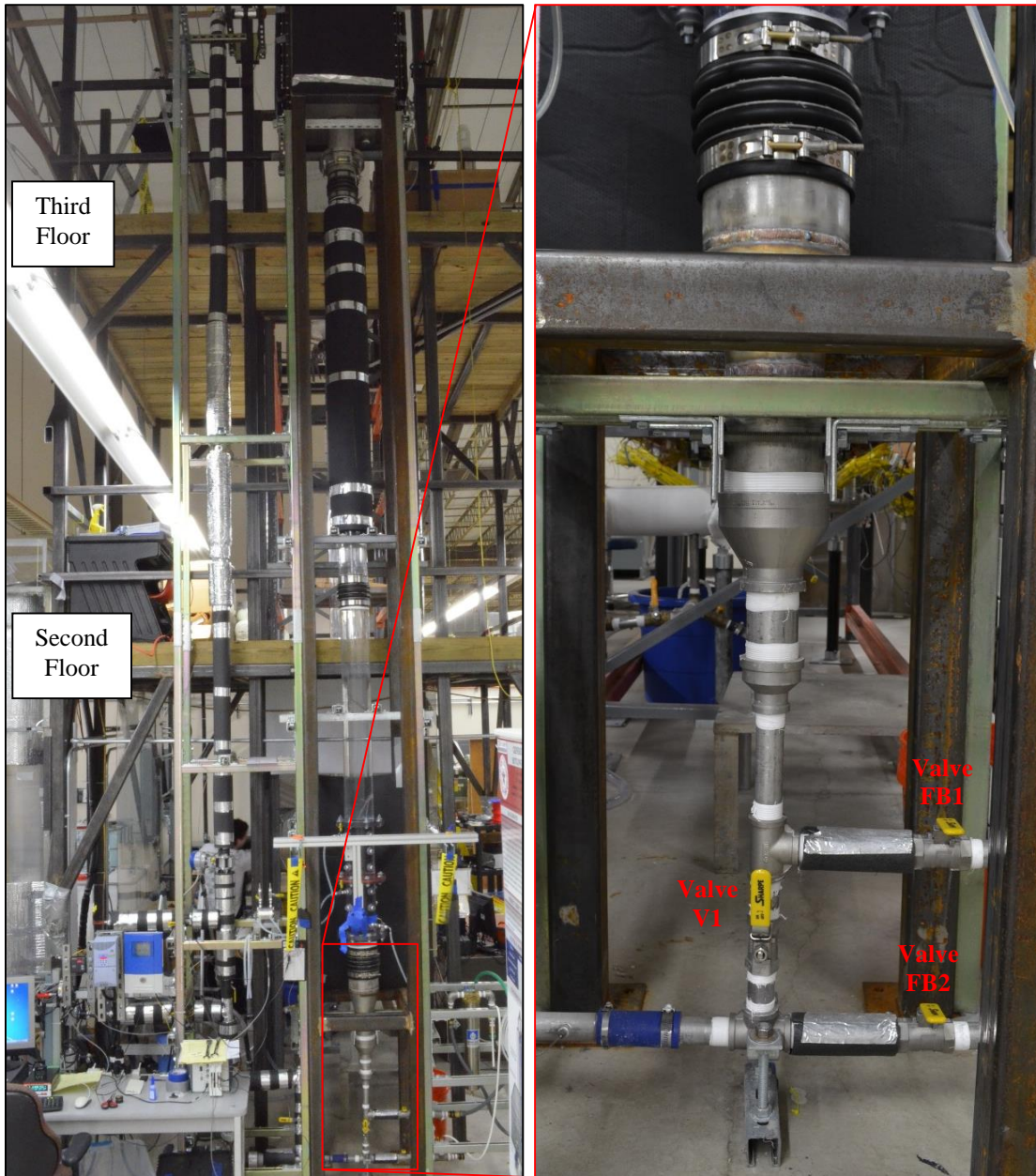


Figure 8. Vertical-flow sump strainer loop

The tank (Figure 9) was constructed from 1/8 in stainless steel with a length and width of 23.75 in, and a height of 29.875 in. It has three polycarbonate windows which allow for visualization of the conditions in the tank. The tank outlet is located at the

center of the bottom face and is 6 inches in diameter. The top of the tank has a 3 inch-wide flange around it with bolt holes which are used to secure a polycarbonate lid, shown in Figure 10.



Figure 9. Stainless-steel tank with polycarbonate viewing windows

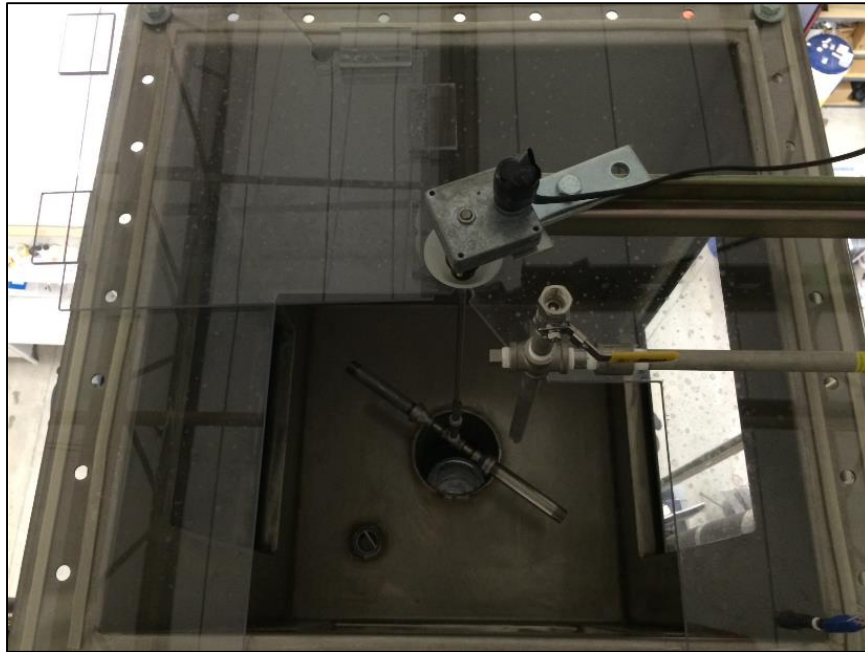


Figure 10. Polycarbonate tank lid

The mixing propeller was assembled using stainless-steel piping. For this mixer, $\frac{1}{2}$ in NPT was used for the body and $\frac{3}{4}$ inch NPT for the arms, to form a t-shape, as shown in Figure 11. A time-adjustable relay was connected to the propeller motor to control the direction of spin, and allowed the spin direction to be switched every one minute. The propeller motor and motor-control relay can be seen in Figure 12.



Figure 11. Mixing propeller inside of tank



a



b

Figure 12. (a) Mixing-propeller motor and (b) motor-control relay

The three-phase centrifugal pump (Figure 13) in this system provides the required flow rate to achieve the necessary approach velocity in the test section (0.3 cm/s). The pump speed, and thus the flow rate, are controlled using a variable-frequency drive, which is part of the control panel. Stainless steel was selected for the impeller and casing, due to its corrosion resistance.



Figure 13. Stainless-steel centrifugal pump

The test section is made of two separate sections of polycarbonate pipe. Each of these sections have a flange on both sides. The flanges are used for installation of the strainer into the test section (Figure 14), and for installation of the test section into the downcomer.

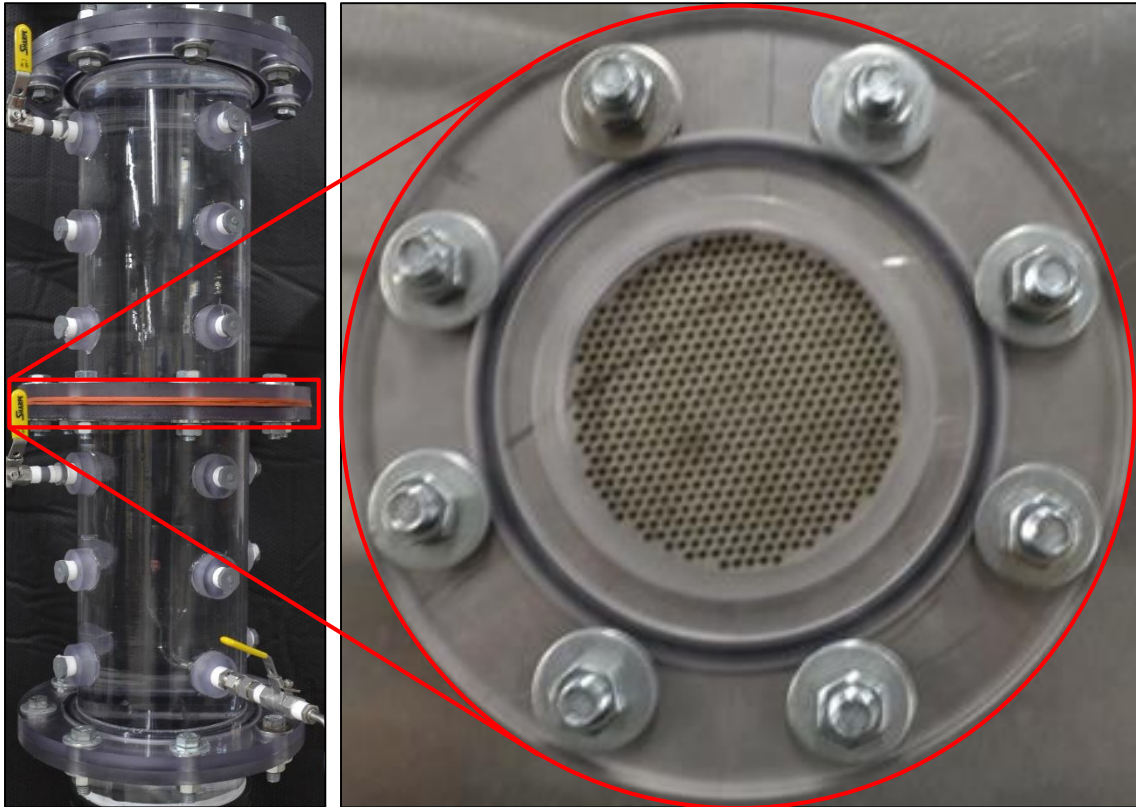


Figure 14. Strainer position within the test section

There is a pressure tap with a valve and barbed hose fitting on both of the test section pipes; this is where the differential pressure transducer is connected. Figure 15.a shows the valves, labeled DP1 and DP2, where the pressure transducer connects to the test section. A glass tube (Figure 15.a) was installed in the bottom half of the test section and was used to collect samples downstream of the strainer. Sampling was initiated by opening valve SP2 and the sampling flow rate was controlled by adjusting the height of this valve using a mechanical slide (Figure 15.b).

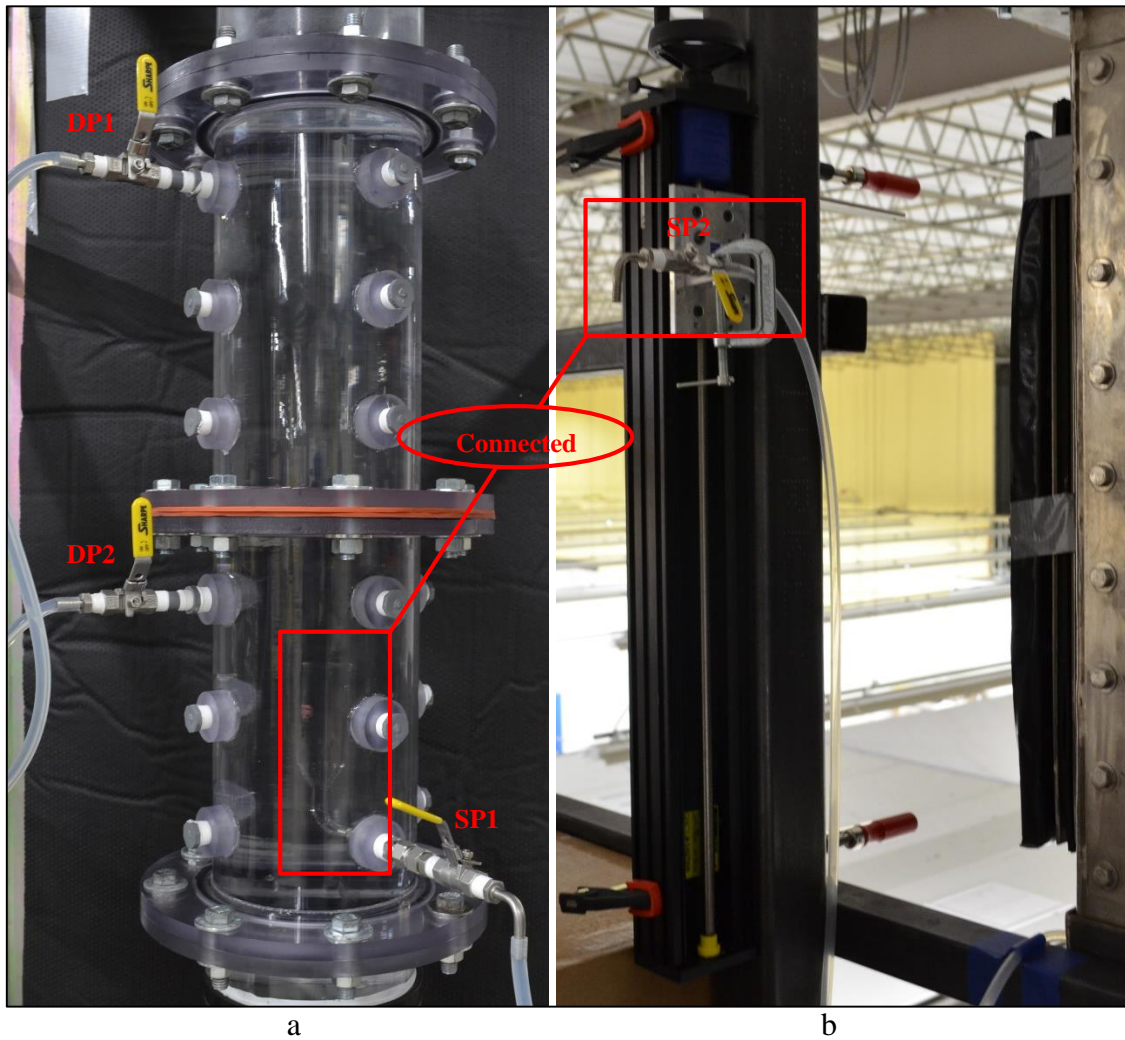


Figure 15. (a) Test section and (b) the downstream-sample collection valve.

The flow rate of the sampling port was set such that the velocity of the fluid entering the sampling port was equal to the approach velocity at the strainer, 0.311 cm/s. The inner diameter of the glass tube used for sampling is 0.978 in, giving an area of 4.85 cm². The required volumetric flow rate of 1.509 cm³/s at the sampling port entrance was calculated as $\dot{V} = v * A$, where v is the approach velocity, and A is the sampling-port

area. The equivalent mass flow rate, 1.504 g/s, was then calculated from the following equation: $\dot{m} = \dot{V} * \rho$, where ρ is 0.997 g/cm³, the density of water at 25°C and 100 kPa.

To measure the flow rate at the sampling-port outlet, a timer and an Acculab® VI-2400 scale were used. The uncertainty in the time measurement was assumed to be 1 s. The scale has a measuring range of 0 – 2400g and readability of 0.1g. The calibration of the scale was verified using the following NIST certified weights:

- 1 g ± 0.0009 g
- 5 g ± 0.0015 g
- 10 g ± 0.002 g
- 50 g ± 0.01 g

All the possible combinations of these weights were verified.

The uncertainty in the measurement of the sampling port flow rate, $\sigma_{\dot{V}}$, was calculated as follows:

$$\sigma_{\dot{V}} = \sqrt{\left(\frac{\partial \dot{V}}{\partial t} \sigma_t\right)^2 + \left(\frac{\partial \dot{V}}{\partial m} \sigma_m\right)^2 + \left(\frac{\partial \dot{V}}{\partial \rho} \sigma_\rho\right)^2}, \quad (2)$$

where \dot{V} is the volumetric flow rate, t is measured time, σ_t is the uncertainty in the time (± 1 s), m is the measured mass, σ_m is the uncertainty in the mass (± 0.1 g), ρ is the density of water, σ_ρ is the uncertainty in the density of water (± 0.003 g/cm³). In order to determine the uncertainty in the density of the water, it was assumed that changes in the temperature of the system would be the only appreciable source of change in the density

of the water; a $\pm 5^\circ\text{C}$ temperature uncertainty was assumed. The density at lower temperature (20°C) and higher temperature (30°C), both at 100 kPa, were found using a table of the properties of water. The differences between these two values and the reference density (25°C , 100 kPa) were calculated and the larger of the two was used as the uncertainty in the density (σ_ρ). Plugging $\dot{V} = \frac{m}{t \cdot \rho}$ into Eq. 2 and simplifying gives:

$$\sigma_{\dot{V}} = \sqrt{\left(\frac{m \cdot \sigma_t}{\rho \cdot t^2}\right)^2 + \left(\frac{\sigma_m}{\rho \cdot t}\right)^2 + \left(\frac{m \cdot \sigma_\rho}{\rho^2 \cdot t}\right)^2} \quad (3)$$

The mass of the water from the sampling port was checked at different times, this mass was then converted into volume using the density of water. The check points used, along with the mass and corresponding error values can be seen in table below.

Table 3. Values used for checking the sampling-port flow rate

Time, t (s)	Mass, m (g)	$\sigma_{\dot{V}}$ (ml/s)
10	15.0	0.151
30	45.1	0.051
60	90.2	0.025
120	180.5	0.013

To measure the head loss produced by fibrous-debris beds in the test section, a differential pressure transducer (Honeywell® TJE, range: 1psid, accuracy: 0.1% full-

scale) was installed. An image of the pressure transducer and its signal conditioner is in Figure 16, below.

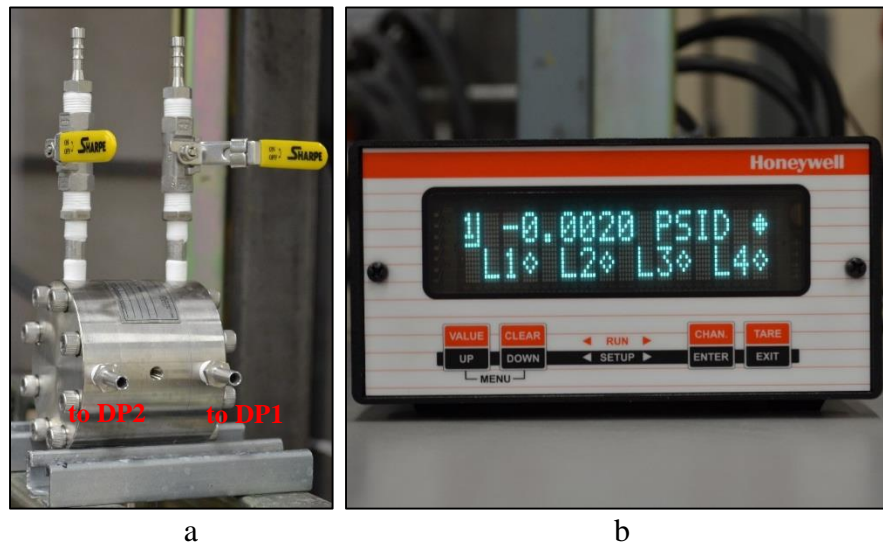


Figure 16. (a) Differential pressure transducer and (b) signal conditioner

A calibration was performed to convert the voltage signal from the pressure transducer into a differential pressure value in the data acquisition system. This was done by varying the height of a water column on one side of the pressure transducer while keeping the other constant. Figure 17 shows a schematic diagram of the setup used.

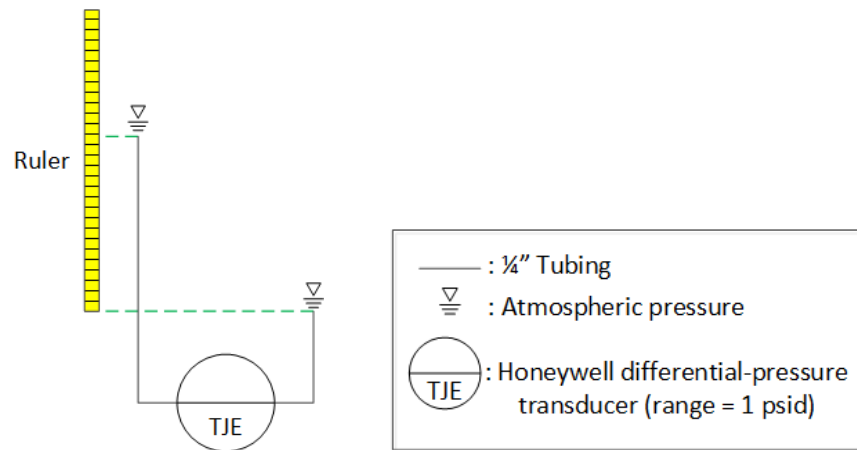


Figure 17. Schematic of the pressure transducer calibration setup

The tube on the low pressure side of the transducer was kept at a constant elevation (the zero value on the ruler), while the tube on the high pressure side was moved to different points on the ruler. At each point, the value from the signal conditioner and the output voltage from the transducer were recorded (Table 4).

Table 4. Calibration data from Honeywell TJE differential-pressure transducer

Signal Conditioner (psid)	Voltage Output (V)
-0.0015	-0.006
0.177	0.0024
0.353	0.011
0.531	0.0195
0.71	0.029

The signal conditioner values were plotted versus the voltage output and fitted to an equation of the form $P = a * V + b$, where P is the differential pressure in psid, V is the voltage output, and a and b are constants. Solving for a and b gave the equation

$$P = 20.392 * V + 0.1259, \quad (4)$$

with an R^2 value of 0.9995. Figure 18 shows the calibration curve, the measured value of pressure versus the value calculated using Eq. 4. All of the data points except the first are within the $\pm 2\%$ lines.

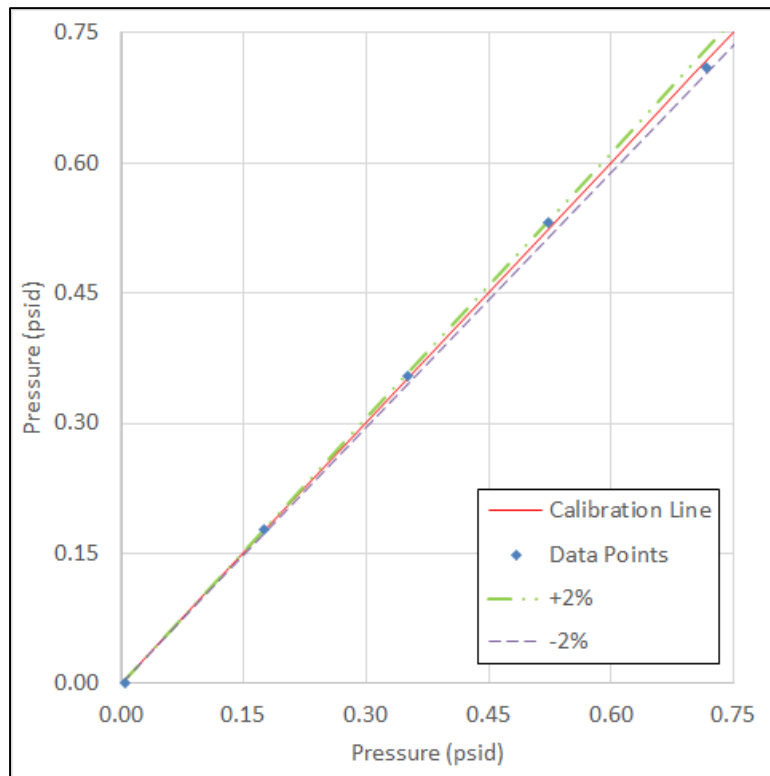


Figure 18. Calibration curve for Honeywell TJE differential-pressure transducer

A Krohne® Optiflux-1300 electromagnetic flow meter (Figure 19) was installed downstream of the pump to read the volumetric flow rate. The accuracy at the target flow velocity, 0.3 cm/s, is 1.26453% of the reading.



Figure 19. Electromagnetic flow meter

For this flow meter, a calibration was performed in order to convert the voltage signal from the flow meter's signal conditioner into a value of flow rate in GPH in the data acquisition system. The flow rate was varied using the variable-speed pump, and the reading from the signal conditioner as well as the voltage output were recorded. The recorded values for this calibration are shown in Table 5.

Table 5. Calibration data from Krohne® Optiflux-1300 flow meter

Signal Conditioner (GPH)	Voltage Output (V)
0	0.801
54	0.832
218	0.927
357	1.007
585	1.137

The signal conditioner values were plotted versus the voltage output and fitted to an equation of the form $FR = a * V + b$, where FR is the flow rate in GPH, V is the voltage output, and a and b are constants. Solving for a and b gave the equation

$$P = 1739.81 * V + 1394.01, \tag{5}$$

with an R^2 value of ~ 1 . Figure 20 shows the calibration curve, the measured value of flow rate versus the value calculated using Eq. 5. All of the data points except the first are within the $\pm 2\%$ lines.

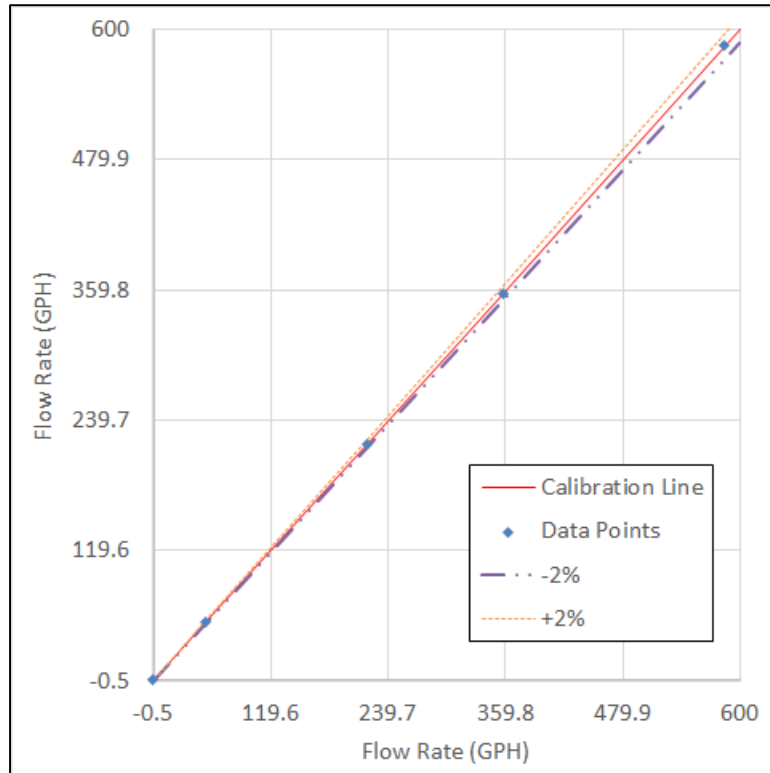


Figure 20. Calibration curve for Krohne® Optiflux-1300 flow meter

Two T-type thermocouple probes (Omega® EN60584-2, Class 1), with accuracy of $\pm 0.5^{\circ}\text{C}$, were installed in the system: one in the tank, and one at the bottom of the system near the pump inlet. Figure 21 shows these two thermocouples. These thermocouples were connected to the facility’s data-acquisition system to measure and record the temperature in the system during the course of each experiment.

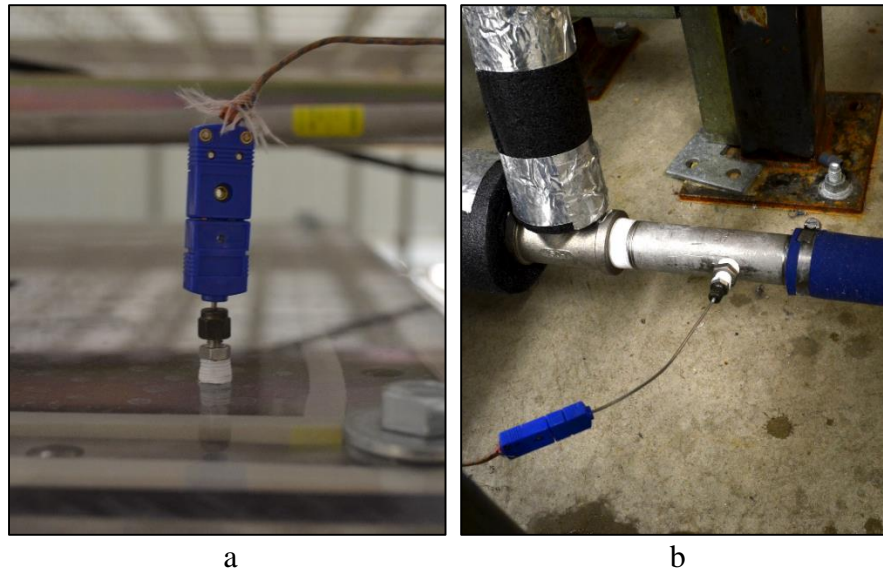


Figure 21. Tank-mounted thermocouple (a) and pump-inlet thermocouple (b)

A camera (16.2MP DSLR) was set up in front of the test section to record the development of the debris bed during the course of each experiment. A relay circuit, triggered by a voltage output from the data-acquisition system, was used to take a picture every five seconds. The camera and its triggering circuit can be seen in Figure 22.

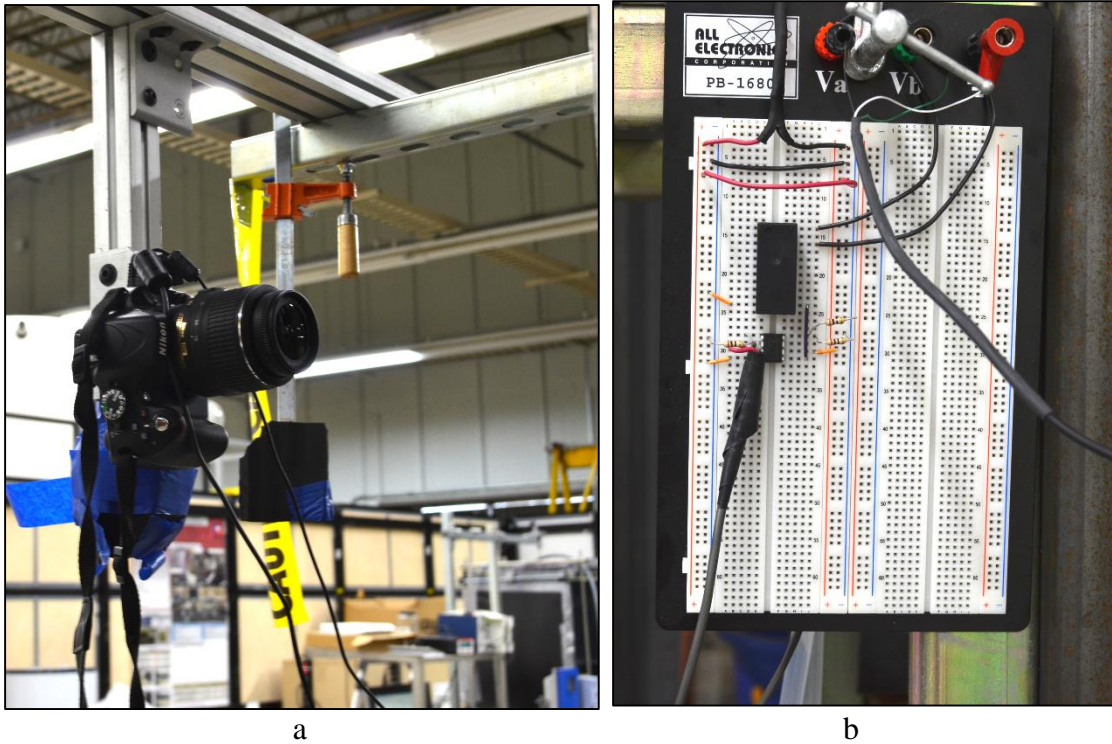


Figure 22. (a) Camera and (b) its triggering circuit

As mentioned before, a data-acquisition system was incorporated into this facility. The system used was a National Instruments (NI) SCXI-1000 with input and output terminal blocks (Figure 23). During the experiment, this system recorded temperature, flow rate, and differential pressure across the test section. It was also used to generate the output signal which triggered the camera to take pictures of the debris bed.



Figure 23. National Instruments SCXI-1000 data acquisition system

The control panel is the facility's operator interface. Figure 24 shows the main components of the control panel.

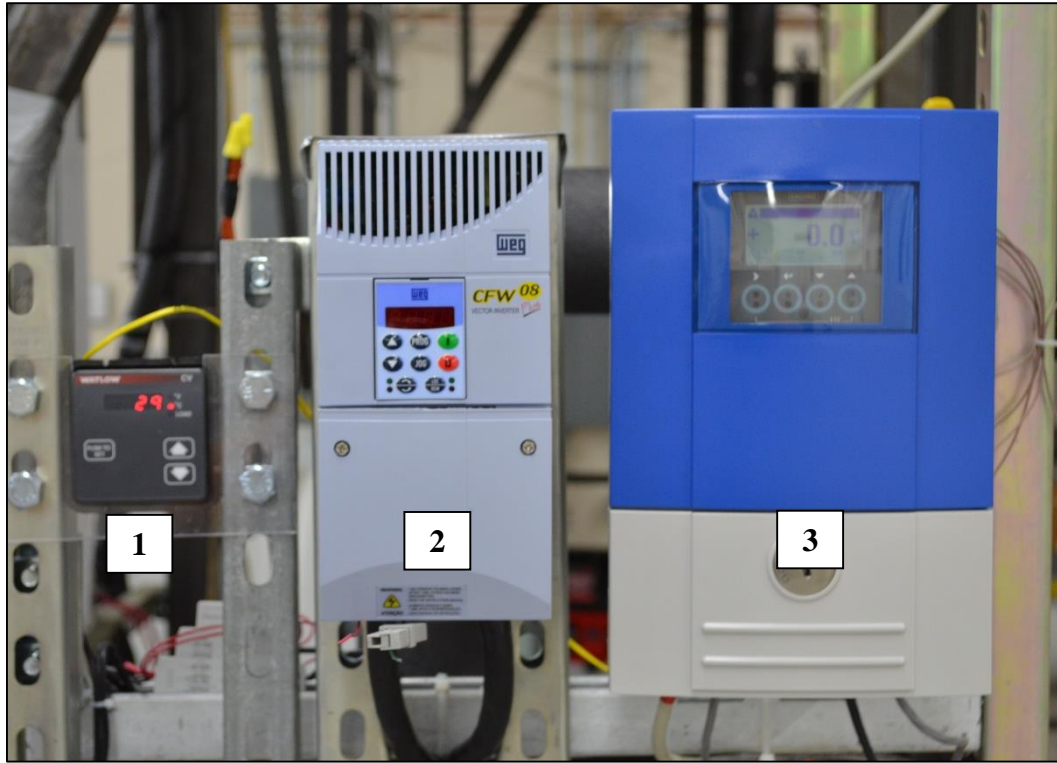


Figure 24. System control panel

The numbered components shown in Figure 24 are listed in Table 6, below.

Table 6. Control panel components

Component Number	Component Description
1	Thermostat for external tape heaters
2	Variable frequency drive for controlling pump speed
3	EM-flow-meter signal conditioner

To facilitate any high-temperature experiments that might be required, two immersion heaters, with a total power of 6 kW, were installed downstream of the pump

in a heating loop, as shown in Figure 25. Before starting a high-temperature experiment, the flow of water can be forced to circulate through the heating loop until the desired temperature is achieved. During the experiment, the heating loop can be isolated using valves.



Figure 25. Heating loop (6 kW)

3.2 Automated Microscope Imaging System

3.2.1. General System Description

Two similar microscope systems were developed for size characterization of fibrous-debris particles. The main components of these two systems are: a camera with an attached microscope objective, three motor-driven linear slides, two motor controllers, a sample stage, a backlight, a cooling fan, and a computer. Figure 26 shows the setup of the system.

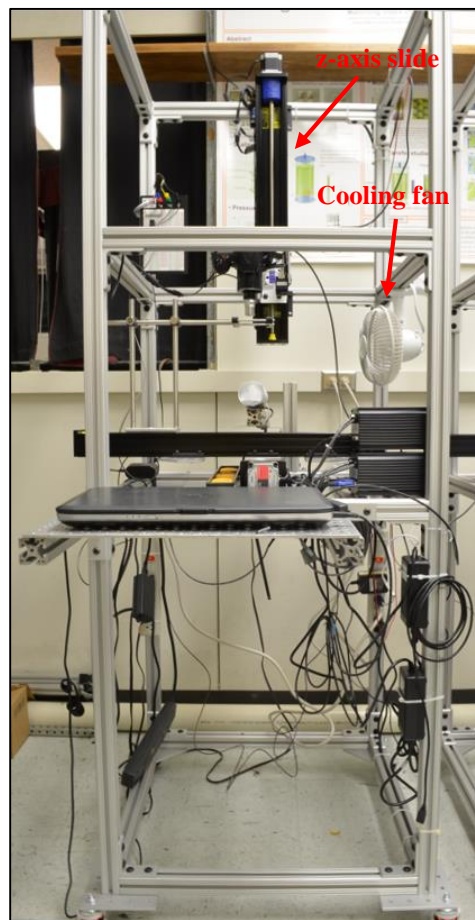


Figure 26. Automated microscope imaging system (AMIS)

The sample stage was mounted onto a motor-driven linear slide (the x-axis slide). This slide was then mounted onto a second motor-driven linear slide (the y-axis slide) so that the directions of movement of the two slides are orthogonal to one another. These two slides are connected to a single motor controller, which allows the movement of the sides to be synchronized. The motor controller is also connected to the camera and is used to generate a voltage output signal that triggers the camera shutter. A computer, equipped with a software called COSMOS, is connected to this slide-motor controller and is used to effectively scan a 20 mm x 20 mm area of the debris sample. Figure 27 shows the slides and motor controllers.

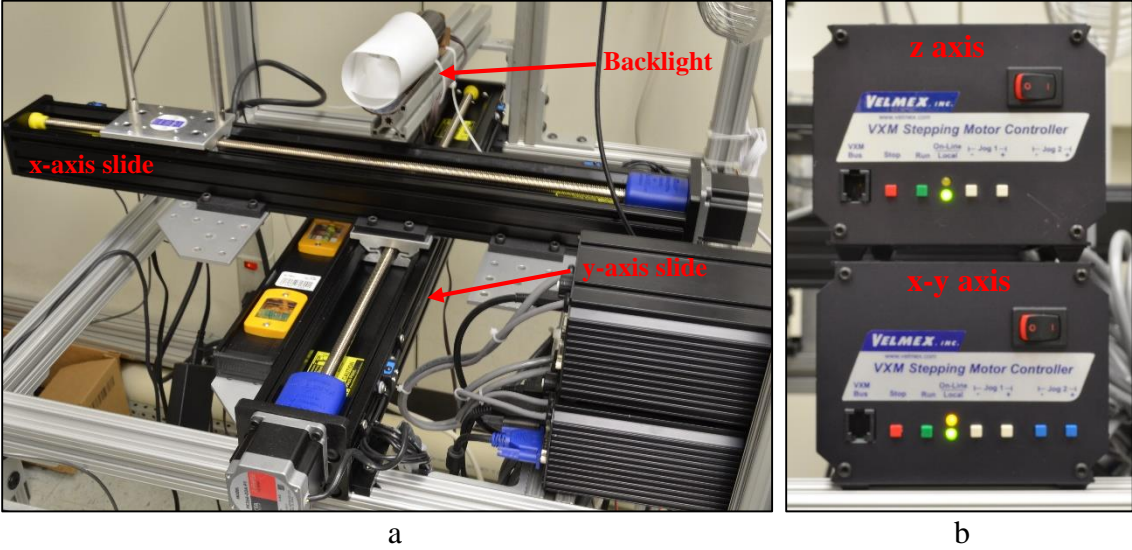


Figure 27. x and y-axis slides (a) and slide-motor controllers (b)

The third motor-driven linear slide (the z-axis slide) is used for focusing the camera. This slide, with the camera mounted on it, is positioned orthogonally to the other two. The slide is controlled manually using the second slide-motor controller. Each sample is placed on the sample stage and illuminated by the backlight (Figure 27). A cooling fan (Figure 26) keeps the sample cool while the backlight is on.

The microscope systems differ in two ways: 1) the type of camera that is used and 2) the magnification of the microscope objective attached to each camera. System 1 (AMIS-1) is equipped with a 36.3 MP DSLR camera and a 10X-magnification microscope objective (Figure 28). The voltage signal from the motor controller in this system goes to a relay circuit (Figure 28.b) that triggers the camera shutter in the DSLR camera. System 2 (AMIS-2) has a 10.6 MP CMOS camera with a 4X magnification microscope objective (Figure 29). This camera is connected to the computer through a USB port, and the camera properties are adjusted using the software included with the camera.

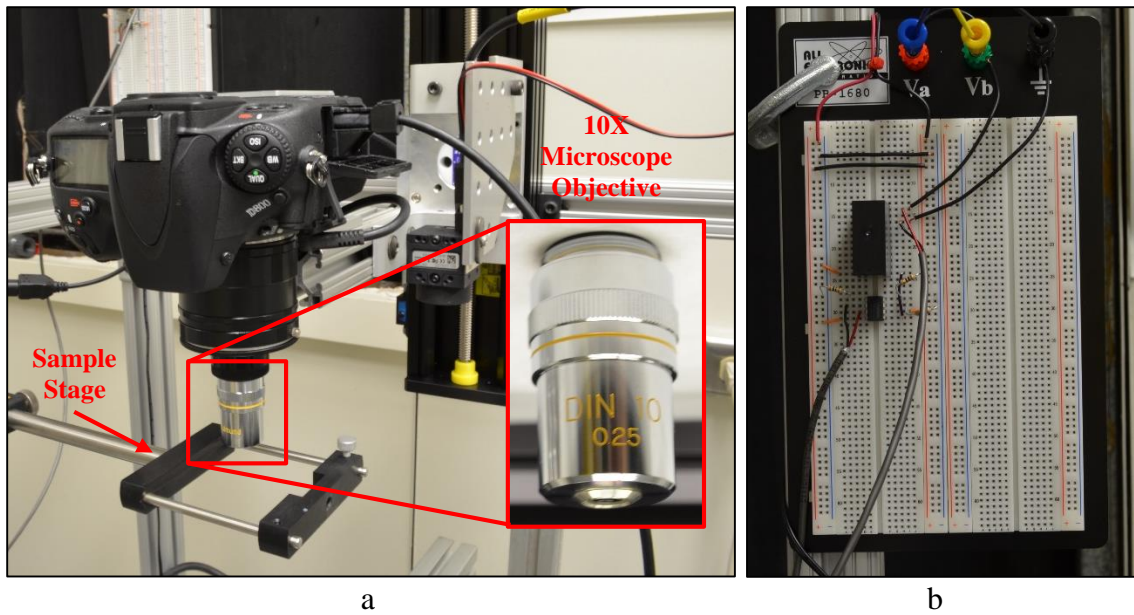


Figure 28. AMIS-1: DSLR camera with 10X microscope objective (a) and its triggering circuit (b)

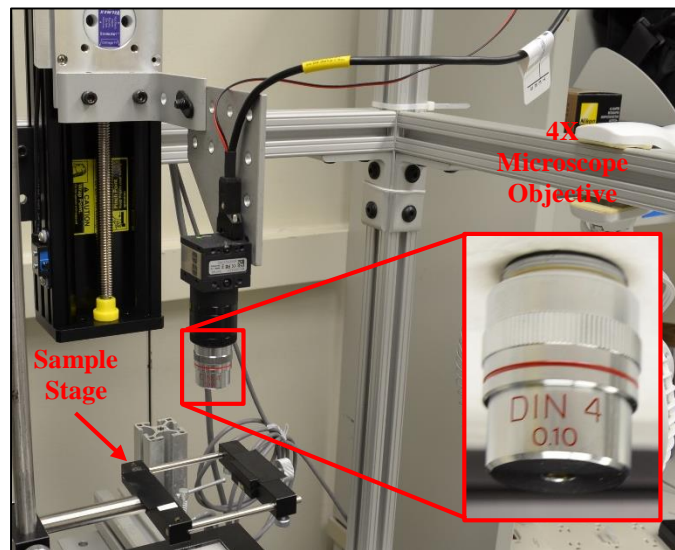


Figure 29. Camera with 4X microscope objective

3.2.2. Calibration and Validation of AMIS

AMIS-1 was calibrated using a NIST traceable Klarmann Rulings, Inc. KR-838 stage micrometer (Figure 30). This micrometer is 25 mm in length with divisions of 0.010 mm.



Figure 30. Klarmann Rulings, Inc. KR-838 stage micrometer

An image of this micrometer taken using AMIS-1 is shown in Figure 31, with a zoomed-in view to show detail.

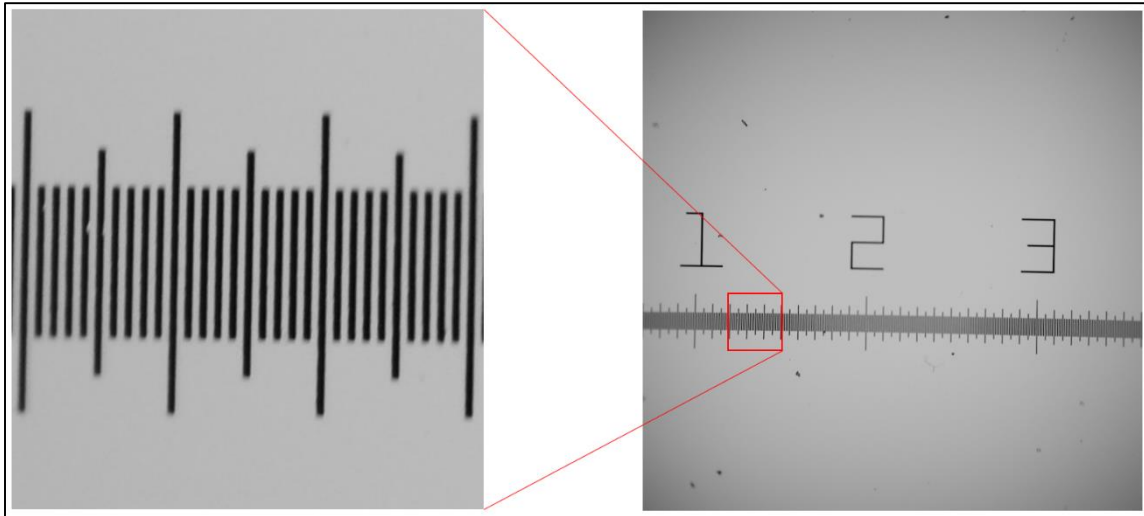


Figure 31. Image of a KR-838 stage micrometer taken using AMIS-1

Using the image of the stage micrometer in ImageJ, the pixel-to-length ratio was calculated to be 1.679 pixels/ μm for AMIS-1. Given this pixel-to-length ratio and that the size of square images taken using AMIS-1 are 24.13 MP, the picture dimensions were calculated. The motor step size of 5 $\mu\text{m}/\text{step}$ and the area of sample to be analyzed ($\sim 20 \text{ mm} \times 20 \text{ mm}$) were used to determine the required number of pictures for imaging the total sample with an overlap of half of the picture length between each image. The specifications of AMIS-1 are shown below, in Table 7.

Table 7. Specifications of AMIS-1

Size of one pixel (μm)	0.595
Single picture dimensions (mm)	2.93 x 2.93
Number of pictures per sample	169 (13 x 13)
Total image area (mm)	20.5 x 20.5
Measurement range (μm)	10 – 500

To validate the accuracy of the size measurements from AMIS-1, four different mono-sized particle standards were used. The results of this validation are presented in Figure 32. The information for the size standards used is shown in Table 8.

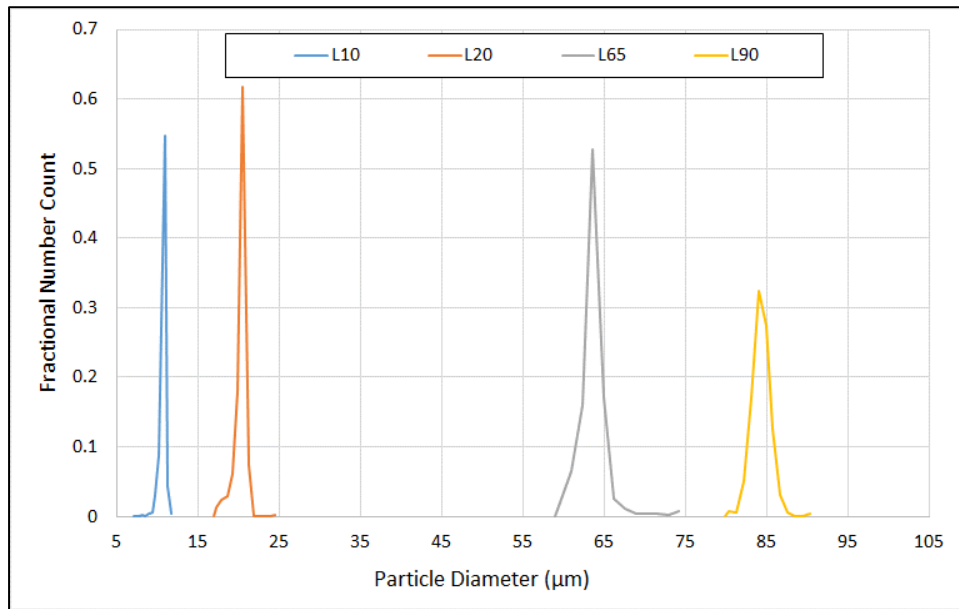


Figure 32. Particle measurements for Coulter CC Size Standards from AMIS-1

Table 8. Size information of mono-sized particles and measurements from AMIS-1

Particles*	Nominal Size (μm)	Assay Value (μm)	Measured Diameter (μm)	Difference (μm)
L10	10	10.35	10.67	0.32
L20	20	20.50	20.22	0.28
L65	65	63.13	63.63	0.5
L90	90	85.42	84.25	1.17
* COULTER CC Size Standard LXX, (NIST Traceable Latex Beads)				

Sample images of two different particle sizes have been included below (Figure 33 and Figure 34). Each image is show before and after processing.

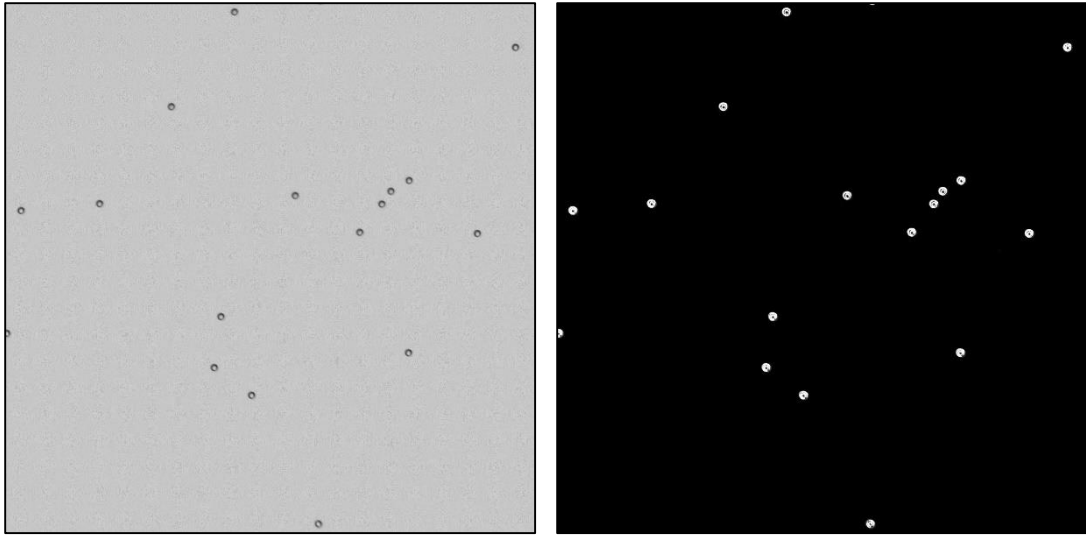


Figure 33. Original (left) and processed (right) image of L10 particles from AMIS-1

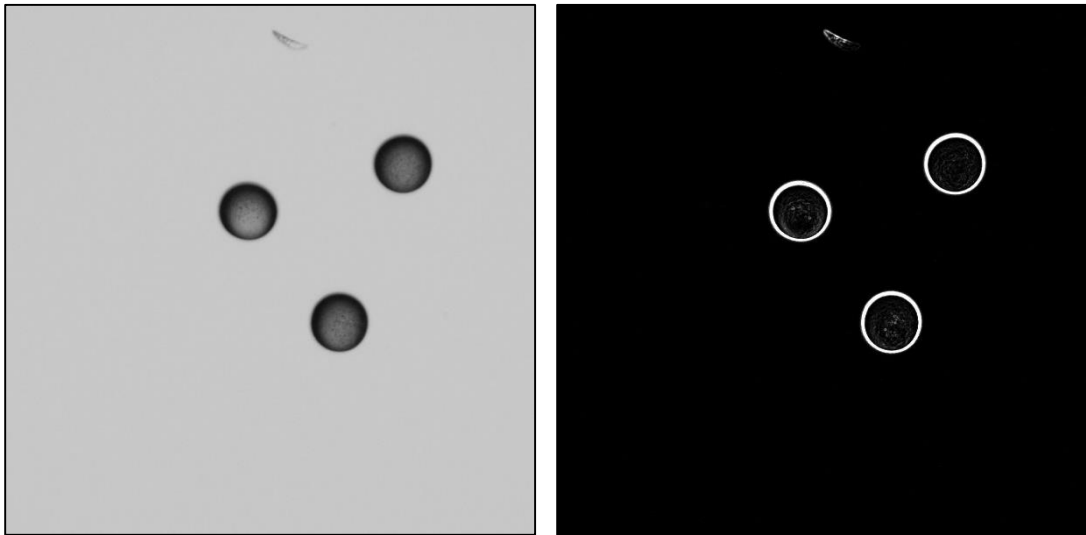


Figure 34. Original (left) and processed (right) image of L90 particles from AMIS-1

AMIS-2 was also calibrated using the Klarmann Rulings, Inc. KR-838 stage micrometer (Figure 30). An image of this micrometer taken using AMIS-2 is shown in Figure 35, with a zoomed-in view to show detail.

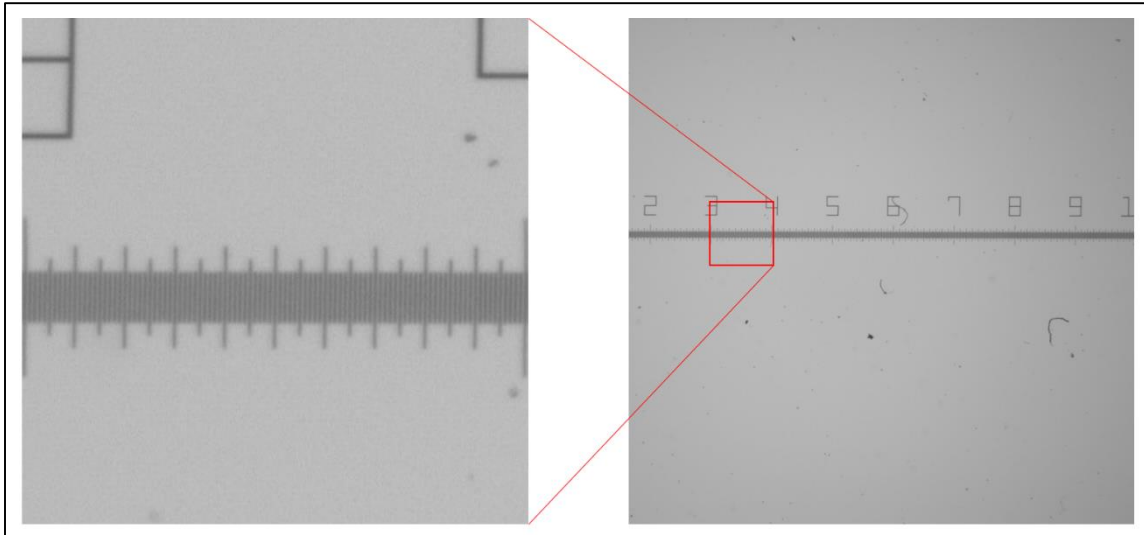


Figure 35. Image of a KR-838 stage micrometer taken using AMIS-2

Using Figure 35 in ImageJ, the pixel-to-length ratio was calculated to be 0.3307 pixels/ μm for AMIS-2. Given this pixel-to-length ratio and that the size of square images taken using AMIS-2 are 7.55 MP, the picture dimensions were calculated. The motor step size of 5 $\mu\text{m}/\text{step}$ and the area of sample to be analyzed ($\sim 20 \text{ mm} \times 20 \text{ mm}$) were used to determine the required number of pictures for imaging the total sample with an overlap of half of the picture length between each image. The specifications of AMIS-2 are shown below, in Table 9.

Table 9. Specifications of AMIS-2

Size of one pixel (μm)	3.024
Single picture dimensions (mm)	8.31 x 8.31
Number of pictures per sample	16 (4 x 4)
Total image area (mm)	20.8 x 20.8
Measurement range (μm)	100 – 2500

To validate the accuracy of the size measurements from AMIS-2, two different mono-sized particle standards were used. The results of this validation are presented in Figure 36. The information for the size standards used is shown in Table 10.

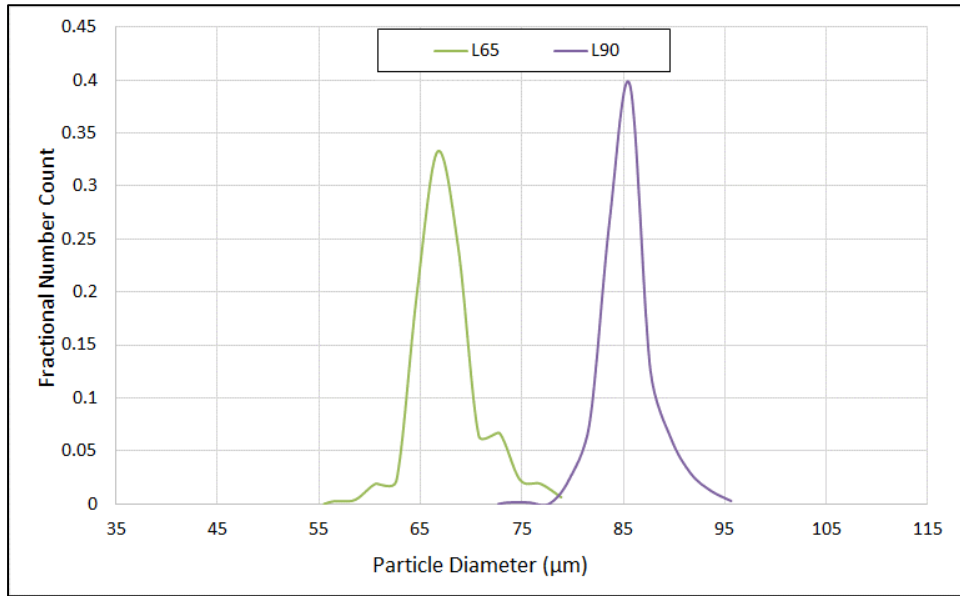


Figure 36. Particle measurements for Coulter CC Size Standards from AMIS-2

Table 10. Size information of mono-sized particles and measurements from AMIS-2

Particles*	Nominal Size (µm)	Assay Value (µm)	Measured Diameter (µm)	Difference (µm)
L65	65	63.13	67.67	4.54
L90	90	85.42	85.50	0.08
* COULTER CC Size Standard LXX, (NIST Traceable Latex Beads)				

Sample images of two different particle sizes taken with AMIS-2 have been included below (Figure 37 and Figure 38). Each image is show before and after processing.

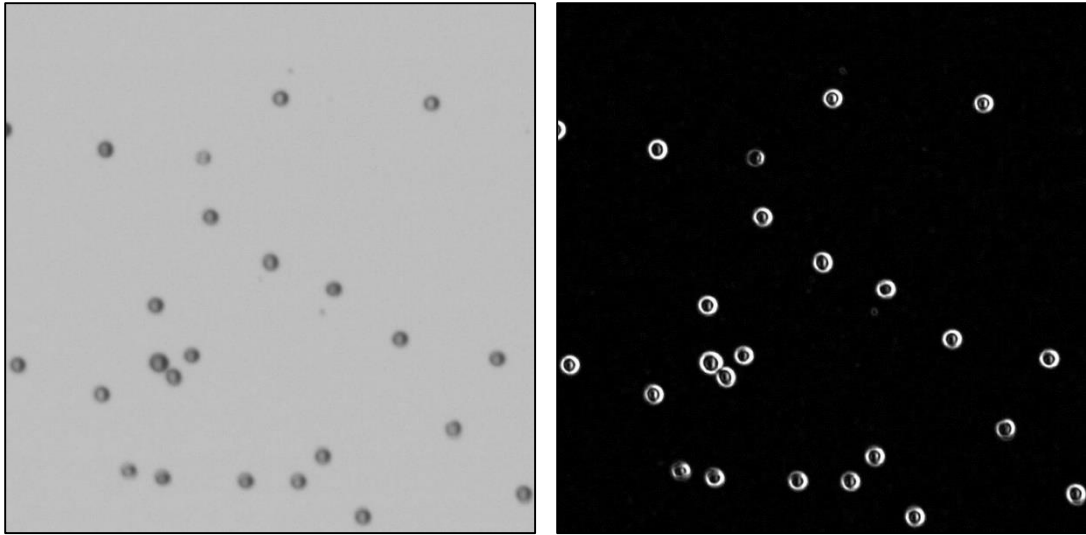


Figure 37. Original (left) and processed (right) image of L65 particles from AMIS-2

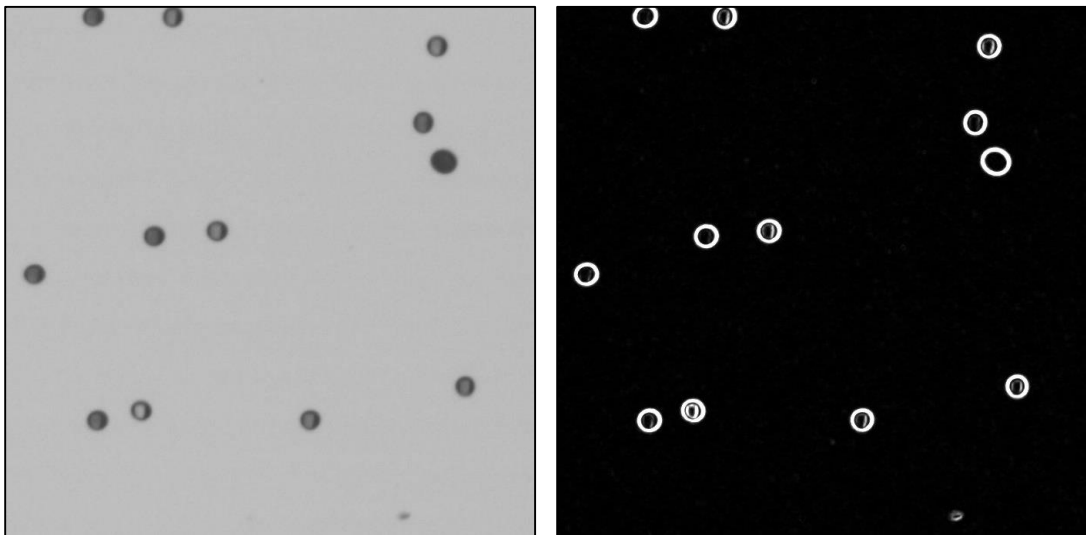


Figure 38. Original (left) and processed (right) image of L90 particles from AMIS-2

3.3 Beckman Coulter Multisizer 3

A Beckman Coulter Multisizer 3 (Figure 39) was used in an attempt to obtain a PSD for the fibrous debris in the range from 0.6-18 μm . This was done using a tube with a 30 μm aperture. Because there were fibers appreciably larger than 30 μm in the samples, this instrument was not able to provide reliable results. It did however, produce results for other particles types. This will be discussed further in the results section.



Figure 39. Beckman Coulter Multisizer™ 3 COULTER COUNTER [13]

The Multisizer 3 Coulter Counter operates using the Coulter Principle, or electrical sensing zone (ESZ) method. Particles are suspended in an electrolytic solution. A metering pump is used to force the solution to flow through a small aperture in a tube that separates two electrodes. As particles enter the aperture they displace their volume of the conducting fluid. This leads to an increase in the impedance across the two electrodes. After processing this current signal and converting it into a voltage pulse, which is proportional to the volume of the particle in the aperture, it is measured and displayed by the Multisizer 3 software. A simple schematic of the Multisizer 3 is presented in Figure 40.

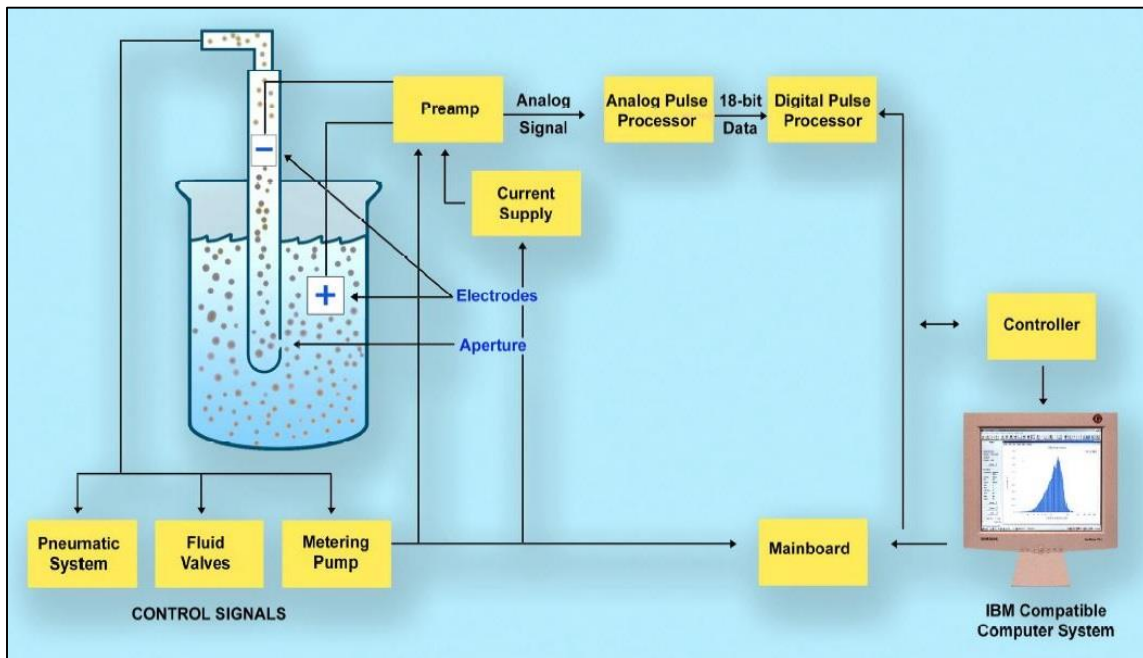


Figure 40. Schematic of the Beckman Coulter Multisizer 3 [14]

The exterior of the system, with important components labeled, is shown in Figure 41.



Figure 41. Multisizer 3 exterior components [14]

The aperture viewer is used to view the aperture while the system is running to ensure that it is not blocked. Two dials are located on the left side of the machine and are used to control the stirrer, which keeps the particles suspended in the solution while samples are being analyzed. The top dial is used to switch the rotational direction of the stirrer, while the bottom dial controls the speed with which the stirrer rotates. Figure 42

shows the sample compartment with the glass door open and points out the components inside.

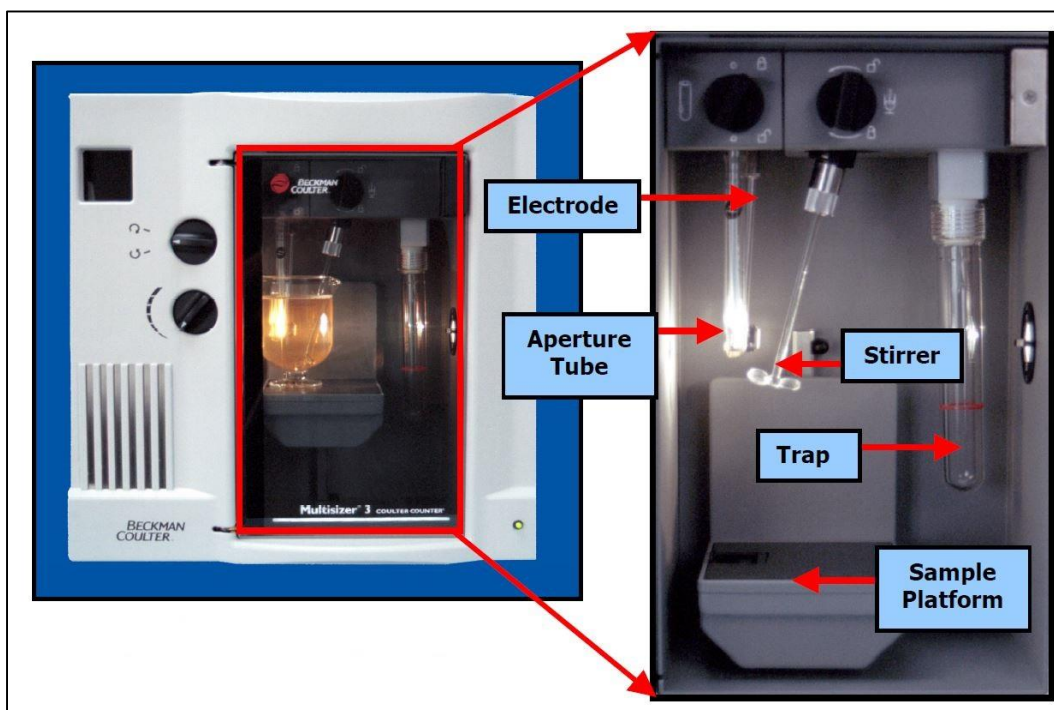


Figure 42. Sample compartment of the Multisizer 3 [14]

In the above figure, the locations of the external electrode, aperture tube, and stirrer can be seen. Directly above the aperture tube is a knob used for holding and releasing the tube; this is used for changing the aperture tube. Above the stirrer is a knob used for adjusting the stirrer position. The trap is installed with the purpose of preventing large or dense particles from making their way into components downstream of the aperture tube. The height of the sample platform is adjustable.

3.4 NanoSight LM10

3.4.1. General System Description

The NanoSight (Figure 43) is based on a conventional microscope. This instrument utilizes a laser as a light source for illuminating nanoscale particles that are suspended in a fluid. With a near-perfect black background in the viewing chamber, the particles appear individually as point-scatters moving under Brownian motion. A scientific CMOS (sCOMS) camera is connected to the microscope and is used for recording the motion of these particles in the sample. The NTA image analysis software automatically tracks and sizes particles simultaneously [15].

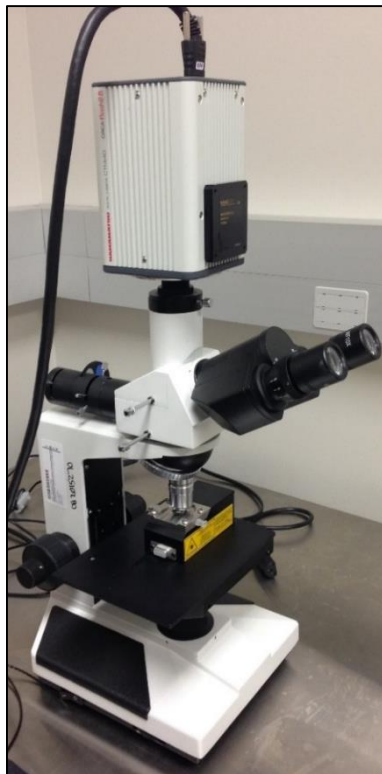


Figure 43. NanoSight LM10

The samples are injected into the viewing unit (Figure 44) which houses the glass optical flat and laser.

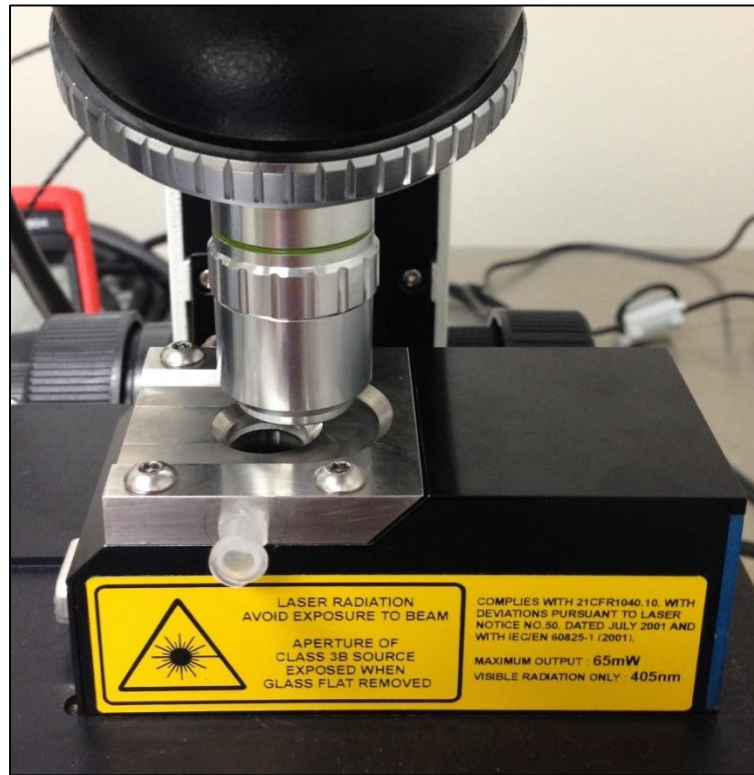


Figure 44. Sample-viewing unit showing the viewing window

3.4.2. Determining a Required Number of Completed Tracks

Due to the low concentration of particles in the samples that were analyzed on this system (especially the downstream sample) it was necessary to run this system for an extended amount of time, allowing a statistically significant number of particles to be tracked. A comparison of the results obtained for different numbers of completed tracks

was made in order to determine a reasonable track requirement for sample analysis. The numbers of tracked particles selected for comparison were: 100, 200, 500, 1000, and 2000. Figure 45 presents the histograms for samples run with the numbers of tracked particles previously listed. For ease of comparison, the number count versus the maximum bin value was put into a scatter plot as opposed to the column plot typically used for histograms.

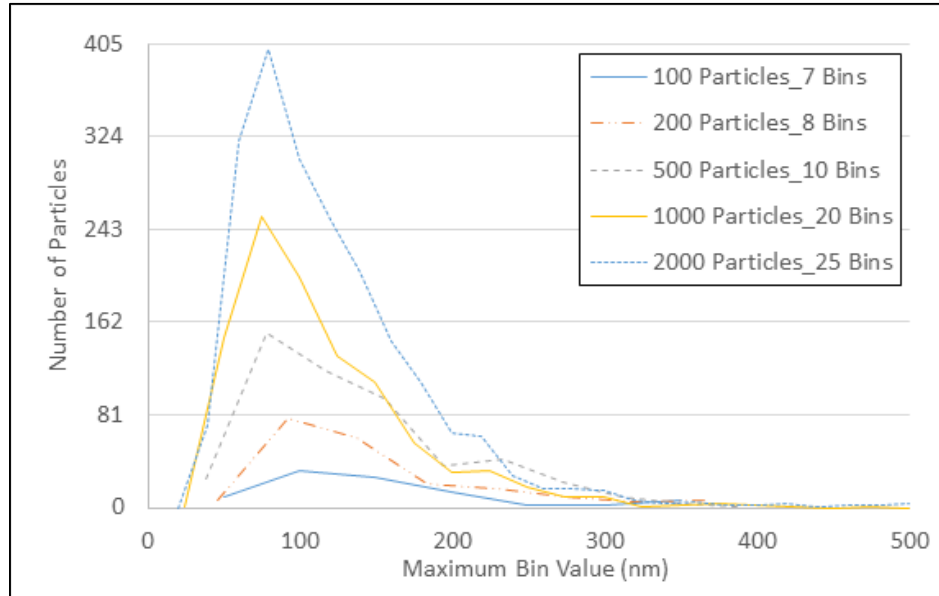


Figure 45. Number count versus maximum bin value for different numbers of tracked particles

It is important to note that in the above plot each of the lines, corresponding to different completed-track numbers, uses different bin widths which are shown in the legend. To determine the appropriate number of required tracks, the comparison needed

to account for different numbers of particles as well as different numbers of bins. To normalize the plots, first each bin value was simply divided by the total number of particles tracked in the sample.

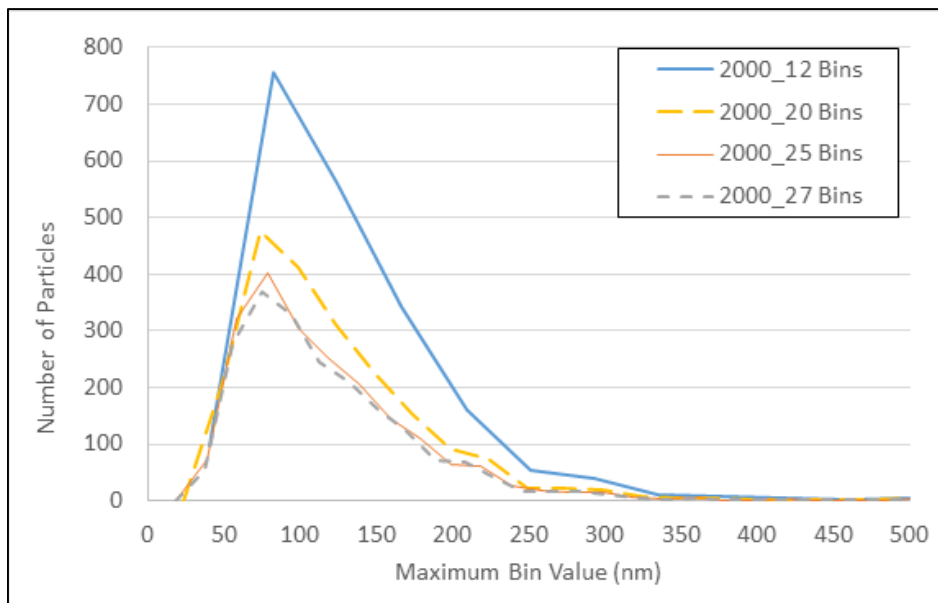


Figure 46. Number count versus maximum bin value for 2000 tracked particles with different numbers of bins

Since the histograms in Figure 46 show an inverse proportionality between the number of particles in the bins and the number of bins used, normalization was done by simply multiplying the value in each bin by the number of bins. Figure 47 shows the normalized plot from Figure 46 for comparison of histograms with different numbers of bins.

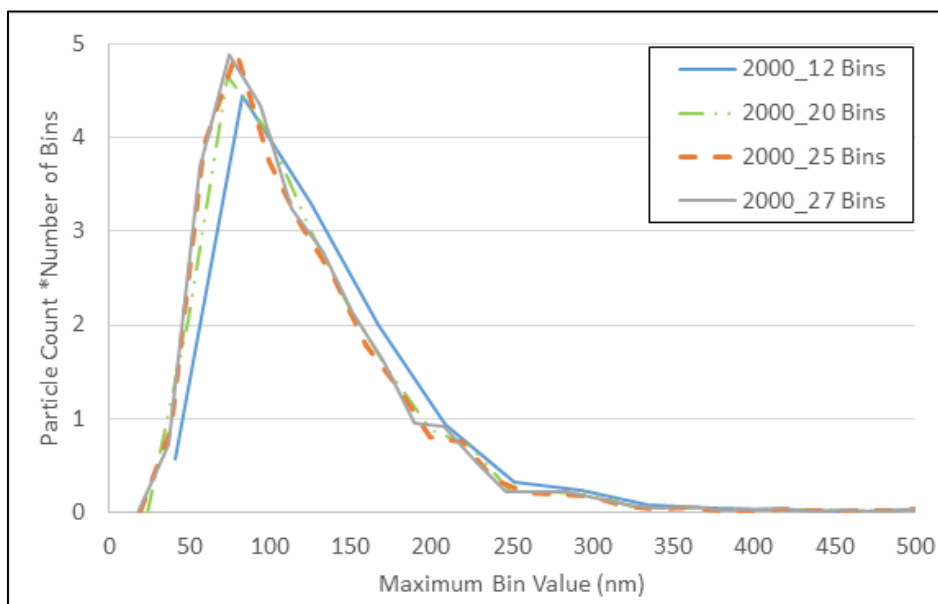


Figure 47. Normalized count versus maximum bin value for 2000 tracked particles with different numbers of bins

Since the plots in Figure 47 showed good agreement among different binning values, this method was applied to the plots in Figure 45. For each histogram in Figure 45, each bin value was multiplied by the following factor: $\frac{\text{number of bins}}{\text{total number of particles tracked}}$. This allowed for a comparison and a determination of the required number of particle tracks to be made; the plot of this is shown below, in Figure 48.

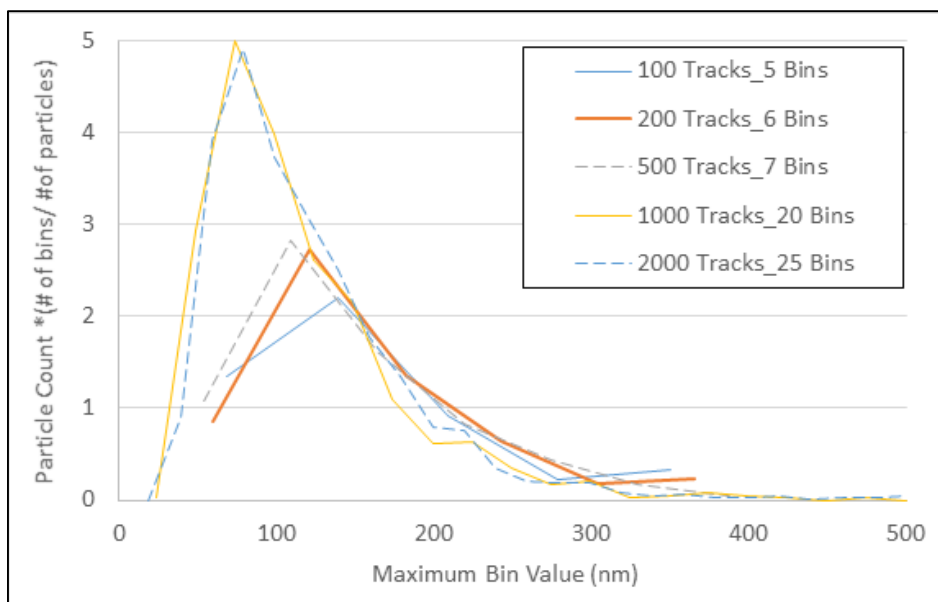


Figure 48. Normalized histograms for comparison of tracked-particle number from NanoSight LM10

Very little change was observed between the normalized graphs for 1000 and 2000 tracked particles, it was then decided that tracking 1000 particles with the NanoSight LM10 was sufficient for producing a statistically accurate particle size distribution.

4. EXPERIMENTAL PROCEDURES

4.1 Vertical-Flow Sump-Strainer Loop

The experimental procedure for the vertical-flow sump-strainer loop is divided into five parts:

1. Experiment preparation
2. Setting the flow rate of the isokinetic sampling port
3. Debris preparation
4. Running the experiment
5. Experiment completion and system cleaning

4.1.1 Experiment Preparation

With the experimental facility cleaned after the previous experiment (see section 4.1.5 for the cleaning procedure), the downcomer pipe support (Figure 49) was loosened and the test section and cleaning filter were removed. The strainer was then installed in the test section.

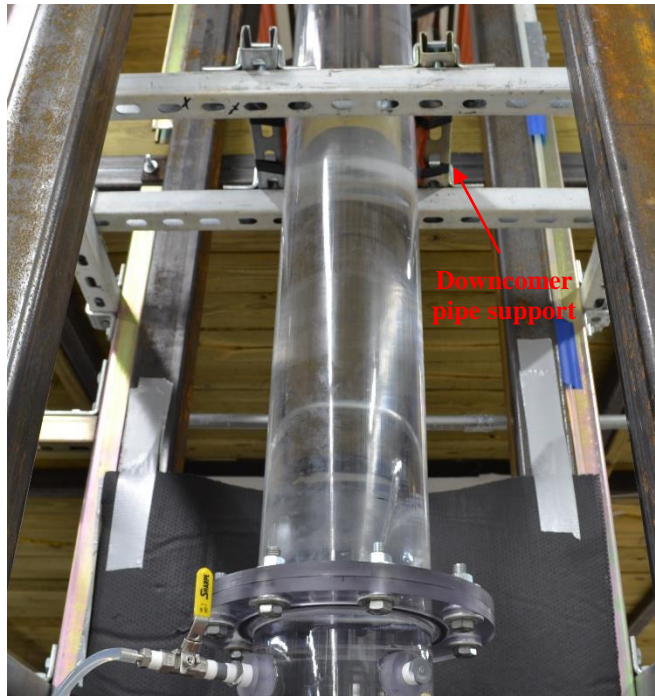


Figure 49. Downcomer pipe support

A $1\mu\text{m}$ heat-welded polyester felt bag with a plastic-ring head of 10.16 cm was used as a bypass filter downstream of the test section. The system was partially filled with filtered tap water so the filter could be completely submerged during installation; this reduced the number of air bubbles downstream of the strainer. To prevent debris from bypassing the filter bag, a silicone gasket was used as a seal between the plastic-ring head of the filter bag and the pipe wall. The location of the filter bag in the pipe can be seen in Figure 50.



Figure 50. Approximate location of the filter bag installation

The test section was put back into the system and bolted in place. The downcomer support was tightened to secure the piping. The tubes from the pressure transducer were connected to their respective taps on the test section, and valves DP1 and DP2 (Figure 15) were both opened. The tube for the isokinetic sampling port was connected to valve SP1 (Figure 15), which was then opened. At this point, system filling resumed with the flow rate being momentarily reduced as the water level reached the strainer, in order to prevent bubbles from being trapped under it. Once the water level in the tank reached a height of 20 in, system filling was stopped. The pump then turned on and the variable frequency drive was used to set the desired flow rate, 54 GPH in this case. This volumetric flow rate was selected to achieve a fluid approach velocity of 0.3 cm/s in the test section. The valves on the pressure transducer were opened in order to

bleed the air from the transducer tubing, after which, the signal conditioner was zeroed. To remove the air from the isokinetic sampling port tubing, valve SP2 (Figure 15), located on the third floor, was opened until no bubbles could be seen in the line. The Labview Virtual Instrument (VI) was prepared to record the temperature, differential pressure, and flow rate, as well as to trigger the camera during the course of the experiment. After mounting the camera, a sample picture was taken to ensure the desired image quality. The final step in preparation for the experiment was to collect and label 13 one-liter bottles; the type of sample bottle used can be seen in Figure 51. These bottle were used for the continuous collection of sample from the port downstream of the strainer.



Figure 51. One-liter bottle for downstream sampling

4.1.2 Setting the Flow Rate of the Isokinetic Sampling Port

Once the system had been prepared for the experiment, four gallons of filtered tap water (the volume added during debris injection) were added to the tank at the top of the system. A small container was placed on a scale below valve SP2 and the scale was zeroed. The scale used was an Acculab® VI-2400 (Figure 52). The specifications of this scale are given in section 3.1 Vertical-Flow Sump-Strainer Loop.



Figure 52. Scale used for setting the sampling port flow rate

Valve SP2 was opened and a timer was started simultaneously. The mass flow rate of the water from valve SP2 was then adjusted as necessary to achieve a rate of 1.509 g/s; this was done using the manual-linear slide which valve SP2 was secured to.

The scale was checked at the intervals specified in Table 3. Once the sampling flow rate was set, water was drained from the system into a bucket until the tank level again reached 20 in.

4.1.3 Debris Preparation Using the NEI Protocol

The NEI protocol [12] was developed by the Nuclear Energy Institute in 2012 and was adopted for this research in order to produce fine debris as defined by this protocol. A description of the steps followed to produce the debris used for each test is reported in this section.

The first step was to sample and weigh the NUKON Debris. A sample was cut from a NUKON heat-treated mat (PCI 2.5" x 24" x 48", Lot #10958HT). The NUKON mat from where the samples were taken is shown in Figure 53. The sample was then trimmed on the edges in order to achieve the desired weight of NUKON, 6.6 g.



Figure 53. One-side baked NUKON® mat

All cuts were performed in a way that preserved the full thickness of the sample, in order to conserve the original characteristics of the heat treated mat. Cutting was complete once the weight displayed on the scale was steady (Figure 54). The scale that was used was an Acculab® VI-350. This scale has a measuring range of 0 – 350g and readability of 0.01g. The calibration of the scale was verified using the following NIST certified weights:

- 1 g ± 0.0009 g
- 5 g ± 0.0015 g
- 10 g ± 0.002 g
- 50 g ± 0.01 g

All the possible combinations of these weights were verified.



Figure 54. Weighing the NUKON debris

Next, the sample was separated into four layers of approximately equal thickness: two dark layers, the side of the mat in contact with the hot surface used during heat treatment, and two light layers, the opposite side of the NUKON mat (Figure 55).



Figure 55. Layer separation

These layers were then cut into smaller pieces, approximately $2.54 \text{ cm} \times 2.54 \text{ cm}$. The pieces from the light layers were additionally torn. This reduced-size debris can be seen in Figure 56.



Figure 56. Manual debris size reduction

The debris was then placed into a plastic bucket (capacity \approx 19 liter) and approximately 2 liters of filtered tap water were added to slightly cover the debris pieces (Figure 57).



Figure 57. Reduced-size debris inside of the five-gallon mixing bucket

The next step was to break down and mix the debris. For this phase, a high-pressure (12.4 MPa, 1800 psi) washer was used, and a lid with a small hole was put on the bucket in order to avoid any spilling of water (Figure 58). The jet, which used a 40°-angle nozzle, was kept submerged in the water in the bucket the entire time that it was running. The jet gun was moved randomly inside the bucket to allow uniform breaking and mixing. Spraying was ceased when the final amount of water in the bucket was approximately 4 gallons. This allowed for the production of uniform debris.

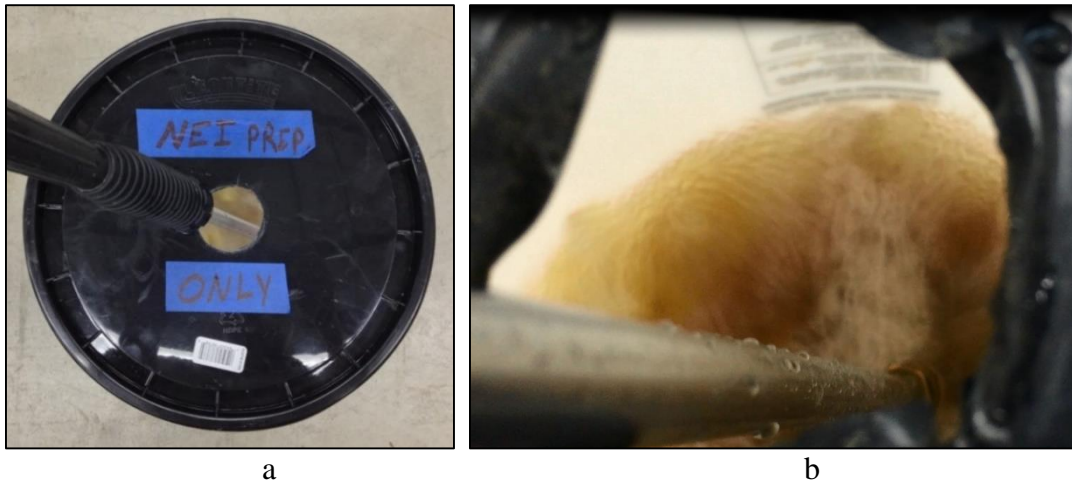


Figure 58. Pressure washer mixing –outside (a) and inside (b) of the bucket

Figure 59 shows the final state of the NEI-prepared NUKON debris in a five-gallon bucket and in a glass observation tray.

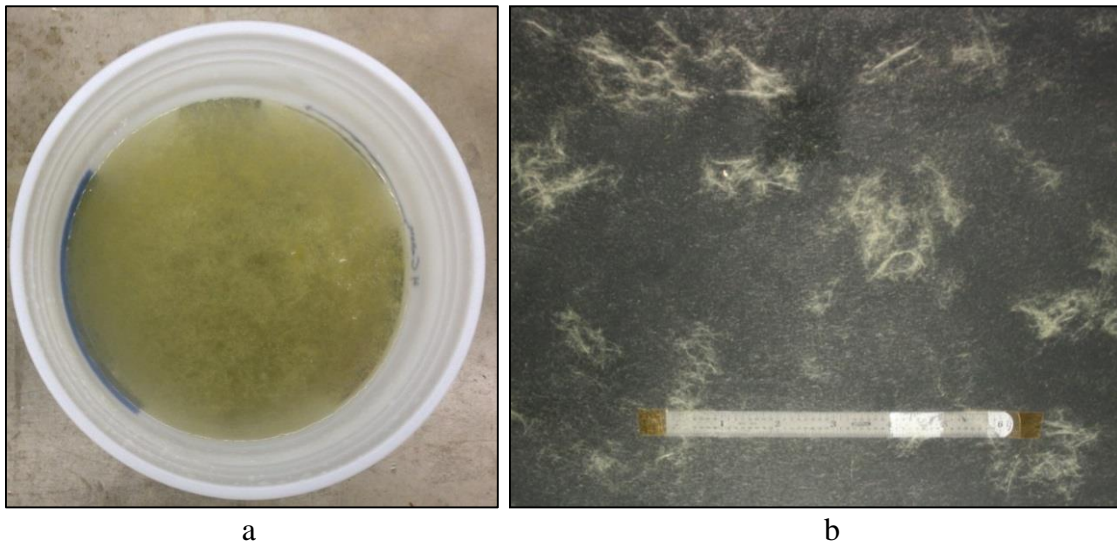


Figure 59. Final state of debris sample in the bucket (a) and in the glass tray (b)

4.1.4 Running the Experiment

Once the flow rates of the system and the sampling port had been set, and the Labview VI was ready to begin logging data, the mixing propeller was powered on and the first one-liter sample bottle was placed under the sampling port valve. The debris previously prepared using the NEI protocol (described in Section 4.1.3 Debris Preparation Using the NEI Protocol), was poured into the water tank over a period of approximately five seconds by the experimental operator on the third floor. Immediately following debris injection, valve SP2 was opened and a timer was started by the third-floor operator, while the first-floor operator initiated data acquisition with the NI system. Throughout the course of the experiment, the sample bottles were changed every 10 minutes, which corresponded to 0.18 turnovers. To keep the water level in the tank nearly constant, approximately 900 ml of filtered tap water were added to the tank immediately following each sample bottle change.

4.1.5 Experiment Completion and System Cleaning

Immediately following termination of the experiment, the first-floor operator stopped the pump and mixing propeller and closed valve V1 (Figure 8), while the third-floor operator closed valve SP2. The third-floor operator then placed a 6 in diameter 1 μm heat-welded polyester felt bag with a plastic-ring head (Figure 60) into the tank outlet pipe.



Figure 60. 1 µm polyester felt filter bag for 6 in pipe

All valves on the test section (SP1, DP1, and DP2) were closed and the tubing for the pressure transducer and sampling port were all disconnected on the test-section side. A drain tube was connected to the upstream pressure tap and valve DP1 was opened to start system draining. Once the water level reached the upstream pressure tap, the drain tube was disconnected and moved to the isokinetic sampling port. The downcomer pipe support was then loosened and the test section's upper-flange bolts were removed. A thin plastic film was inserted between the top flange of the test section and its mating flange on the downcomer. This plastic was then secured to the downcomer using tape. This was done to prevent any water that could possibly drip from the tank or pipe walls from impacting the debris bed, potentially causing further debris bypass through the strainer. Valve SP1 was opened to recommence draining at a rate that didn't exceed the experimental sampling flow rate. After the water level had fallen just below the strainer, valve DP2 was opened and a drain hose was connected to the filter bypass outlet pipe.

Valve FB1, shown in Figure 8, was fully opened at this point to finish draining. Valve FB1, as well as all valves on the test section were closed and the drain tube was disconnected from the sampling port. The test section's lower flange bolts were then removed and the test section extracted. To ensure the collection of all debris that had bypassed the strainer, filtered tap water was poured onto the inner walls of the pipe above the filter bag. The filter bag was then removed and placed on the filter-bag hanger to remove excess water before the filter was to be dried. The 6 in filter bag was removed from the tank and the plastic film was pulled off of the downcomer flange. A system-cleaning filter bag (the same type as that used for collecting the debris bypass) was inserted into the filter bag location downstream of the test section. The test section was disassembled to remove the strainer as well as the debris bed. Any residual debris on the test section walls was rinsed off at this point using filtered tap water. The test section was then reassembled without the strainer and then put back into the system and bolted in place. The downcomer support was tightened. To drain the piping downstream of valve V1, the drain hose is moved from the filter-bypass outlet to the filter-bypass inlet pipe and valve FB2 (Figure 8) is opened.

After draining had been completed, the system was refilled with filtered tap water until the return pipe was submerged (Figure 61). The pump was turned on and the flow rate was increased to ~800 GPH for 30 minutes, after which water was drained from the system until the water level was at the bottom of the tank viewing windows. The system was then run in this condition for more than 12 hours. At the end of the

cleaning period the pump was shut off, the system was drained, and the cleaning filter was removed.



Figure 61. Water level in tank during system cleaning

4.2 Automated Microscope Imaging System

A description of the systems and the components that will be mentioned in this section, can be found in Section 3.2 Automated Microscope Imaging System.

4.2.1 AMIS-1: DSLR Camera with 10X Microscope Objective

To prepare AMIS-1 for use, the first step was to turn on the DSLR camera, the cooling fan (Figure 26), and the backlight (Figure 27). The camera was put into Live View mode so that the image could be seen through the camera's LCD screen. Two

glass slides were then prepared for the sample. One of the slides, the bottom one, had a small piece of electrical tape at each of the corners which acted as spacers to keep a small gap between the top and bottom slides. Both sides of each slide were cleaned using a low-lent delicate-task wiper and a small amount of isopropyl alcohol. Any dust or lent that was left behind was removed using air duster. The sample bottle to be used was shaken to re-suspend any particles that had settled. A 200 μl sample was taken from the bottle immediately after shaking, using a pipette. This sample was put onto the bottom slide and the top slide was put over it carefully, to avoid trapping bubbles in the sample.

Figure 62 presents an image of a prepared sample.

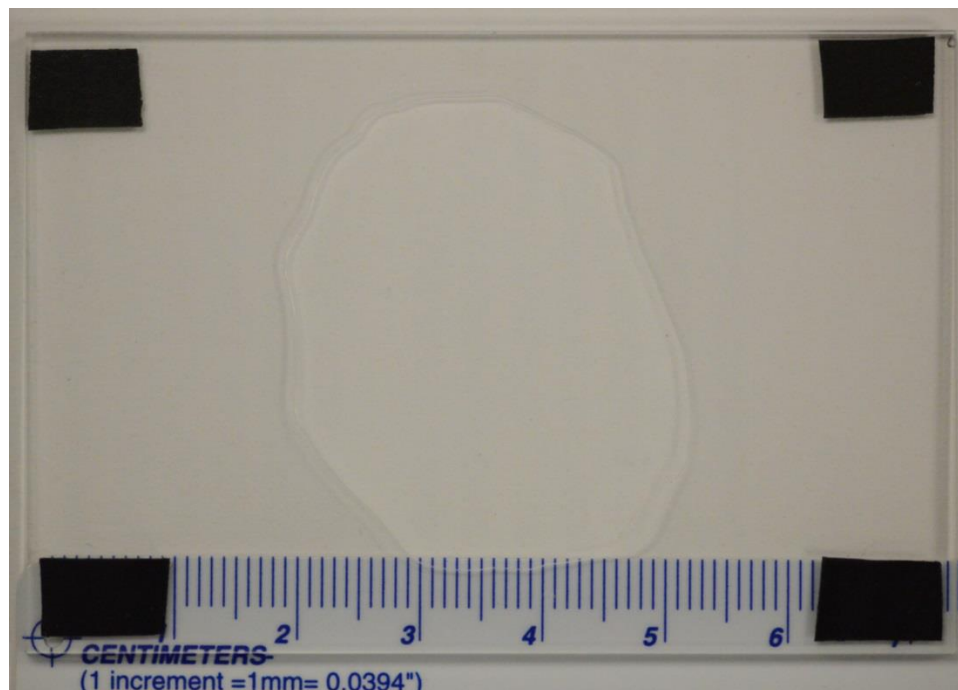


Figure 62. 200 μl wet debris sample prepared for use with the automated microscope imaging systems

Once sample preparation was complete, the sample was placed onto the sample stage (Figure 28) above the backlight. While looking at the camera's LCD screen, the x and y-axis mechanical slides (Figure 27) were used to center the camera display near the bottom-left corner of the sample area, and the z-axis mechanical slide (Figure 26) was used to focus the camera image. A sample picture was taken at this point to ensure that the image was clear. Next, the power supply to the camera-triggering circuit (Figure 28) was plugged in and the camera's data cable was connected to the computer. The COSMOS software, which was used to control the linear-slide motors, was opened and set to "Buffered" mode. A command line to trigger the system was pasted into the command box and executed. For this particular system, the code triggered the camera to take 169 pictures (a square of 13 by 13 images) while scanning the sample area. After execution of the command was completed by COSMOS, the sample was removed from the stage and the slides were cleaned.

4.2.2 AMIS-2: CMOS Camera with 4X Microscope Objective

The first step in the procedure for using AMIS-2 was to prepare the sample. A 200 μl sample was prepared in the same manner described in section 4.3.1. The sample was placed on the stage (Figure 29), and the backlight and cooling fan were turned on. The uEye Cockpit software was opened and the "Monochrome" setting was selected. The attached CMOS camera was opened in the program. The camera was put into "Live View" mode so that a real-time image in the camera software could be used to adjust the image. The x and y-axis mechanical slides were then used to center the camera display

near the bottom-left corner of the sample area, and the z-axis mechanical slide was used to focus the camera. Under the uEye tab, “Auto contrast” was unselected. Under this same tab, the Properties were then opened. The gamma factor was turned off and the exposure time was then adjusted until a desired particle visibility was achieved. Next, the camera-trigger input was enabled and set to 100 μ s, the camera-trigger mode was set to “Falling edge,” and the trigger timeout was set to 200 seconds. Next, the camera was put into continuous-trigger mode and was ready to start recording. The record-video-sequence icon was selected. A new file was created to save the image sequence of the sample, and the JPEG quality of the image sequence was set to 100%. At this point recording was initiated by clicking the Record button in the Record Dialog box. The COSMOS motor controller software was opened and put into “Buffered” mode. A command line to trigger the system was pasted into the command box and executed. For this particular system, the code triggered the camera to take 16 pictures (a square of 4 by 4 images) while scanning the sample area. After execution of the command was completed by COSMOS, the recording in the uEye software was stopped. A program was used to convert the video file created by the uEye program into a series of JPEG images. Finally, the sample was removed from the stage and the slides were cleaned.

4.3 Beckman Coulter Multisizer 3

Before using the Multisizer 3, the computer was turned on and the Multisizer 3 software was opened. In the software the Change Aperture Tube Wizard was selected from the Run menu. Next the electrolyte container had to be filled and the waste

container emptied. The appropriate aperture tube was then selected, and the tube and sample beaker were both washed with distilled water. Table 11 lists the aperture tubes that were available for use at TAMU.

Table 11. Aperture tubes with corresponding size measurement ranges

Aperture Size (μm)	Analysis Size Range (μm)
30	0.6-12.0
50	1.0-30.0
100	2.0-60.0
280	5.6-168.0
560	11.2-336.0
1000	20.0-600.0
2000	40.0-1200.0

After the aperture tube was dry, it was put into to the appropriate location (Figure 63) and locked in place.

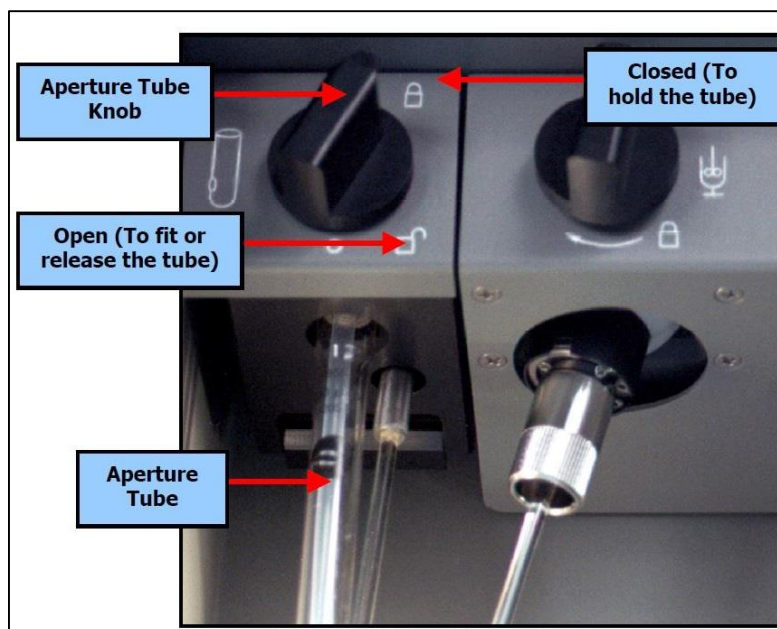


Figure 63. Aperture tube placement in the Multisizer 3 [14]

The sample beaker was filled with clean electrolyte and placed on the sample platform. The platform was raised until the aperture tube was nearly touching the bottom of the beaker. After closing the door, Fill System was selected in the Change Aperture Tube Wizard and the system was filled with the clear electrolyte. After completing the Change Aperture Tube Wizard, the system was run with the clean electrolyte to obtain a background analysis. After saving the results of this analysis, the file was loaded as a background run and was subtracted from all subsequent analyses. At this point the system was prepared for sample analysis.

The sample was then prepared in the beaker using 90 ml of electrolyte and 10 ml of the fibrous-debris mixture to be analyzed. After placing the sample in the sample compartment, the aperture image was focused in the viewing window. Next, the Preview

button was selected in the software. The preview allowed for the concentration of the sample to be checked. The optimal concentration is 10%, and, if needed, electrolyte could be added to reduce the concentration; conversely, fibrous debris would be added to raise the concentration. After achieving the desired concentration, the operator clicked the Start button in the software to begin the particle analysis.

The files produced from each run were exported and saved. The results in the output file from each analysis were directly put into histograms by the Multisizer 3 software.

4.4 NanoSight LM10

First, the viewing unit was disassembled and the viewing window and glass prism were cleaned using a small drop of deionized (DI) water and a low-lent delicate-task wiper. The viewing unit was then reassembled. The scientific CMOS (sCMOS) camera was plugged in and the NTA software suite (Figure 64) was opened on the computer.

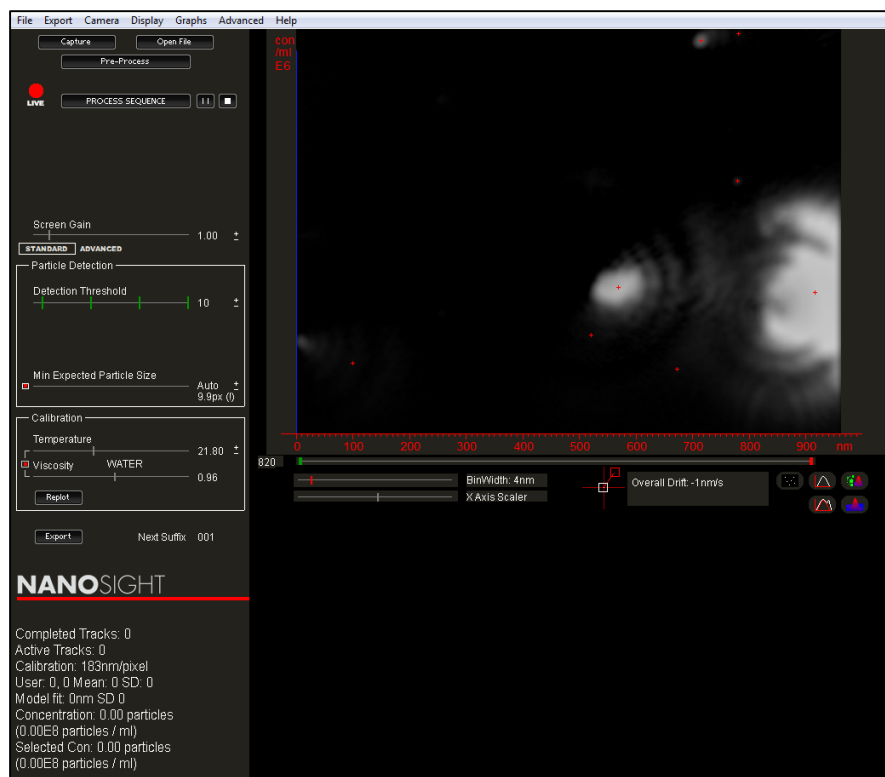


Figure 64. NanoSight NTA 2.3 software

After shaking the sample bottle to ensure mixing and suspension of the fibers, a one-milliliter syringe was used to extract 0.3-0.4 ml. The tip of the syringe was put into the injection port (Figure 65) of the viewing unit and, while holding the viewing unit so that the syringe was oriented upward, the sample was injected until the sample area was completely filled. The sample injection was done slowly enough to ensure that no air bubbles were trapped in the sample-viewing area. After the sample was prepared for viewing, the laser power supply was plugged in, the thermocouple was put into the thermocouple port (Figure 65), and the viewing unit was placed onto the microscope stage; the laser was then turned on.

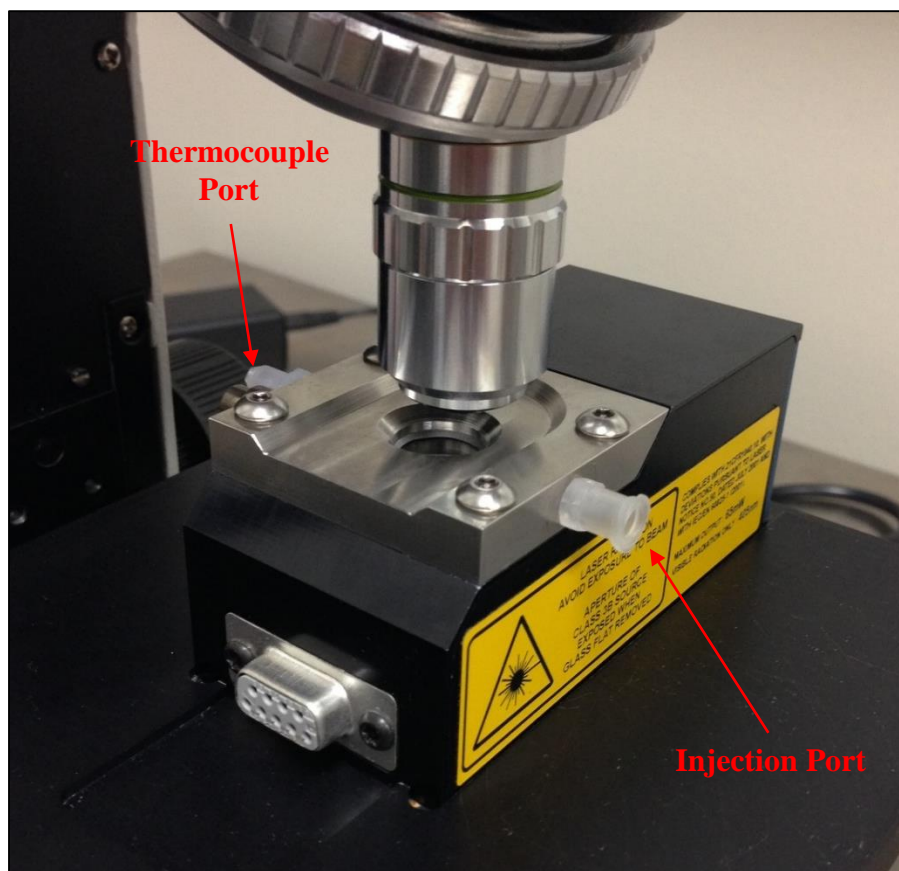


Figure 65. Viewing unit showing the injection and the thermocouple ports

Using the microscope eyepiece, the stage was adjusted until the spot where the laser beam emerges was in view. The view was then diverted from the eyepiece so that the sCMOS camera could be used. In the NTA software, the “Capture” option was selected, which allows for real-time viewing of the illuminated sample without recording any data. Since there is a small variation between the view through the eyepiece and through the camera, any necessary adjustments to the stage were made at this point to find the emerging laser beam. The camera view was then positioned just to the left of the

beam, where particle visibility is the greatest. A drawing showing the area on which the sCMOS camera was focused while using the NanoSight can be seen in Figure 66.

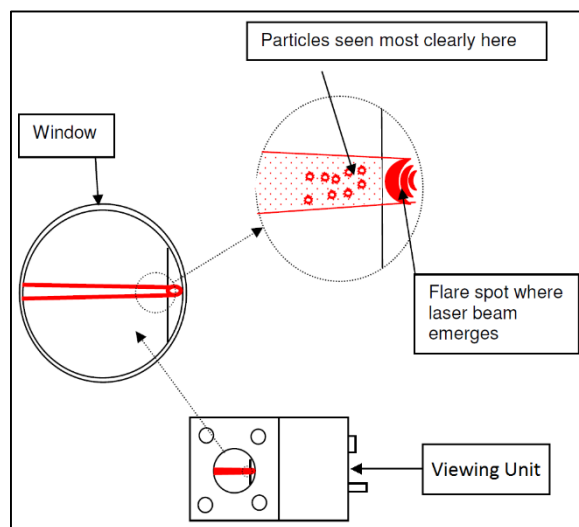


Figure 66. Drawing of NanoSight viewing unit showing the area where the camera was focused [15]

The thermometer was turned on and the calibration temperature for NTA was adjusted to match the reading. At this point, the sample was ready to be analyzed using the NTA software. The “Live” option was selected and the program was run until the number of completed tracks reached 1000. Recording was terminated by clicking the “Live” button again. The laser was shut off, the power supply was disconnected, and the thermocouple was removed from the viewing unit. With the block again being held so that the syringe was pointing upward, the plunger was pulled until the sample area was emptied. Finally, the cleaning procedure discussed at the beginning of this section was repeated to prepare for analysis of the next sample.

5. RESULTS AND ANALYSIS

5.1 Upstream Versus Downstream Particle Size Distributions

For the NanoSight LM10, AMIS-1, and AMIS-2, NEI-prepared Nukon debris and a downstream sample from the vertical-flow sump-strainer loop were both analyzed. The downstream sample that was selected for analysis was the fifth sample bottle (B#5) of the test VWT-04. This sample bottle corresponds to the time period from 50 to 60 minutes after the injection of debris into the system, at about one system turnover. Image of the debris bed at the start and end of sampling for VWT-05 B#5 are included (Figure 67).

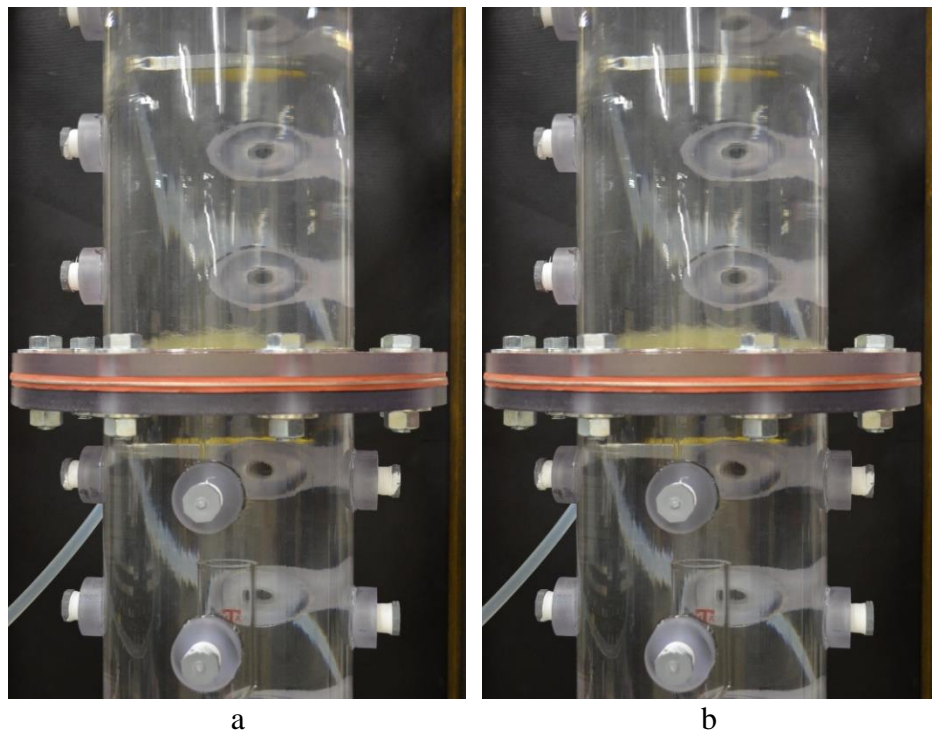


Figure 67. Debris bed at the (a) start and (b) end of sampling for VWT-04 B#5

5.1.1. NanoSight LM10 Results

NEI-prepared Nukon debris and a downstream sample from the vertical-flow sump-strainer loop were both analyzed using the NanoSight LM10. To achieve a statistically accurate distribution, more than 1000 particles were tracked in each sample analysis. Histograms were created for this data between 10-500 nm and were normalized by dividing the number count of particles in each bin by the total number of particles tracked in the sample. The results from the NanoSight LM10 are shown in Table 12 and the plotted histograms are presented in Figure 68 and Figure 69.

Table 12. Results from the NanoSight LM10 for debris size upstream (NEI Nukon debris) and downstream (VWT-04 B#5) of the strainer

Max Bin Value (nm)	Fraction of Number of Particles	
	Nukon Debris	VWT-04 B#5
55	0.26212	0.15531
99	0.28697	0.36664
144	0.18970	0.24148
188	0.11394	0.12615
233	0.06545	0.06094
277	0.03485	0.02490
322	0.02152	0.01212
366	0.01152	0.00655
411	0.00697	0.00295
455	0.00515	0.00164
500	0.00182	0.00131

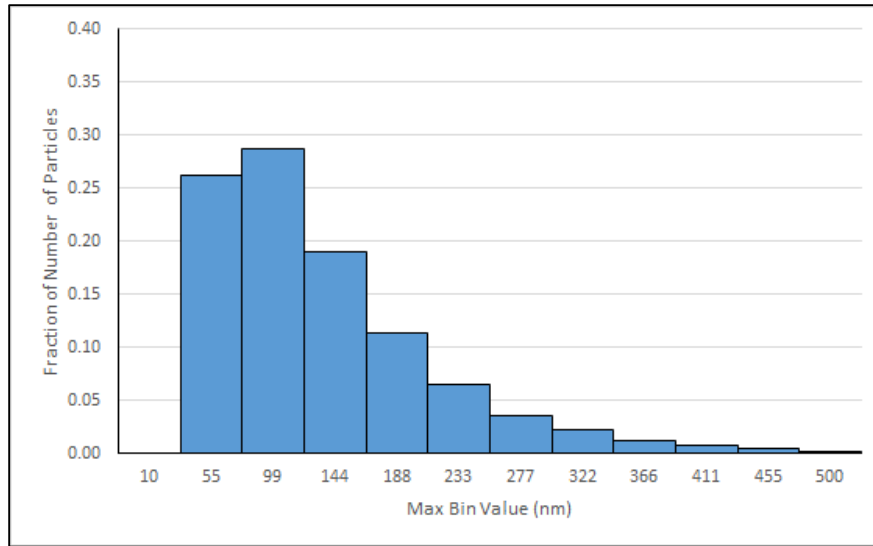


Figure 68. Size distribution of the upstream debris between 10 and 500 nm

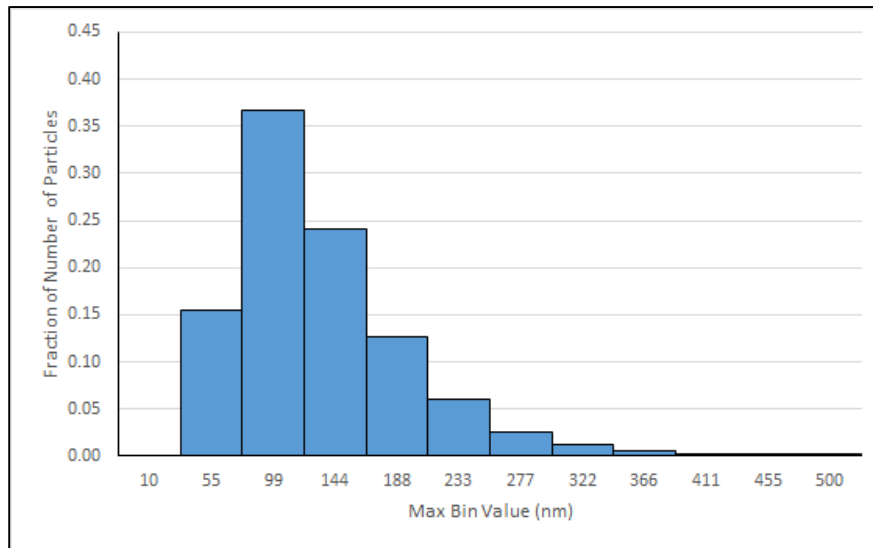


Figure 69. Size distribution of the downstream debris between 10 and 500 nm

From Figure 68 to Figure 69, an increase in the fraction of particles from 55 to 188 nm can be seen. In this range, the fractional number of particles increased by 24%

between the upstream and downstream samples. It is also observed that there is decrease in the fraction of particles in the range 10-55 nm and 188-500 nm, from upstream to downstream of the strainer. This would suggest that the particles in the 55-188 nm range preferentially bypass the fibrous-debris bed and strainer, which is consistent with Hutten's [10] statement that the MPPS is typically in the range of 40-400 nm.

The lower limit for size measurement with the NanoSight LM10 is 10 nm, and the smallest particle measured in the upstream and downstream samples was 17.80 nm. With the minimum particle size being within the range of the measurement equipment, it was expected that bounded PDFs would provide superior fits to those of unbounded functions for this data. PDFs were fit to the data from the NanoSight LM10 using a software called EasyFit. This allowed many distributions to be fit to the data and quickly compared. The three functions selected for the NanoSight LM10 results are shown below in Table 13.

Table 13. PDFs used for fitting the data from the NanoSight LM10

Function	Equation	Parameters	
Johnson's S _B	$f(x) = \frac{\delta}{\lambda z \sqrt{2\pi}(1-z)} e^{\left(-\frac{1}{2}\left(\gamma + \delta \ln\left(\frac{z}{1-z}\right)\right)^2\right)}, \xi \leq x \leq \xi + \lambda$ <p style="text-align: center;">where $z \equiv \frac{x-\xi}{\lambda}$</p>	γ δ λ ξ	shape shape scale location
Lognormal (3P)	$f(x) = \frac{1}{(x-\gamma)\sigma\sqrt{2\pi}} e^{-\frac{1}{2}\left(\frac{\ln(x-\gamma)-\mu}{\sigma}\right)^2}, x > \gamma$	σ μ γ	shape scale location
Weibull (3P)	$f(x) = \frac{\alpha}{\beta} \left(\frac{x-\gamma}{\beta}\right)^{\alpha-1} e^{-\left(\frac{x-\gamma}{\beta}\right)^\alpha}, x > \gamma$	α β γ	shape scale location

To compare the fit of each function to the data, the Kolmogorov-Smirnov (K-S) test was used. This test compares the difference between the empirical cumulative distribution function (ECDF) and a reference cumulative distribution function (CDF) that has been fit to the data. The equation for the ECDF, F_E , is:

$$F_E(x) = \frac{1}{n} \sum_{i=1}^n I(X_i), \quad (6)$$

where X_i is the value of the i^{th} observation and $I(X_i)$ is the indicator function for i^{th} observation which is equal to 1 if $X_i \leq x$ and equal to 0 otherwise. The K-S test statistic for a cumulative distribution function $F(x)$ then is:

$$KS = \sup(|F_n(x) - F(x)|). \quad (7)$$

In the above equation, *sup* is the supremum, or least upper bound, of the differences between the ECDF, $F_E(x)$, and the CDF, $F(x)$. The parameters for each function, along with the values of the K-S test statistic values are presented in Table 14.

Table 14. Results from PDF fitting of the upstream (NEI-prepared Nukon) and downstream (VWT-04, B#5) particle size distributions from NanoSight LM10

Sample	Function	Rank	K-S Test Value	Parameters
NEI- Prepared Nukon	Johnson S_B	1	0.0184	$\gamma = 2.0185$ $\delta = 0.99655$ $\lambda = 632.51$ $\xi = 15.326$
	Lognormal (3P)	2	0.03038	$\sigma = 0.77508$ $\mu = 4.3331$ $\gamma = 10.834$
	Weibull (3P)	3	0.0304	$\alpha = 1.2682$ $\beta = 101.81$ $\gamma = 17.784$
VWT-04 B#5	Johnson S_B	1	0.01505	$\gamma = 3.1491$ $\delta = 1.3667$ $\lambda = 889.2$ $\xi = 14.634$
	Lognormal (3P)	2	0.02193	$\sigma = 0.59204$ $\mu = 4.4683$ $\gamma = 7.6773$
	Weibull (3P)	3	0.02965	$\alpha = 1.4595$ $\beta = 97.199$ $\gamma = 23.497$

As previously stated, it was expected that bounded functions would fit this data best. Of the selected PDFs, the Johnson's S_B distribution, essentially a lognormal distribution truncated on both sides, provided the best fit for both the upstream and downstream data in this range; this is shown by the rankings in Table 14.

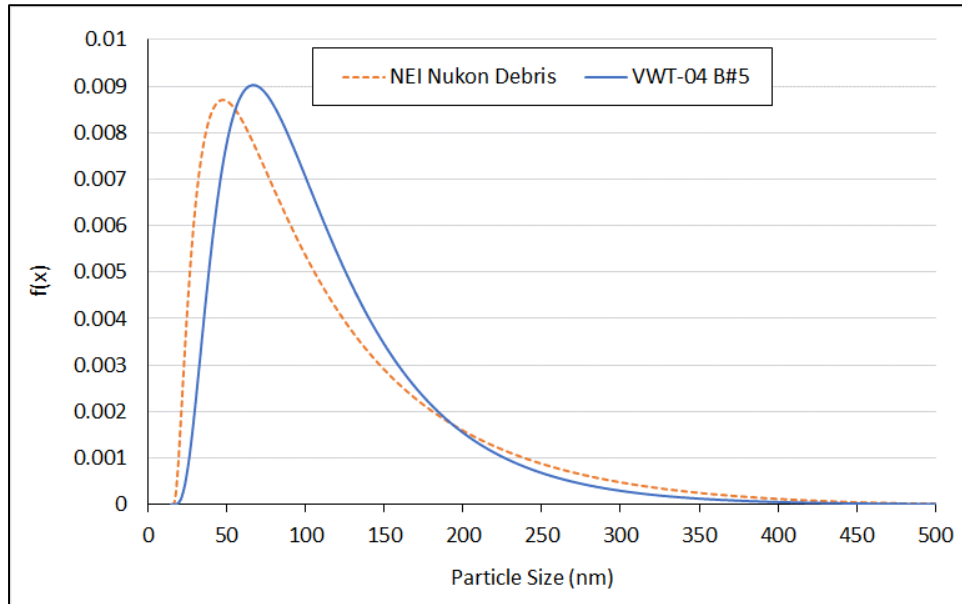


Figure 70. Johnson S_B functions fit to the distributions of the upstream (NEI Nukon debris) and downstream (VWT-04 B#5) particle sizes from the NanoSight LM10

In the above figure, a shift of the peak from a smaller particle size to a large one, upstream to downstream, is consistent with the idea of the MPPS. As particles at the low and high ends of this size range are filtered out by the debris bed, the mode shifts from 47.38 to 66.73 nm upstream to downstream, respectively. The mode was calculated by solving for x in the following equation:

$$\frac{d}{dx}f(x) = 0, \tag{8}$$

where, $f(x)$ is the function for the Johnson's S_B distribution shown in Table 13.

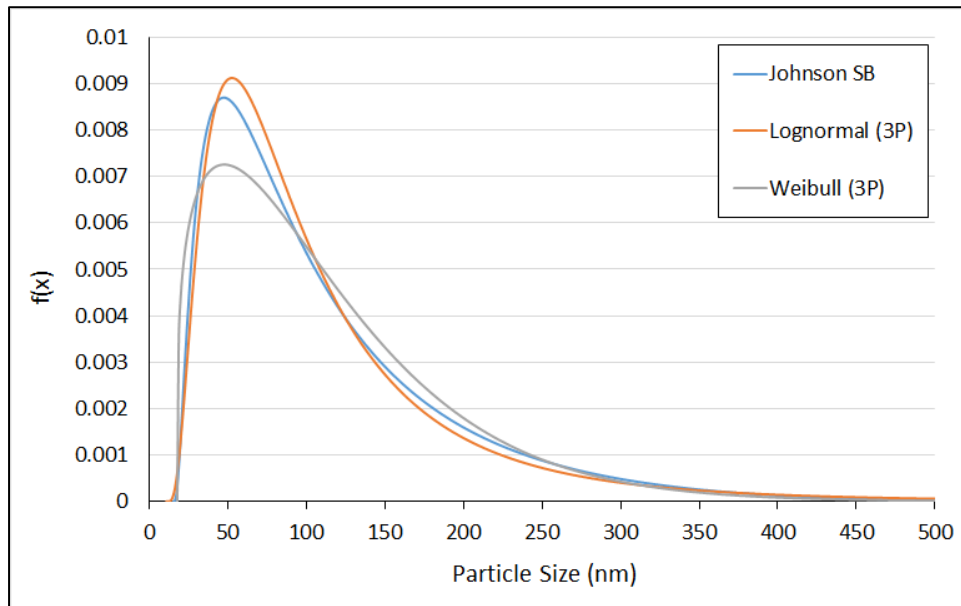


Figure 71. Comparison of the three functions chosen for fitting the particle size distribution of the upstream debris (NEI-prepared Nukon) from the NanoSight LM10

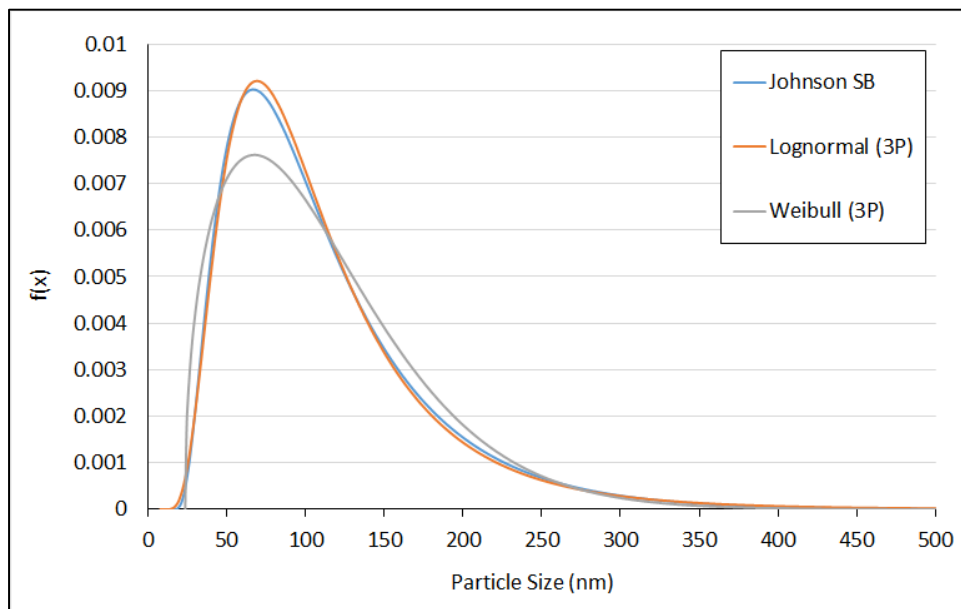


Figure 72. Comparison of the three functions chosen for fitting the particle size distribution of the downstream particles (VWT-04 B#5) from the NanoSight LM10

Any distribution that can be fit with a Johnson's S_B function can also be fit with a lognormal function; however, being that the 3P lognormal function is unbounded on one side, the fit at the upper end of the PSD will deviate. The Johnson's S_B and lognormal distributions for the NanoSight samples were observed to be very similar to one another. This can be seen for both the upstream and downstream PSDs in Figure 71 and Figure 72, respectively. The Weibull distributions in both Figure 71 and Figure 72 is observed to deviate from the other two distributions, and has the highest K-S test value for both the upstream and downstream PSDs.

5.1.2. AMIS-1 Results

Images taken using AMIS-1 were processed and the particles were measured using a known pixel-to-length ratio. An example image from AMIS-1 before and after processing is presented in Figure 73.

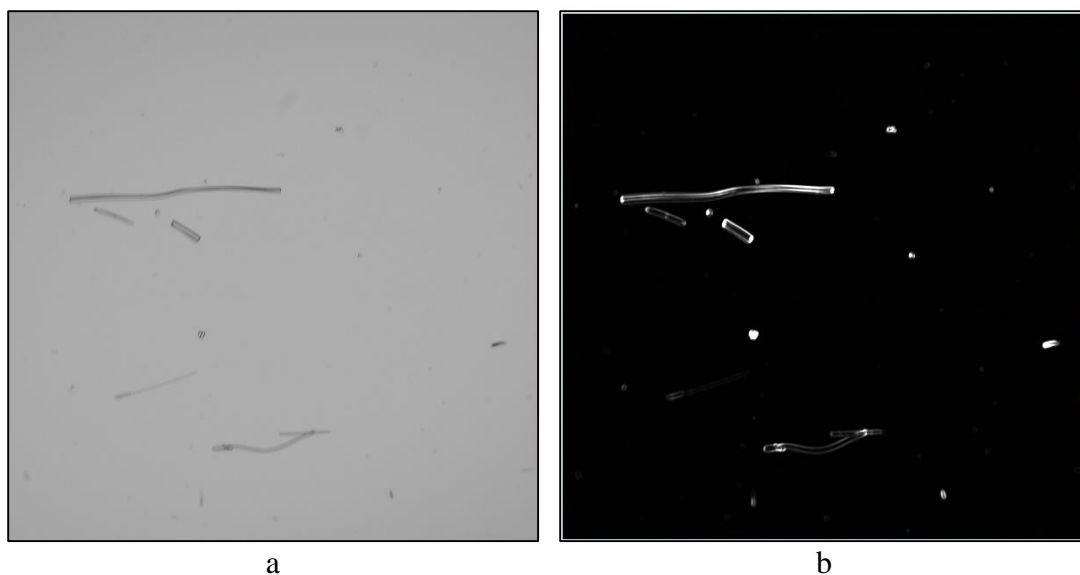


Figure 73. Image taken with AMIS-1 (a) before and (b) after processing, reprinted with permission from [16], Copyright 2014 by the American Chemical Society, La Grange Park, Illinois.

For each particle, the feret length, or maximum caliper diameter, was recorded. This dimension is the distance between the two most separated points on the outline of the particle [17]. An example is presented in Figure 74; the outline of the particle is in red, and the feret length is in green.

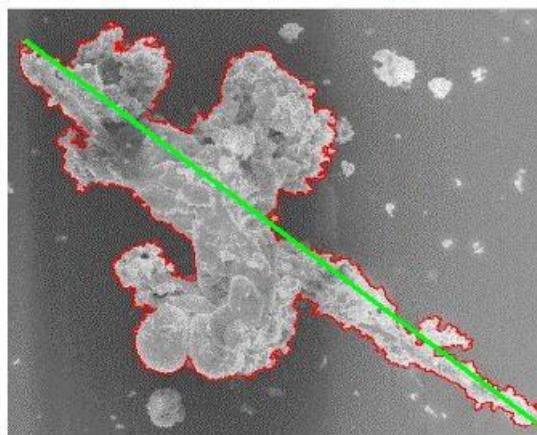


Figure 74. Feret length of a particle (represented by the green line) [17]

To reduce the number of images required for analyzing the downstream debris, the samples being used were concentrated. The downstream sample was placed in a graduated cylinder, where it was allowed to settle for at least two hours. Once the debris had settled, water was extracted from the top of the cylinder using a syringe. The final concentration of the downstream sample was 150X. The results from AMIS-1 are presented in Table 15. Plots of these results upstream and downstream of the strainer are shown in Figure 75 and Figure 76, respectively. These histograms were normalized by dividing the number count of particles in each bin by the total number of particles measured.

Table 15. Results from AMIS-1 for debris size upstream (NEI Nukon debris) and downstream (VWT-04 B#5) of the strainer

Max Bin Value (μm)	Fraction of Number of Particles	
	Upstream (NEI-Prepared Nukon Debris)	Downstream (VWT-04 B#5)
55	0.76951	0.89268
99	0.08340	0.04876
144	0.04902	0.02018
188	0.02952	0.01191
233	0.01435	0.00818
277	0.01665	0.00493
322	0.00621	0.00736
366	0.00911	0
411	0.00926	0.00099
455	0.00660	0.00304
500	0.00635	0.00197

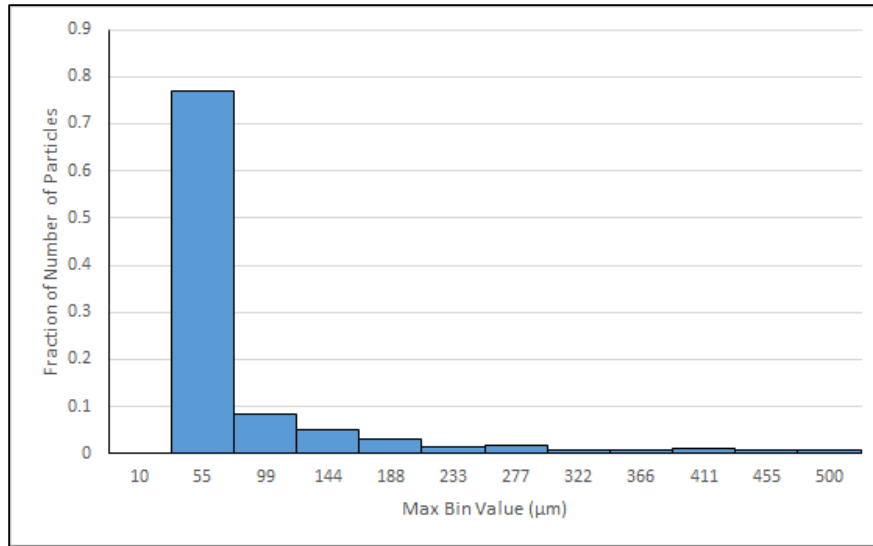


Figure 75. Size distribution of the upstream debris from AMIS-1

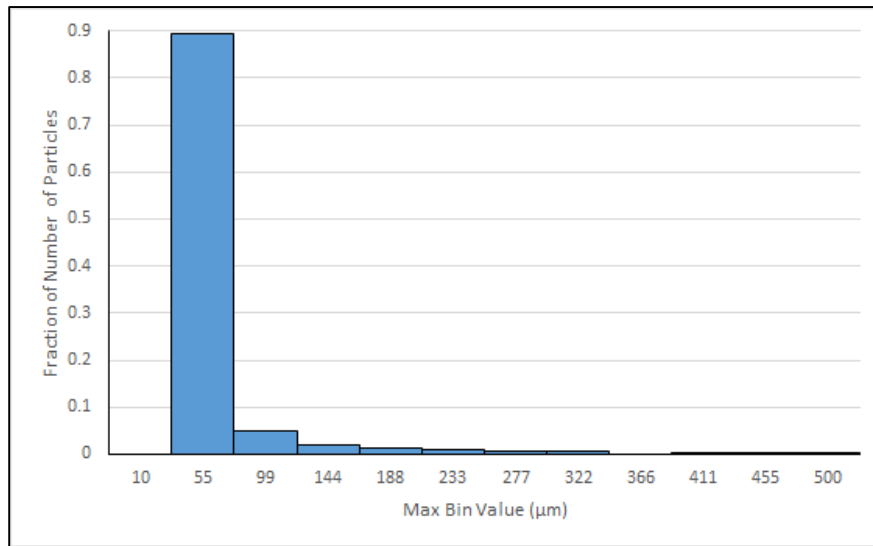


Figure 76. Size distribution of the downstream debris from AMIS-1

In the size range from 10-500 µm, larger particles were preferentially filtered from the upstream water. This is evident from the shift of the particle size distribution to

the left between figures Figure 75 and Figure 76. The fraction of particles in the first bin, with a range of 10-55 μm , increased from approximately 77 % in the upstream sample to 89 % in the downstream sample, while the fractional particle number of nearly every other bin decreased from upstream to downstream. This trend of larger particles being more efficiently filtered than smaller ones was expected based on statements from Sutherland and Purchas [11] and the graph in Figure 4.

The Johnson's S_B distribution didn't provide an appropriate fit of the particle distributions for AMIS-1 or AMIS-2, so the log-logistic function was chosen to be used as a third fitting function. The three functions selected for fitting to the AMIS-1 results are shown in Table 16, below. The parameters for each function, along with the values of the K-S test statistic, for both the upstream and downstream samples are presented in Table 17.

Table 16. PDFs used for fitting the results from AMIS-1

Function	Equation	Parameters	
Log-logistic (3P)	$f(x) = \frac{\alpha}{\beta} \left(\frac{x-\gamma}{\beta}\right)^{\alpha-1} \left(1 + \left(\frac{x-\gamma}{\beta}\right)^\alpha\right)^{-2}, x > \gamma$	α β γ	shape scale location
Lognormal (3P)	$f(x) = \frac{1}{(x-\gamma)\sigma\sqrt{2\pi}} e^{-\frac{1}{2}\left(\frac{\ln(x-\gamma)-\mu}{\sigma}\right)^2}, x > \gamma$	σ μ γ	shape scale location
Weibull (3P)	$f(x) = \frac{\alpha}{\beta} \left(\frac{x-\gamma}{\beta}\right)^{\alpha-1} e^{-\left(\frac{x-\gamma}{\beta}\right)^\alpha}, x > \gamma$	α β γ	shape scale location

Table 17. Results from PDF fitting of the upstream (NEI-prepared Nukon) and downstream (VWT-04, B#5) particle size distributions from AMIS-1

Sample	Function	Rank	K-S statistic value	Parameters
NEI- Prepared Nukon	Log-logistic (3P)	2	0.03663	$\alpha = 0.8992$ $\beta = 10.483$ $\gamma = 10$
	Lognormal (3P)	1	0.0323	$\sigma = 1.7548$ $\mu = 2.3454$ $\gamma = 9.8849$
	Weibull (3P)	3	0.1096	$\alpha = 0.59565$ $\beta = 26.762$ $\gamma = 10$
VWT-04 B#5	Log-logistic (3P)	1	0.0298	$\alpha = 1.0497$ $\beta = 6.4421$ $\gamma = 10.117$
	Lognormal (3P)	2	0.03937	$\sigma = 1.572$ $\mu = 1.8709$ $\gamma = 9.9984$
	Weibull (3P)	3	0.11403	$\alpha = 0.55524$ $\beta = 11.13$ $\gamma = 10.12$

For the upstream particles, the lognormal distribution provided the best fit, while the log-logistic function fit the downstream data best. The distributions obtained from fitting the log-logistic function to the particle size data were very similar to those produced from the lognormal function; this will be shown in later figures. It was decided to present the lognormal functions for the upstream and downstream PSDs in Figure 77, since the lognormal function is commonly used for fitting particle system data [8].

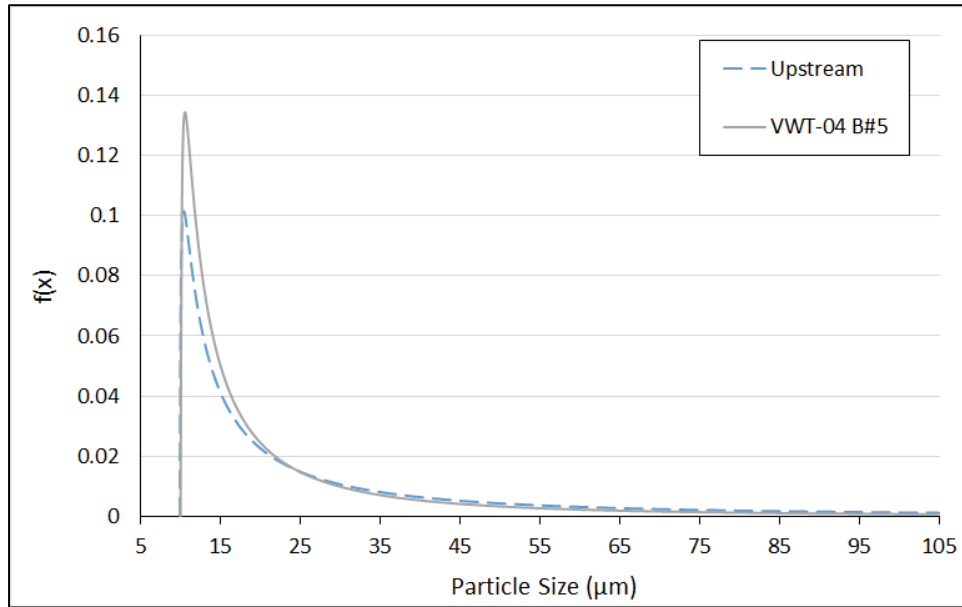


Figure 77. Lognormal function fit to the distributions of the upstream (NEI Nukon debris) and downstream (VWT-04 B#5) particle sizes from AMIS-1

The mean particle sizes in the upstream and downstream distributions in Figure 77 are 58.55 µm and 32.34 µm, respectively. This change in the mean particle size between the two distributions demonstrates that the particles of smaller size preferentially bypass the debris bed and strainer. The mean particle size *MPS* was calculated using the following equation:

$$MPS = \int_{L.L.}^{U.L.} f(x) x dx, \quad (9)$$

where *U.L.* is the upper limit, *L.L.* is the lower limit, and *f(x)* is the function for the lognormal distribution (Table 16). For the lognormal function, *U.L.* = ∞ and *L.L.* = γ.

A comparison of the three functions used in fitting the data from AMIS-1 is shown below. Figure 78 presents the functions for the upstream sample and Figure 79 presents the functions for the downstream sample.

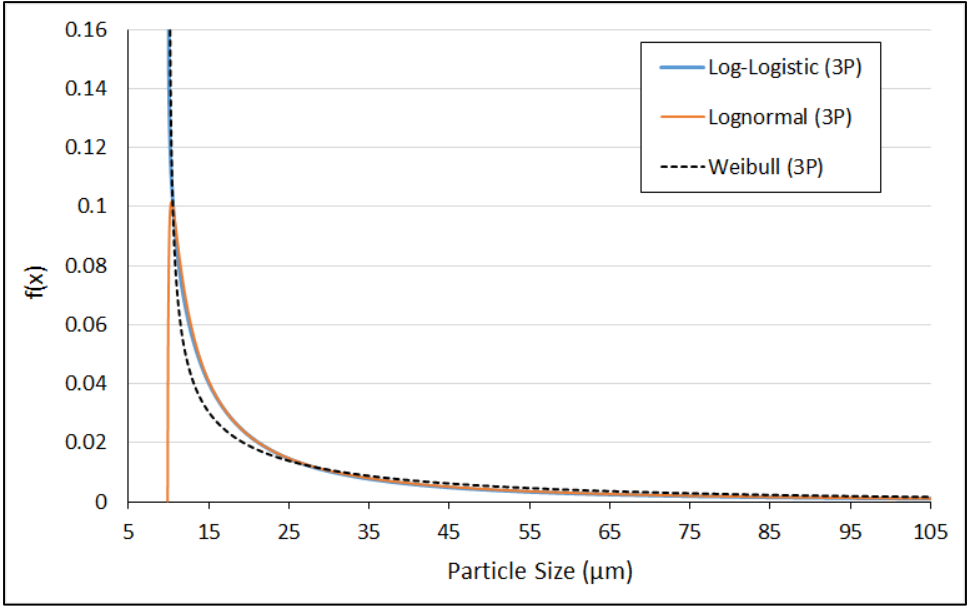


Figure 78. Comparison of the three functions chosen for fitting the particle size distribution of the upstream debris (NEI-prepared Nukon) from AMIS-1

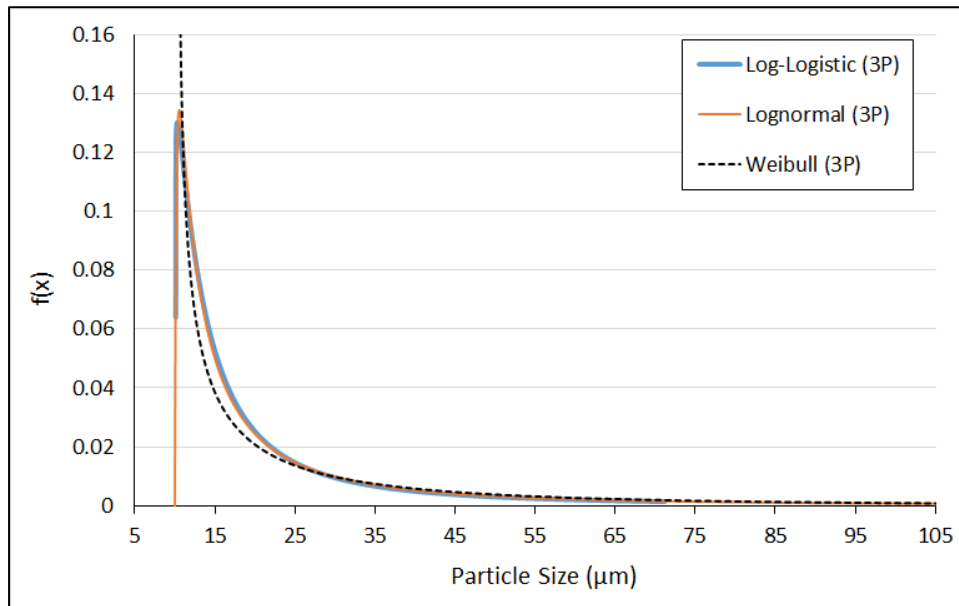


Figure 79. Comparison of the three functions chosen for fitting the particle size distribution of the downstream debris (VWT-04 B#5) from AMIS-1

For the upstream particles down to 10 μm (the lower limit of AMIS-1) the log-logistic and lognormal distributions are essentially overlapping, as shown in Figure 78. The same observation is made for the downstream particle size distributions in Figure 79. As with the nanometer range, the Weibull distributions for particles in the range of 10-500 μm deviates from the other two distributions (Figure 78 and Figure 79), and has the highest K-S test value for both the upstream and downstream PSDs (Table 17).

5.1.3. AMIS-2 Results

As with AMIS-1, images taken using AMIS-2 were processed and the feret length of each particle was measured using a known pixel-to-length ratio. An example image from AMIS-2 before and after processing is presented in Figure 80.

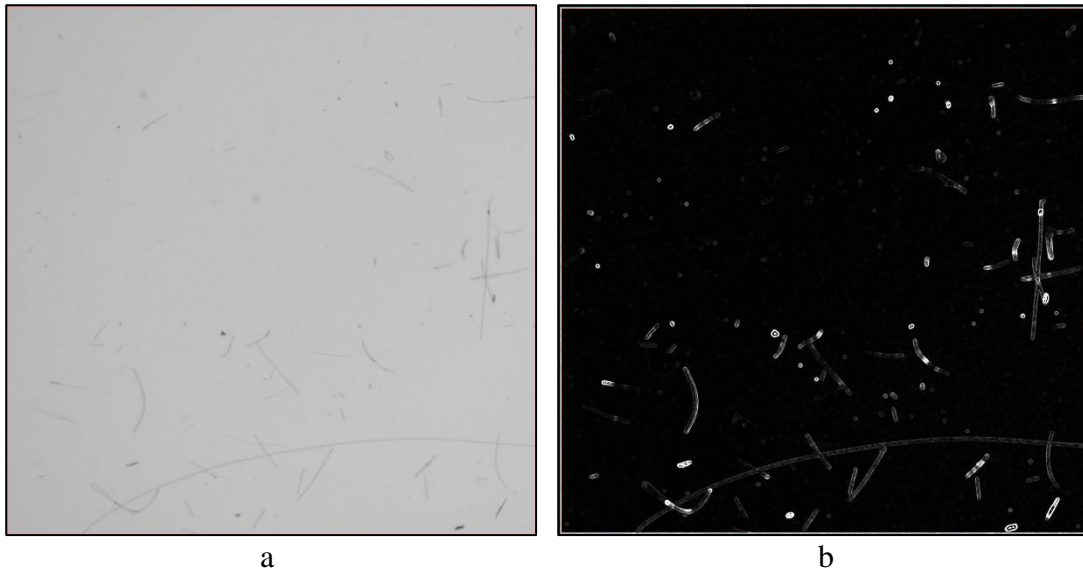


Figure 80. Image taken with AMIS-2 (a) before and (b) after processing

The samples analyzed using this system were concentrated in the same way as those used in AMIS-1. The results from AMIS-2 are shown in Table 18, below. Plots of these results upstream and downstream of the strainer are shown in Figure 81 and Figure 82, respectively. These histograms were normalized by dividing the number count of particles in each bin by the total number of particles measured.

Table 18. Results from AMIS-2 for debris size upstream (NEI Nukon debris) and downstream (VWT-04 B#5) of the strainer

Max Bin Value (μm)	Fraction of Number of Particles	
	Upstream (NEI-Prepared Nukon Debris)	Downstream (VWT-04 B#5)
340	0.53622	0.66797
580	0.22099	0.18750
820	0.09139	0.06641
1060	0.05271	0.02930
1300	0.03578	0.01953
1540	0.02503	0.01563
1780	0.01294	0.00586
2020	0.01201	0.00391
2260	0.00564	0.00391
2500	0.00728	0

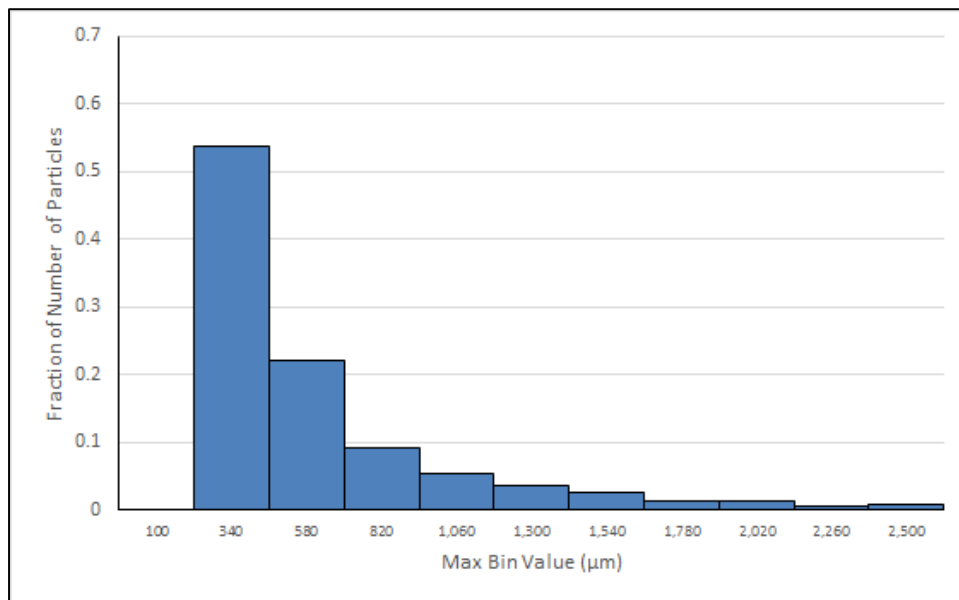


Figure 81. Size distribution of the upstream debris from AMIS-2

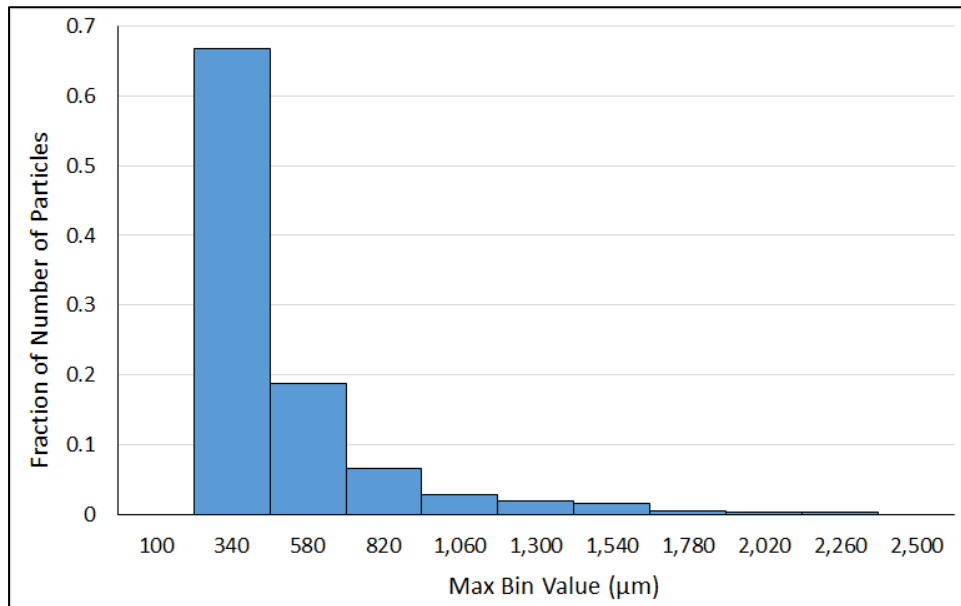


Figure 82. Size distribution of the downstream debris from AMIS-2

The results in the size range from 100-2500 µm (from AMIS-2) were similar to those in the range from 10-500 µm (AMIS-1), with larger particles being more effectively filtered from the upstream water. This is demonstrated in figures Figure 81 and Figure 82. In the size range of 100-340 µm, the fraction of particles changes from 0.536 to 0.668 from upstream to downstream, respectively, while every other size range in the histograms decreases from Figure 81 to Figure 82.

The three functions selected for the AMIS-2 results were the same three used for AMIS-1, and are shown in Table 16. The parameters and K-S test statistic value for each function for both the upstream and downstream samples are presented in Table 19.

Table 19. Results from PDF fitting of the upstream (NEI-prepared Nukon) and downstream (VWT-04, B#5) particle size distributions from AMIS-2

Sample	Function	Rank	K-S statistic value	Parameters
NEI- Prepared Nukon	Log-logistic (3P)	2	0.03479	$\alpha = 1.3331$ $\beta = 190.5$ $\gamma = 99.322$
	Lognormal (3P)	3	0.03821	$\sigma = 1.194$ $\mu = 5.2704$ $\gamma = 92.221$
	Weibull (3P)	1	0.02842	$\alpha = 0.88858$ $\beta = 327.02$ $\gamma = 100.51$
VWT-04 B#5	Log-logistic (3P)	3	0.08755	$\alpha = 0.87836$ $\beta = 111.54$ $\gamma = 100$
	Lognormal (3P)	2	0.07339	$\sigma = 1.7727$ $\mu = 4.4379$ $\gamma = 98.343$
	Weibull (3P)	1	0.05597	$\alpha = 0.65244$ $\beta = 205.34$ $\gamma = 100$

The Weibull function was found to most closely fit the particle size data for both the upstream and downstream samples analyzed with AMIS-2, as the rankings in Table 19 show. Figure 83 presents the Weibull functions for both of the samples.

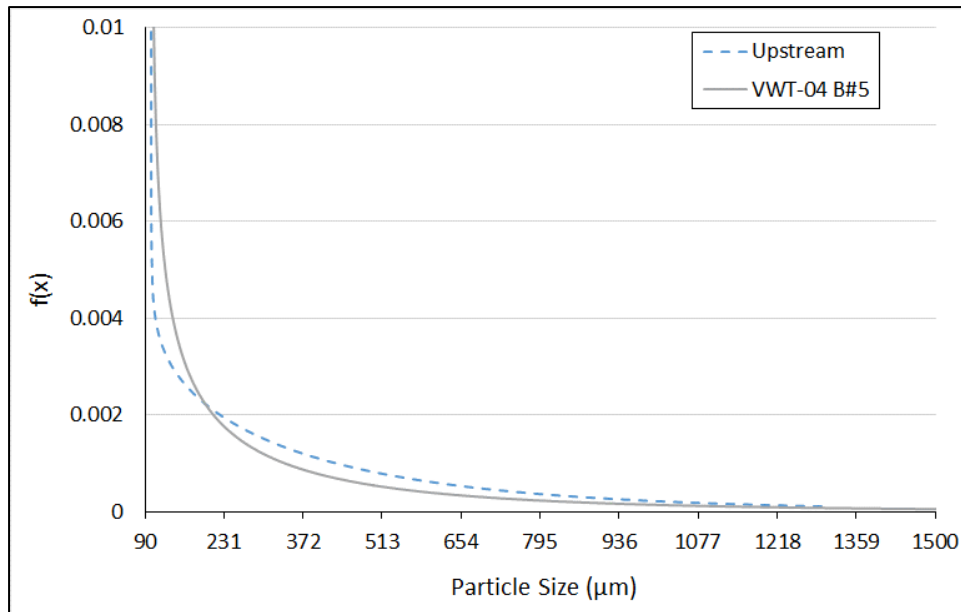


Figure 83. Weibull function fit to the distributions of the upstream (NEI Nukon debris) and downstream (VWT-04 B#5) particle sizes from AMIS-2

As with the results from AMIS-1, the average particle size of the fitted distributions shifts to a lower value when comparing the upstream sample to the downstream. The mean particle sizes in the upstream and downstream distributions in Figure 83 are 447 μm and 379 μm , respectively. This change in the mean particle size between the two distributions shows that, in the size range of 100-2500 μm , the particles of smaller size preferentially bypass the debris bed and strainer. The mean particle size *MPS* was calculated using Eq. 9. The Weibull distribution function (Table 16) was used for $f(x)$, and $U.L. = \infty$ and $L.L. = \gamma$ were the integration limits.

Comparisons of the three functions used in fitting the data from AMIS-2 are shown below. Figure 84 presents the functions for the upstream sample and Figure 85 presents the functions for the downstream sample.

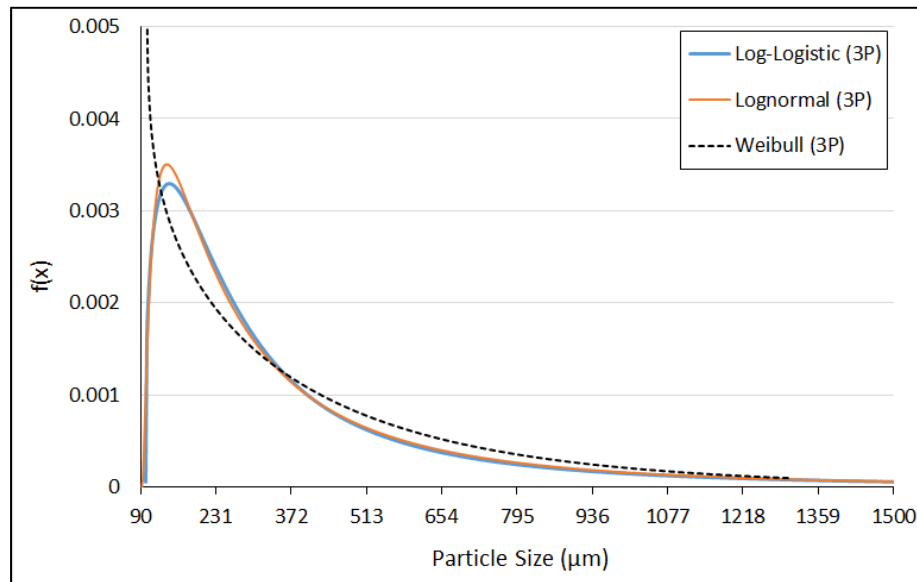


Figure 84. Comparison of the three functions chosen for fitting the particle size distribution of the upstream debris (NEI-prepared Nukon) from AMIS-2

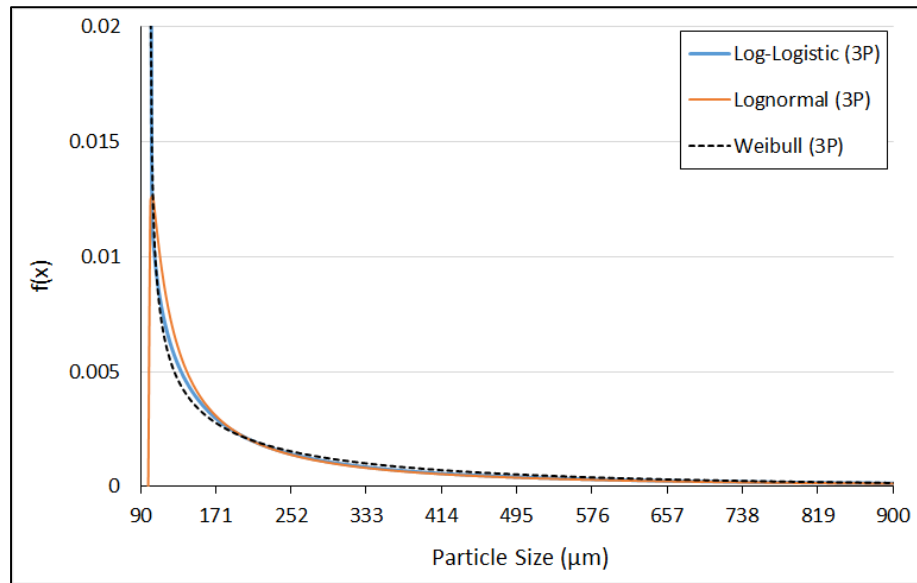


Figure 85. Comparison of the three functions chosen for fitting the particle size distribution of the downstream debris (VWT-04 B#5) from AMIS-2

5.2 Coulter Counter Results for Non-Fibrous Debris

As previously mentioned, the Coulter Counter did not work well for the fibrous debris; however, it was used for the analysis of other debris types during the course of this research. The two debris samples that were analyzed with this instrument were silicon carbide (SiC) powder and tin particles. To give a qualitative comparison of the differences between these two types of debris, images of the SiC powder and tin particles were taken with a scanning electron microscope (SEM). Images of a sample from the SiC powder taken at 250x (Figure 86) and 1,000x (Figure 87) magnifications are shown below.

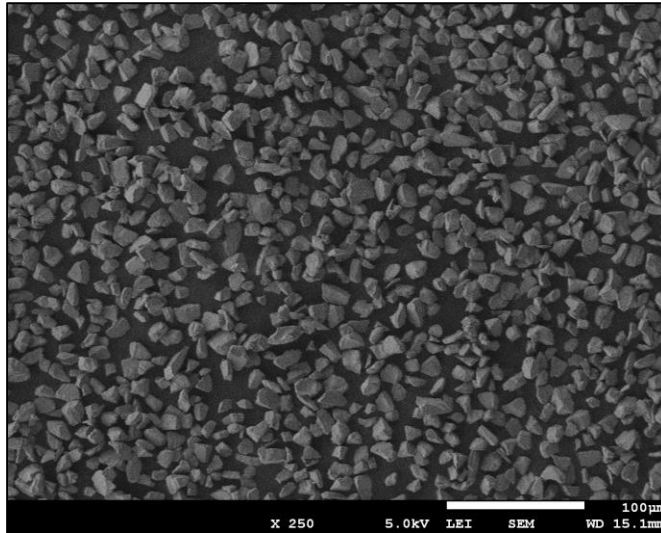


Figure 86. SEM image of SiC F600 powder at 250x magnification

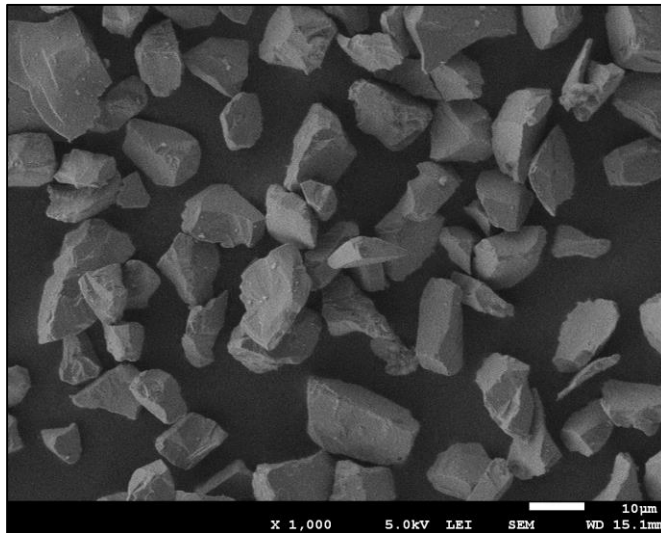


Figure 87. SEM image of SiC F600 powder at 1,000x magnification

The particles of SiC powder (Figure 86 and Figure 87) could be classified as angular or quadrangular, as defined by NIST [18]. Definitions of these two particle morphology classifications are given below, with example images included.

- Angular: sharp edges, prominent, slightly rounded or straight.



Figure 88. Example of an angular particle from NIST morphology glossary [18]

- Quadrangular: outline has four prominent sides or two parallel sides, most sides are straight, almost right angled.



Figure 89. Example of a quadrangular particle from NIST morphology glossary [18]

As can be seen in Figure 73 and Figure 80, the fibrous debris typically has a length much greater than its diameter. For this reason, the orientation of the debris as it approaches the aperture is important, and depending on the orientation, the particle may

or may not pass through the aperture. Unlike the fibrous particles, the particles of SiC powder (Figure 86 and Figure 87) look roughly prismatic and don't seem to have one dimension that is much larger than another, which reduces the role that the particle's orientation plays in determining whether it passes through the aperture. The results for the SiC powder obtained using the Coulter Counter with a 100- μm diameter aperture, are presented in Table 20. The measuring range of this aperture is 2-60 μm .

Table 20. Results for SiC powder from the Coulter Counter using a 100- μm aperture

Particle Diameter (μm)	Fraction of Number of Particles	Particle Diameter (μm)	Fraction of Number of Particles	Particle Diameter (μm)	Fraction of Number of Particles
2.11	0.00378	6.79	0.05276	20.73	0.00033
2.22	0.00445	7.16	0.05810	21.86	0.00033
2.35	0.00367	7.55	0.06066	23.05	0
2.47	0.00668	7.96	0.07046	24.31	0
2.61	0.00434	8.40	0.07179	25.64	0
2.75	0.00390	8.86	0.07569	27.04	0
2.90	0.00501	9.34	0.06890	28.51	0.00011
3.06	0.00401	9.85	0.06690	30.07	0
3.23	0.00467	10.39	0.05955	31.71	0
3.40	0.00545	10.95	0.05065	33.44	0
3.59	0.00568	11.55	0.04085	35.27	0
3.78	0.00490	12.18	0.03083	37.19	0
3.99	0.00612	12.85	0.02093	39.22	0
4.21	0.00701	13.55	0.01269	41.36	0
4.44	0.00913	14.29	0.00623	43.62	0
4.68	0.01035	15.07	0.00345	46.00	0
4.94	0.01258	15.89	0.00111	48.51	0
5.21	0.01492	16.76	0.00122	51.16	0
5.49	0.02204	17.67	0.00067	53.95	0
5.79	0.02683	18.64	0.00022	56.89	0
6.11	0.03762	19.65	0.00022	60.00	0
6.44	0.04219				

Figure 90 contains a plot of the data from Table 20. Although the table includes the entire measuring range of the aperture used, this data is only plotted up to 28.51 μm , as the bins of larger particle diameter are empty.

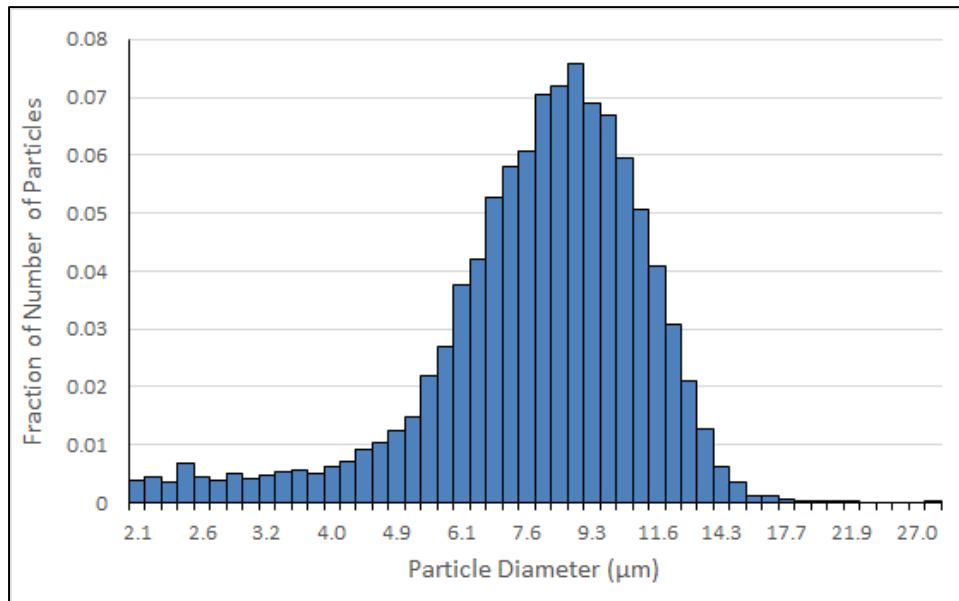


Figure 90. Size distribution of F600 SiC from Coulter Counter (100- μm aperture)

The coulter counter was also used to analyze tin particles. Images of a sample from the tin particles taken at 1,000x (Figure 91) and 10,000x (Figure 92) magnifications are shown below.

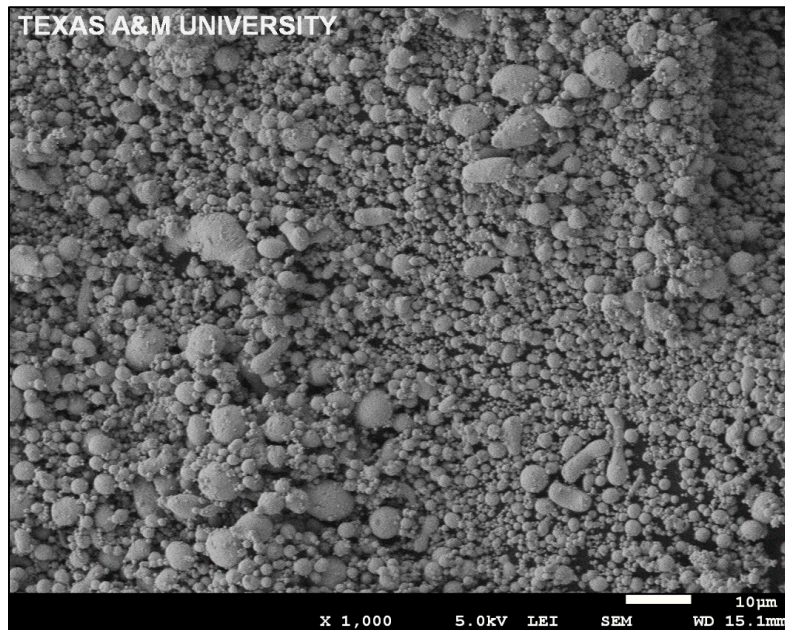


Figure 91. SEM image of tin particles at 1,000x magnification

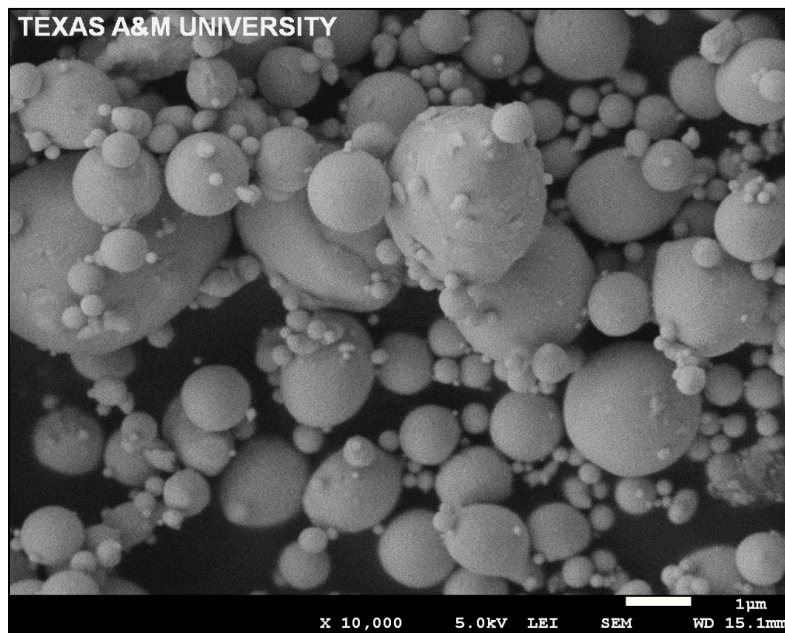


Figure 92. SEM image of tin particles at 10,000x magnification

Some of the tin particles (Figure 91 and Figure 92) can be classified as sphere while others can be classified as sub-sphere in shape, as defined by NIST [18]. Definitions of these two particle morphology classifications, along with example images, can be seen below.

- Sphere: round, spherical overall shape

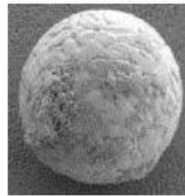


Figure 93. Example of a spherical particle from NIST morphology glossary [18]

- Sub-sphere: roughly spherical



Figure 94. Example of a sub-sphere particle from NIST morphology glossary [18]

For spherical particles, the orientation of the particle as it approaches the aperture is of no consequence. For this reason, there were no issues with the analysis of these

particles using the Coulter Counter. The results for the tin particles, obtained using the Coulter Counter with a 30- μm diameter aperture, are presented in Table 21. The measuring range of this aperture is 0.60-18 μm .

Table 21. Results for tin particles from the Coulter Counter using a 30- μm aperture

Particle Diameter (μm)	Fraction of Number of Particles	Particle Diameter (μm)	Fraction of Number of Particles	Particle Diameter (μm)	Fraction of Number of Particles
0.60	0	1.93	0.02602	5.90	0
0.63	0.02554	2.04	0.02460	6.22	0
0.67	0.03974	2.15	0.02460	6.56	0
0.70	0.03784	2.27	0.02034	6.92	0
0.74	0.04115	2.39	0.02176	7.29	0.00047
0.78	0.03548	2.52	0.01703	7.69	0
0.83	0.03548	2.66	0.01277	8.11	0
0.87	0.03832	2.80	0.01561	8.55	0
0.92	0.03737	2.95	0.00804	9.02	0
0.97	0.04021	3.12	0.00804	9.51	0
1.02	0.04021	3.29	0.00662	10.03	0
1.08	0.04399	3.47	0.00331	10.58	0
1.14	0.04163	3.65	0.00615	11.16	0
1.20	0.04541	3.85	0.00237	11.77	0
1.26	0.04163	4.06	0.00189	12.41	0
1.33	0.04541	4.29	0.00237	13.09	0
1.40	0.03737	4.52	0.00284	13.80	0
1.48	0.03926	4.77	0.00047	14.55	0
1.56	0.03690	5.03	0	15.35	0
1.65	0.02886	5.30	0.00047	16.19	0
1.74	0.03075	5.59	0.00047	17.07	0
1.83	0.03122				

A histogram of the data from Table 21 is shown in Figure 95. Although Table 21 includes the entire measuring range of the aperture used, this data is only plotted up to 7.29 μm , as the bins of larger particle diameter are empty.

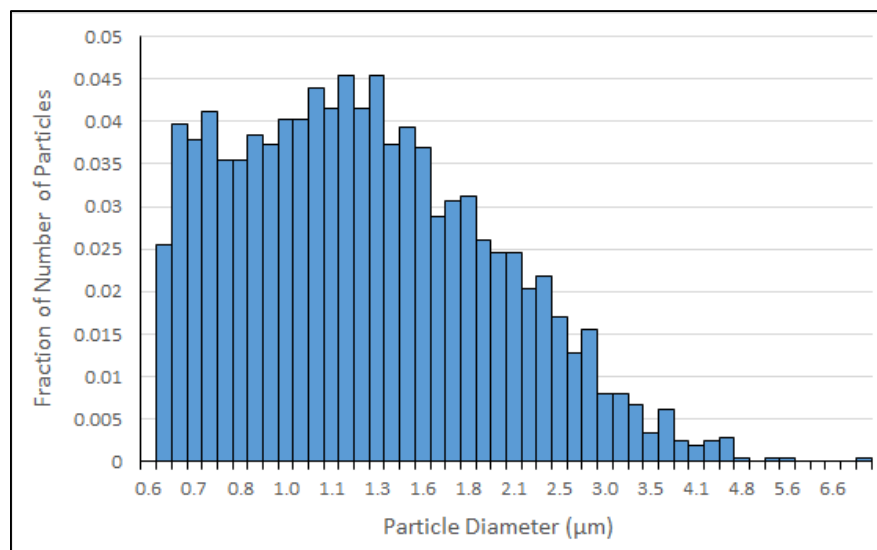


Figure 95. Size distribution of tin particles from Coulter Counter (30- μm aperture)

6. CONCLUSION

The objective of this particular research was to create a methodology for obtaining PSDs for fibrous-thermal-insulation debris both upstream and downstream of a containment sump strainer in multiple size ranges. The NEI protocol was used to simulate debris created during a LOCA. This debris was then injected into an experimental facility which simulated the conditions in a LWR containment sump. Samples were taken downstream of the strainer during the experiment. Using a NanoSight LM10 and two optical microscope systems, size measurements of the particles in upstream and downstream samples were made. Finally, these size measurements were used to create PSDs. PDFs were also fit to the data from the analysis of these samples.

PSDs of fibrous debris upstream and downstream of the strainer with a fibrous debris bed on it were obtained using three different facilities: a NanoSight LM10 and two optical microscope systems (AMIS-1 and AMIS-2). The size-measurement ranges of these facilities are 10-500 nm, 10-500 μm , and 100-2500 μm for the NanoSight LM10, AMIS-1, and AMIS-2, respectively. In the nanometer range, the effect of relative inefficiencies in the diffusion and inertial mechanisms of particle capture were observed in the changes between the PSDs upstream and downstream of the strainer. When comparing the histograms (Figure 68 and Figure 69), the fractional number of particles in the range of 55-188 nm increased from 0.591 to 0.734 from upstream to downstream, while all other bins of smaller and larger particle sizes decreased. This trend is consistent

with Hutten's [10] statement that the MPPS is typically in the range of 40-400 nm. For both AMIS-1 and AMIS-2 the larger-size particles were preferentially filtered out of the water by the debris bed. For AMIS-1, from upstream to downstream, the fraction of particles smaller than 55 μm increased from 0.77 to 0.89 (Table 15). The fractions of particles in almost all of the larger bins decreased, demonstrating that the larger particles were more efficiently filtered by the debris bed. For AMIS-2, from upstream to downstream, the fraction of particles smaller than 340 μm increased from 0.536 to 0.668 (Table 18). The fractions of particles in all of the larger bins decreased, also demonstrating that the larger particles were more efficiently filtered by the debris bed.

It was found that different functions provided the fit for the PSDs in each of the three size ranges measured. For the nanometer range, three PDFs were used to fit the data: Johnson's S_B , lognormal (3P), and Weibull (3P). It was expected that the Johnson's S_B function, being bounded on both sides, would give the best fit of the three selected functions. This was the case, as the K-S test value for the Johnson's S_B distribution was the lowest for both the upstream and downstream PSDs. For the 10-500 μm range, the Johnson's S_B distribution didn't fit the data well, and instead the log-logistic function was used along with the lognormal and Weibull distributions. This was expected due to the PSDs in this size range being unbounded by the measurement range of AMIS-1. Although the log-logistic function fit the downstream data better, the lognormal function provided a better fit for the upstream data, and due to the frequent application of the lognormal function for PSDs, it was selected for use in this size range. The mean particle sizes in the upstream and downstream distributions in Figure 77 are 58.55 μm and 32.34

μm , respectively. This change in the mean particle size between the two distributions demonstrates that the particles of smaller size preferentially bypass the debris bed and strainer. The data from AMIS-2 (100-2500 μm size range) was fit using the same three functions that were used for AMIS-1. For both the upstream and downstream data, the Weibull distribution was found to fit best. The mean particle sizes in the upstream and downstream distributions in Figure 83 are 477 μm and 379 μm , respectively. This decrease in the mean particle size between the two distributions demonstrates that the particles of smaller size preferentially bypass the debris bed and strainer.

Size distributions for spherical (tin powder) and angular (SiC F600) particles were easily obtained using the Coulter Counter, however, it is not recommended that it be used to obtain size distributions for fibrous debris. The Coulter Counter didn't provide reliable results for this debris type, due to the buildup of fibers on the aperture while running the machine.

REFERENCES

- [1] "Pressurized Water Reactor Sump Performance Evaluation Methodology." Nuclear Energy Institute (2004).
- [2] "Description of the Safety Concern." U.S. Nuclear Regulatory Commission, Washington D.C. (2013). <http://www.nrc.gov/reactors/operating/ops-experience/pwr-sump-performance/safety-concern.html>.
- [3] "Function of the Containment Sump." U.S. Nuclear Regulatory Commission, Washington D.C. (2013). <http://www.nrc.gov/reactors/operating/ops-experience/pwr-sump-performance/function-containment-sump.html>.
- [4] A.W. Serkiz. NUREG-0897 "Containment Emergency Sump Performance." U.S. Nuclear Regulatory Commission, Washington D.C. (1985).
- [5] R.W. Borchardt. SECY-10-0113 "Closure Options for Generic Safety Issue-191, Assessment of Debris Accumulation on Pressurized Water Reactor Sump Performance." U.S. Nuclear Regulatory Commission, Washington D.C. (2010).
- [6] R. Vaghetto, Y.A. Hassan. "Study of debris-generated core blockage scenarios during loss of coolant accidents using RELAP5-3D." Nuclear Engineering and Design, Vol. 261, Pgs. 144-155 (2013).
- [7] H.G. Merkus. "Particle Size Measurements." Springer (2009).
- [8] T. Allen. "Powder Sampling and Particle Size Determination." Elsevier (2003).
- [9] G. Zigler, J. Brideau, D. V. Rao, C. Shaffer, E. Souto, W. Thomas. NUREG/CR-6224 "Parametric Study of the Potential for BWR ECCS Strainer Blockage Due to

LOCA-Generated Debris.” U.S. Nuclear Regulatory Commission, Washington D.C. (1995).

[10] I. Hutten. “Handbook on Non-Woven Filter Media.” Elsevier (2007).

[11] K. Sutherland, D.B. Purchas. “Handbook of Filter Media.” Elsevier (2002).

[12] “ZOI Fibrous Debris Preparation: Processing, Storage and Handling.” Rev. 1. Nuclear Energy Institute, Washington, D.C. (2012).

[13] “Multisizer™ 3 COULTER COUNTER®.” Beckman Coulter, Inc.

<https://www.beckmancoulter.com/wsrportal/WSR/industrial/products/coulter-counter-analyzers/index.htm>.

[14] “Multisizer™ 3 Operator’s Manual.” Beckman Coulter, Inc. (2011).

[15] “NanoSight LM10 Nanoparticle Analysis System & NTA 1.5 Analytical Software: Operating Manual.” NanoSight Ltd., Salisbury, United Kingdom (2008).

[16] M. Kappes, S. Lee, Y.A. Hassan. “Size Characterization of Fibrous Nukon Debris Upstream and Downstream of the Containment Sump Strainer.” American Nuclear Society Transactions, Vol. 111, Pgs. 1586-1589 (2014).

[17] “Morphological Parameters for Particles – Illustrations.” National Institute of Standards and Technology, Maryland (2008).

<http://www.nist.gov/lispix/doc/particle-form/morph-param.htm>.

[18] “Glossary of Morphology Terms.” National Institute of Standards and Technology, Maryland (2009). <http://www.nist.gov/lispix/doc/particle-form/part-morph-gloss.htm>.